Multi-mode Controller Development for Cross-Flow Hydrokinetic Turbines

Dominic D. Forbush

A dissertation submitted in partial fulfillment of the
requirements for the degree of

Doctor of Philosophy

University of Washington

2018

Reading Committee:
Brian L. Polagye, Chair
Andrew Stewart
Brian C. Fabien

Program Authorized to Offer Degree:
Mechanical Engineering

University of Washington

Abstract

Multi-mode Controller Development for Cross-Flow Hydrokinetic Turbines

Dominic D. Forbush

Chair of the Supervisory Committee:
Brian L. Polagye
Department of Mechanical Engineering

Cross-flow turbines, in which the axis of rotation is perpendicular to the direction of inflow, have particular advantages over axial-flow turbines in aquatic settings, but are not as well understood. The applicability of axial-flow controls research to cross-flow systems is limited because cross-flow turbines have unique dynamics and fewer means of control actuation. This work explores the unique dynamics of cross-flow turbines, proposes a methodology for performance characterization in non-uniform inflow appropriate for field-scale devices, and investigates potential torque control strategies through computer simulation, laboratory experiment, and field-scale testing. The objective is to develop and evaluate control algorithms that are broadly applicable to cross-flow turbines. An emphasis is placed on simplicity: required sensing, the complexity of any necessary turbine characterization, and actuation requirements are minimized to ensure that proposed controllers are broadly implementable on extant turbines. The potential costs and benefits of added system complexity can then be considered against this benchmark on a device-specific basis.

Firstly, a method is suggested to define an effective inflow velocity for turbine performance characterization from a series of point velocity measurements in a spatially non-uniform but temporally consistent flow field. This characterization is necessary to appropriately anticipate device power outputs, to evaluate controller performance, and to allow accurate turbine simulation. When paired with time-average estimates of turbine power output, the developed performance characterization curve is found to be consistent for temporally-separated power measurements. Turbine performance is found to be highly sensitive to flow measurement location when subject to a hypothetical control law relying on an upstream point-measurement of velocity. This implies that multiple sensors or a spatially-resolved measurement of inflow would be necessary

for good turbine performance, which contravenes the control objective of minimal sensing requirements.

Secondly, three potential power-maximizing controllers were considered in simulation, experiment, and at field-scale. While the field-scale and laboratory turbines were not directly geometrically or hydrodynamically scaled, they were morphologically similar (i.e., both were four-bladed helical turbines) and had similar normalized time-average performance curves. The effect of neglecting phase variations in turbine performance in simulation is considered, but is found to be insignificant because the helically-bladed turbines have relatively consistent power output. In addition, the ability to apply torque in the direction of turbine rotation (i.e, "motoring" the turbine) is not presumed: only resistive control torques are allowed. Simulation was found to predict controller behavior in both a time-resolved and statistical sense, and trends in controller performance in the laboratory were also observed at field-scale. The largest sources of simulation error were related to unmodeled dynamics of the physical control implementations and simplifications to the flow interaction model. Accurately modeling dynamics of the physical implementation is found to be critical for simulation to be reflective of physical testing, particularly when the implementation is non-ideal (i.e., latency, sensor noise, etc.), and these non-ideal elements are likely to vary device-by-device. One evaluated controller required an upstream measurement of inflow and an advection model: this was not found to enhance performance of the laboratory turbine and significantly complicated implementation. Nonlinear "Kω^2" control, which requires only a time-average turbine model and a measurement of angular velocity, showed the best performance of the evaluated controllers.

Thirdly, the best-performing power-maximizing controller (a nonlinear controller) is incorporated with a nonlinear rated power-tracking controller and a strategy to transition between the objectives proposed. Power-tracking control is performed "overspeed" (i.e., the turbine accelerates to decrease power output) to provide superior stability properties to "underspeed" control. In keeping with controller objectives, each control law and the transition strategy requires only an angular velocity measurement and a time-average turbine characterization for implementation. The control law is examined in simulation and experiment for two cross-flow turbines: the helical turbine used in the previous study, and a turbine with two straight blades. Because the power output from the straight-bladed turbine is much more variable than for the helical turbine, these cases provide contrasting dynamics to evaluate controller effectiveness. Again, only resistive control torques were allowed, but because of the phase variation in power output, the simulation included phase-resolved turbine performance models. For both turbines, in all laboratory cases, constant power set points are closely tracked (less than 3% mean absolute percentage error). The limited observed error has two contributing factors, both with a common cause. The combination of filtering, sensor sampling rate, and torque feedback loops present in experiment effectively delay control response. During relatively large flow accelerations, this delay results in a steady-state tracking error. Particularly for the straight-

bladed turbine, the delay results in imperfect mitigation of the natural phase variation in power output. In simulation, steady-state error due to flow accelerations is negligible, but, as demonstrated via spectral analysis, unmitigated variations remain for the straight-bladed turbine. An analytical examination of phase-resolved turbine dynamics indicates that perfect mitigation is not generally possible under purely resistive torque, but scales favorably with turbine radius. Simulation suggests that this is not an issue for turbines with relatively constant power output, such as the helical turbine. These conclusions are extended to field-scale turbines and cross-flow wind applications.

The presented controller can be broadly implemented on field-scale devices due to its minimal sensing and actuation requirements. However, it has yet to be demonstrated on a field-scale device. Additionally, the relationship between power-smoothing accomplished at the turbine (as investigated here) and that which can be performed by power electronics will vary by device. Thus, the presented algorithm is not expected to be generally optimal, but a useful benchmark against which the performance of more demanding implementations can be compared. Other areas suggested for future work include the exploration of optimal control trajectories for various cost-functions and actuation capabilities (e.g., the ability to motor the turbine) using phase-resolved turbine models. While these models are not expected to accurately predict physical turbine performance, the general form of the suggested optimal controller could serve as a starting point for the development of alternative control laws, specifically model-predictive control.

The major contributions of this work are a method for performance characterization in non-uniform inflow, a demonstration of the extent to which simple simulation and laboratory-scale testing is predictive of field-scale response without explicit consideration of geometric or hydrodynamic scaling parameters, and a simple, general purpose turbine control law demonstrating good power-tracking performance and smooth, stable transitions between control objectives.

Acknowledgments

I am grateful for the continuing support of my parents, David and Joan, who funded my undergraduate education and then some. Thanks to them, I had a roof and food whenever I needed, and, at all times, strong examples of fortitude, drive, and compassion. I am also grateful for my sisters Maria and Sophia, and my dog Whiskey Jack, who helped me keep it all in context by regularly reminding me that most normal people (and puppies) don't care at all about math or fluid mechanics. And to Karla Diaz, who has put up with me through the drastic ups and downs of the last couple years and kept me on track when I was seconds away from dropping everything and becoming a potato farmer (or a writer, or a baker, or whatever it was that week). Thanks also to my grandparents, aunts, uncles and cousins for making our family so solid. And to my best friend Sarah, for staying by me no matter what; I'll see you on the other side.

I was inspired to pursue my Ph.D by Larry Clifton, whose passion for and mastery of all things mathematical still resonates with me today, and whose dedication to the most fundamental aspects of his discipline broadened, deepened, and strengthened this engineer's understanding: "If something is an 'abstraction', that's a sign that you ought to really be paying attention".

To Dr. Brian Polagye, my advisor and committee chair, I owe an immense debt of gratitude. His knowledge and expertise in the field, work ethic, and dedication to the development of his students has been both an inspiration and an asset. It is a humbling honor to have come up through his laboratory. He always goes above and beyond as a researcher and a mentor, and his selfless efforts have contributed to the growth of the field and the expansion of opportunities for his students. In addition, he is a warm, welcoming person, and we have on many occasions shared rad climbing days, good meals, and perhaps overly-intense game nights. Thanks also to the other members of my supervisory committee, Drs. Andy Stewart, Brian Fabien, and Michael Brett. Your advice, critiques, and support have been tremendously useful.

The Marine Renewable Energy Lab is a great place to learn and work. Current and former members or collaborators of the lab, Dr. Rob Cavagnaro, Curty Rusch, Hannah Ross, Emma Dewitt-Cotter, Ben Strom, Paul Murphy, Kate Van Ness, Dr. James Joslin, Trevor Harrison, Carl Stringer, Hannah Aaronson, Isabel Scherl and Dr. Ben Maurer, I thank you for the all the productive discussions and for being thoroughly enjoyable people to be around. It is an immense privilege to be surrounded by so much talent. The majority of the work presented herein is experimental, and it is difficult to overstate the impact of everyone who spent time and effort designing, disassembling, moving, and re-assembling (several times) our research flume and all the relevant accessories. I am particularly grateful for all help provided by those who had no intention of using the flume themselves, including the excellent work from Michelle Hickner, Bill Kuykendall, Eamon McQuaide, and Reggie Rocamora. I would also like to acknowledge the precision chilled water technical support staff at Parker for all their assistance: I am sure they very much regret providing me with any direct

contact information.

I also owe a debt of thanks to my skiing and climbing partners, especially Per Nesselquist, Carl Marrs, Rich Ellison, James Wyland, Jimmy Davis, Carl Stringer, Drew Bateman, Chase Hathaway, Emily Hanson, Shelley Leiphart and Brendan Moran. There is nothing like gravity-induced fear to make the stresses of academia disappear, and there is no one better to experience this with than good friends.

Work in Igiugig, Alaska and other work related to the RivGen turbine is based upon work supported by the Department of Energy under DE-EE0006397. Support from Nortek USA, the Alaskan field crew (Joe Talbert, Alex deKlerk, Curtis Rusch, Ryan Tyler, and Monty Worthington), ILC camp, Dena'ina Air Taxi, and the village of Igiugig is gratefully acknowledged. The assistance and collaboration of the Ocean Renewable Power Company, particularly Jarlath McEntee and James Donegan, is especially recognized. Laboratory-scale testing and simulation efforts are based on work funded by the Naval Facilities Engineering Command. The support of Dr. Eric Clelland during experimental campaigns at the Bamfield Marine Science Center is appreciated. Finally, the Alice C. Tyler trust funded numerous improvements to the flume. Their support, and the hard work of the members of the Marine Renewable Energy Lab, combined to make the aptly-named Tyler flume one of the finest facilities for hydrokinetic turbine research.

Disclaimer

Work funded in whole or part by the Department of Energy carries the following disclaimer: This was prepared as an account of work sponsored by an agency of the United States Government. Neither the United States Government nor any agency thereof, nor any of their employees, makes any warranty, express or implied, or assumes any legal liability or responsibility for the accuracy, completeness, or usefulness of any information, apparatus, product, or process disclosed, or represents that its use would not infringe privately owned rights. Reference herein to any specific commercial product, process, or service by trade name, trademark, manufacturer, or otherwise does not necessarily constitute or imply its endorsement, recommendation, or favoring by the United States Government or any agency thereof. The views and opinions of authors expressed herein do not necessarily state or reflect those of the United States Government or any agency thereof.

Contents

List of Figures

List of Tables

1 Introduction

Moving water can contain large amount of harvestable energy. Fast-moving flows of water are found in rivers, tidal channels, and the western boundary currents of oceans [1] [2] [3]. A current turbine is a device designed to convert a portion of the kinetic energy in the moving flow to mechanical energy. Typically, this energy is ultimately converted to electricity via a generator. Current turbines operate without impounding water, making them a viable option in areas where a dam or barrage would be infeasible [4]. Current turbines can be broadly subdivided into axial-flow, where the axis of rotation aligns with the inflow direction, and cross-flow, where the axis of rotation is perpendicular to the inflow direction. The present work focuses on cross-flow turbines, which, in the wind sector are often referred to as vertical-axis turbines. The utility-scale wind energy market is dominated by axial-flow turbines, but cross-flow turbines have a number of beneficial attributes in currents, offshore wind, and small-scale wind applications [5] [6]. For example, in a vertical orientation, cross-flow turbines do not require a yaw mechanism to maximize power output. In bi-directional flows, common for tidal currents [2], horizontally-oriented cross-flow turbines can operate efficiently and maintain a lower profile in the water column, which are advantageous for shallower channels. Further, cross-flow turbines tend to operate at lower blade speeds, limiting the risk of cavitation, decreasing noise production, and reducing the risk of collision with marine animals [4] [7]. Finally, dense arrays of turbines occupying a large portion of a confined channel can improve individual turbine power conversion efficiency and significantly enhance array performance [8]. Because cross-flow turbines can have a rectangular cross-section, they are more amenable to high-density arrangements in rectangular channels than axial-flow turbines. Note that because air does not have a "free-surface" vertically bounding the flow in the same respect as a cross-flow turbine, and cavitation is not a concern, several of the advantages of cross-flow turbines are unique to submerged applications. However, cross-flow turbines are actively studied for wind applications as well, emphasizing offshore deployments [6] [9], stand-alone small-scale devices, and dense counter-rotating arrays [10]. Cross-flow turbine technology remains at an earlier stage than axial-flow systems due in part to the convergence of the wind industry on the three-bladed axial-flow design [5].

Cross-flow turbines have disadvantages. Firstly, particularly in submerged applications, flow can be strongly sheared [2] [1]. Cross-flow turbines potentially have longer aspect ratios than axial-flow turbines, implying that the former may be more strongly affected by sheared inflow. Cross-flow turbines also cannot typically adjust the mounting angle of their blade (i.e., pitch control), an actuation mode commonly utilized on axial flow systems [11], and must rely on a single degree of freedom, the torque applied at the power-take-off, to affect control. There are exceptions to this generalization: numerous computational studies ([12],[13],[14],[15],[16]) have explored the potential advantages of active pitch control. There are also limited

examples of laboratory-scale pitch-actuated cross flow turbines [17]. While field-scale designs have been proposed [13], as of this writing, the author is unaware of any field-scale cross-flow devices capable of pitch actuation. This leaves a sole degree of freedom available for control of cross-flow turbines: the torque applied to the turbine rotor, to regulate turbine speed such that all controls objectives are met. Thirdly, the motion of a cross-flow rotor relative to the inflow yields unsteady fluid dynamic effects [16] that can dominate turbine loading and rotor dynamics [5]. The amplitude of these cyclic oscillations related to blade passage can be more than an order of magnitude larger than those observed in an axial flow turbine of similar size. This presents unique design, modeling and control considerations [6], [18], [19], [20]. With the emergence of the offshore wind and water current energy markets, it is critical that cross-flow research addresses these specific limitations so that the technology can be best applied.

This dissertation presents a methodology by which a cross-flow turbine controller can be developed for both power-maximizing and power-tracking objectives. A prerequisite to controller development and evaluation is the characterization of turbine performance. Sheared inflow complicates this characterization, which is generally parameterized based on a singular (i.e., not spatially varying) estimate of inflow velocity. Section 3 proposes a methodology for field-scale turbine characterization in spatially varying inflow for which time-varying fluctuations can be neglected over the duration of the characterization effort. Using this characterization, Section 4 explores power-maximizing control in simulation, laboratory experiment, and subsequently, field implementation. A difficulty endemic to many fluid-dynamic investigations, including turbines, is the question of scale: how conclusions drawn for small, laboratory scale devices will (and will not) hold for larger-scale devices of interest to industry given the mathematical impossibility of scaling all relevant parameters simultaneously, and the physical impracticalities of scaling even singular hydrodynamic parameters [18]. Due to the parallel investigations at laboratory and field-scale, Section 4 considers these questions of scale directly in the context of controller performance. Section 5 proposes a control algorithm for power maximizing and rated power tracking operating conditions and a means to automatically transition between them. The presented controller is intentionally simplistic: requiring a minimal set of sensors and functioning under restrictive assumptions regarding hardware implementation such that it might be applied readily to a wide range of field-scale devices. The limitations of the control algorithm are explored analytically, and implications for field-scale and array-based applications are considered. The main body of work contained in Sections 3, 4, and 5 has been published (or is currently in-review) in peer-reviewed literature. A citation is provided, and any differences from the published version are noted in the chapter headers. The subsequent section (Section 2) presents a summary of relevant subjects and literature to motivate the investigation.

2 Background

2.1 Turbine Dynamics

The dynamics of a cross flow turbine generally obey the first order non-linear differential equation

$$J\dot{\omega} = \tau_h - \tau_c \tag{1}$$

where J is the turbine moment of inertia (kg-m^2), τ_c is a control torque (N-m), ω angular velocity (rad/s) and the dot implies a time derivative [21]. Hydrodynamic torque is defined as

$$\tau_h = \frac{1}{2}\rho A R C_Q(\lambda) N_Q(\lambda, \theta) U^2 \tag{2}$$

where ρ is fluid density (kg/m^3), A is turbine projected area (m^2), R is turbine radius (m), U is the inflow velocity affecting the turbine (m/s), C_Q is the time-averaged torque coefficient, depending only on tip speed ratio

$$\lambda = \frac{R\omega}{U} \tag{3}$$

and

$$\{N_Q(\lambda, \theta) \in \mathbb{R} : \tau_h(\lambda, \theta, U)\} \tag{4}$$

is a non-dimensional correction for variations in C_Q due to changes in turbine azimuthal position (θ). This formalism also facilitates comparison between time-average and phase-resolved simulations (e.g., for a time-averaged model, $N_Q = 1$, when averaging occurs over a large number of turbine rotations). In axial-flow wind turbines, variations in turbine dynamics with azimuthal position are due primarily to wind shear and tower shadow, effects that occur for each blade once per rotation [21] [22] [23] [24]. The net impact of these intra-cycle torque variations is on the order of 10% of the mean (i.e., values $0.9 < N_Q < 1.1$ are expected) for 'upwind' axial-flow turbines (but can significantly larger for 'downwind' devices [25]). In contrast, the main source of intracycle variation in a cross-flow turbine is the changing blade orientation to the relative inflow [19], and the variations in N_Q are expected to be an order of magnitude larger .

Reference fluid power is

$$P_{fluid} = \frac{1}{2}\rho A U^3 \tag{5}$$

and depends on time-varying fluctuations in U. U can also vary spatially across the turbine rotor area, making reference fluid power difficult to sense and describe in non-uniform time-varying flows. Turbine shaft power is the product of control torque and angular velocity. This implies the mechanical efficiency of the turbine is phase-varying. The non-dimensional power coefficient is

$$C_P = \frac{\tau_h \omega}{P_{fluid}}. \tag{6}$$

C_P is commonly presented in a time-average sense as a function of λ [21], which yields a non-dimensional performance curve with a single maximum C_P^*, occurring at λ^*. Changes in turbine rotation rate and performance are therefore expected even in constant inflow, due to intracycle variations. In Region 3 control, where a fixed-pitch cross-flow turbine is purposely operated away from λ^* to maintain constant power, the turbine can be operated underspeed, where time-average $\lambda < \lambda^*$, or overspeed, where time-average $\lambda > \lambda^*$.

Similarly, the electrical 'water-to-wire' efficiency of the system is defined

$$\eta = \frac{IV}{P_{fluid}} \tag{7}$$

where I and V are the electrical current (A) and voltage (V) developed by the turbine. This includes any losses in the generator and power electronics: the efficiency of these combined components is in fact η/C_P. The extent to intracycle variations will be present in η depends on the specific turbine implementation [26], however it is generally characteristically similar to C_P in a time-average sense, which can be presented in a similar way as a function of λ.

The mechanical power available to the power take-off is

$$P = \tau_c \omega \tag{8}$$

and, for purely resistive control, torque is constrained such that

$$\tau_c > 0. \tag{9}$$

Restricting actuation in this way implies that the turbine will never draw power from the grid or power-electronics, potentially simplifying implementation and reducing cost.

Loads experienced by the turbine also drive design and control decisions. The stream-wise thrust force exerted on the turbine F_x can be similarly described as

$$F_x = \frac{1}{2}\rho A C_T(\lambda) N_T(\lambda, \theta) U^2 \tag{10}$$

where C_T and N_T are the time-average and phase-resolved coefficients, analogous to C_Q and N_Q, respectively (Eq. 2).

2.2 Turbine Control Overview

2.2.1 Control Objectives

Hydrokinetic and wind turbines of both axial and cross-flow varieties are expected to encounter varying flow speeds. Generally, a controller will attempt to maintain an operating condition in spite of varying inflow. The specific control objective will depend on the flow speed and the device [27]. If the flow speed is too low, it is not economical (and may not be possible) to operate the turbine. This is referred to as Region 1, (Figure 2.1). When the flow has reached the 'cut-in' speed of the device, a controller should maximize captured power until the device rated speed is reached (Region 2). At rated speed, the device is capable of generating rated power. The turbine controller should attempt to maintain rated power at and above rated speed, as this will maximize captured power without damaging the system (Region 3). In extremely high flow speeds above the 'cut-out' speed of the turbine, a controller should shut-down the system to prevent damage (Region 4). In contrast to wind, flow speeds resulting from tidal forcing are highly predictable over long time horizons, and thus, Region 4 control is likely unnecessary for a tidal turbine sized sufficiently for the predicted inflow. However, extreme events in river-deployed turbines such as flooding may necessitate Region 4 control protocols.

Axial-flow wind turbines generally switch from torque control in Region 2 to blade pitch control in Region 3 [21]. In many cases, the transition requires an additional "Region 2.5" control law to ensure that neither turbine rated speed or rated torque are exceeded during the transition and to reduce large transient responses.

In addition to maximizing or tracking power, turbine control laws also generally attempt to limit the loads experienced by a turbine. These can include thrust loads, blade loads, or drive-train loads. In addition to minimizing peak loads, the amplitude and frequency of cyclic loading are considered for fatigue calculations and to avoid excitation of system structural resonances [28]. The critical loads depend on the design of the turbine system and the purpose of its deployment, and the relative importance of load mitigation to achievement of power objectives can be distinct on a device-to-device basis. Meeting multiple control objectives involves the minimizing a cost function quantifying the relevant performance data over time [29].

In order to advise cross-flow controller development while remaining agnostic to a specific device, the

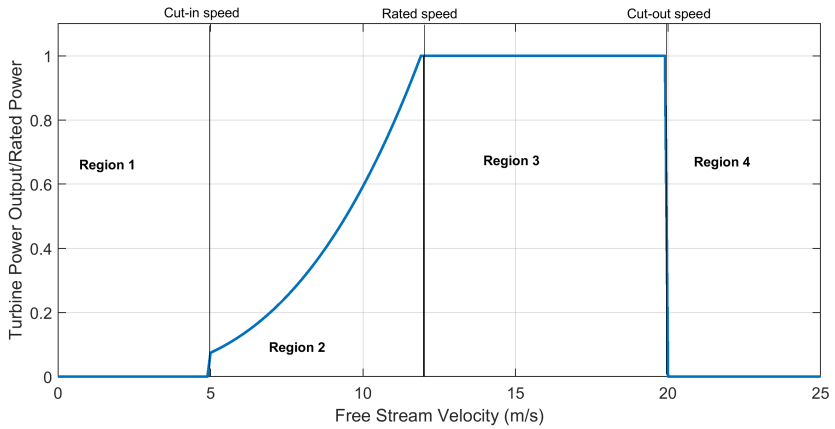

Figure 2.1: Normalized power capture for each control regions as a function of flow speed for an arbitrary turbine

present work focuses on the attainment of power-related control objectives and considers implications of these control decisions on turbine loadings without presuming a specific cost function. Because multi-objective control can imply the availability of numerous and specific sensors, this approach will broaden the implementations to which the investigated controllers are applicable. To that end, a control law needing only a time average turbine model is preferred to one necessitating a phase-resolved model, as the derivation of an accurate phase-resolved model requires additional sensing and a far more involved characterization effort. This is explored in more detail in Appendix A. Finally, the ability to "motor" the turbine by extracting power from the grid or some other energy storage source is not presumed (except to initially start the turbine, if it cannot generate sufficient hydrodynamic torque while stationary). This further broadens potential applications by reducing the requirements on implementation hardware.

2.3 Characteristics of Turbulence

Region 2 and Region 3 control objectives depend on maintaining a specific λ (Eq. 3) or a specific P, respectively. In the case of the latter, the turbine produces P and is in equilibrium only for a specific τ_h, which itself is a function of λ. This implies that a change in inflow will disturb this operating condition and require a controller to compensate for the disturbance. A change in local velocity from the mean flow velocity is referred to as turbulence and varies in both space and time within a flow field. Turbulence, by nature, is stochastic and the time-domain behavior cannot be predicted. However, frequency-domain behavior can be estimated with knowledge of fluid properties and the characteristics of the inflow environment [30], [2], [31]. The frequency-domain representation of turbulence can be related to a spatial scale via Taylor's hypothesis [32], in which the measured turbulence at frequency f (Hz) is assumed to advect with the mean flow velocity $\overline{U}$ (m/s) such that its spatial scale l (m) can be assumed via

$$f = \overline{U}/l. \tag{11}$$

An example frequency-domain representation of turbulence is shown in Figure 2.2. The existence and nature of turbulence present in flow can be characterized by the Reynolds number

$$Re = \overline{U}c/\nu \tag{12}$$

where c is a length scale, and ν is the kinematic viscosity of the fluid. Reynolds number is a ratio of the inertial forces to dissipative viscous forces in the flow. Flows with large ($> 5x10^4$) Reynolds numbers are turbulent. Because high-energy flows attractive for energy conversion have high inflow velocities (Eq. 5), all high-energy flows in a natural environment are turbulent. At high Reynolds numbers, Kolmogorov's hypothesis of local isotropy states that small-scale fluid motions are statistically isotropic, implying that the turbulent flow field (i.e., the flow field with the mean flow removed) is statistically invariant under rotations and reflections [33]. Viewed in the frequency domain, the power-spectral density of isotropic inertial turbulence obeys an $f^{-5/3}$ decay law, indicated in Figure 2.2. Lower-frequency (i.e., large spatial scale, via Taylor's hypothesis, Eq. 11) turbulence is generally assumed to be anisotropic. Generally, the most energetic turbulence in a natural flow, and those on a spatial scale commensurate to the size of a turbine, will be anisotropic turbulence. This is a significant consideration for flow measurement in the context of turbine characterization or if the measured flow is to be used in a control decision, particularly for cross-flow turbines. If the turbulence is not isotropic, statistics of a stationary point-measurement of inflow in the mean flow direction cannot be extrapolated to other directions. Because cross-flow turbines have a particularly long aspect ratio that is perpendicular to the inflow direction, this suggests a wide sampling area would be necessary to describe the turbulence interacting with a turbine rotor and anticipate the disturbance to turbine operating conditions.

2.4 Control Approaches

Due to the breadth and depth of relevant research and development techniques, linear control laws are a reasonable first consideration for cross-flow turbine control. Linear proportional-integral (PI) control laws have been successfully employed for axial flow turbines in Region 3 [11]. As detailed in Appendix A, linearizing turbine equations predicts the onset of non-minimum phase behavior for torque controllers in a time-average sense as the peak of the $C_Q(\lambda)$ curve, which is an excellent estimate of low-speed stability limits for implemented torque controllers [34] [35], and provides a good estimate of frequency-response function of the turbine rotor [18]. Beyond this, however, linearized turbine models and resulting linear control laws

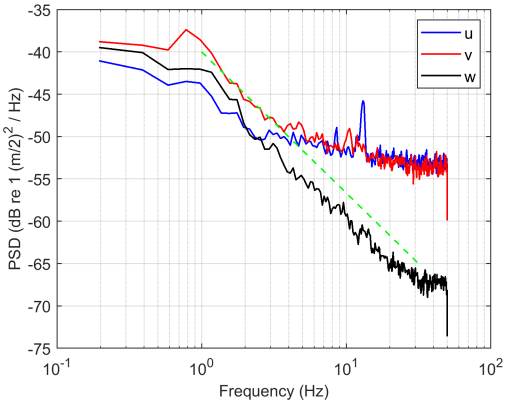

Figure 2.2: An example of turbulence spectra for the laboratory flume as measured by an acoustic doppler velocimeter. The hashed line indicates the $f^{-5/3}$ decay rate predicted for isotropic turbulence. The flattening of the horizontal components around 10 Hz is due to the noise floor of the instrument.

are fundamentally limited in performance for cross-flow turbines, which exhibit highly non-linear behavior. These limitations are discussed more thoroughly in Appendix A.

2.4.1 Non-linear Model-based Control

A commonly utilized power-maximizing algorithm for axial-flow wind turbines uses a time-average non-linear model of the turbine to hold rated power.

$$\tau_c = K\omega^2 \tag{13}$$

where

$$K = \frac{1}{2}\rho A R^3 \frac{C_P^*}{\lambda^3 *}. \tag{14}$$

The gain K is generally a static constant determined from the time-average C_P vs. λ relationship. A turbine obeying this relationship will remain operate at the maximum C_P^* (at λ^*) without a measurement of the inflow. If there are significant intracycle variations, the λ at which C_P is maximized varies with turbine azimuthal position, so this control law cannot maximize power in a phase-resolved sense. This control law can be extended to address azimuthal variation by scheduling K based upon the C_P vs. λ relationship at fixed θ ranging from 0 to 2π. This would again introduce the need for a phase-resolved model and the associated difficulties (Appendix A).

Extremum-seeking control laws are commonly implemented around $K\omega^2$ architectures that allow for the turbine point of time-average maximum power to be determined without *a priori* knowledge of the turbine

model (e.g., λ^* or C_P^*) through systematic variation of the turbine operating point. This form of control presents unique difficulties as applied to cross-flow turbines in the phase-resolved sense. These are discussed briefly in Appendix A.

2.4.2 Preview Control

State-of-the-art control for axial-flow wind turbines utilize a measurement of upstream turbulence to actuate the turbine in order to maintain an optimal operating condition throughout the turbulent disturbance. This requires a measurement of upstream flow, typically acquired from nacelle or ground-mounted LIDAR in wind applications [36] [21] [37]. In hydrokinetic applications, flow measurements are generally made using acoustic instruments [2] [30] (though examples of preview control in tidal applications are not readily available). Simple implementations assume that the measured turbulence advects without evolution from the measurement location until it interacts with the turbine rotor, as per Taylor's Hypothesis. The measurement of turbulence must be far enough upstream to allow sufficient time to actuate the turbine in advance of the flow interaction (a function of the mean flow velocity), but near enough to the turbine that the measured turbulence is a good estimate of the turbulence that will affect the turbine rotor (i.e., that Taylor's Hypothesis is approximately correct). More advanced implementations weight the consideration of the preview information in the control decision according to the recent accuracy of the inflow prediction [38].

As an example, the maximum power point control (Eq. 13) can be expanded to incorporate preview information as

$$\tau_c = K\omega^2 + K_U \hat{U_\infty}/J \tag{15}$$

where K_U is the linearization of the turbine response based on desired operating condition (Eq. 48) to a perturbation of the inflow velocity $\hat{U}_\infty$. The estimation of $\hat{U}_\infty$ is based upon an earlier upstream flow measurement that, according to an estimate of advection time, is presently affecting the rotor.

Preview control is closely related to model-predictive control, in which a model of a disturbance is used to predict turbine response, and controller behavior selected based on this prediction maintain the desired operating condition (e.g., [39]). A key difference in model-predictive control is that a real-time measurement of the inflow may not be explicitly necessary, and an estimate can be developed from previously measured states [28].

The implementation of this type of control for cross-flow turbines raises two unique considerations. Firstly, the need to actuate a turbine in advance of a turbulent gust implies (in the context of torque control) that the turbine would not accelerate to the desired operating condition with sufficient speed due to interacting

with the gust itself, which implies the turbine response bandwidth is limited by its inertia [18]. As noted above, cross-flow turbines have potentially lower inertia for a given swept area. Further, they have long aspect ratios, and only turbulent gusts of a spatial scale commensurate with the length of the turbine would significantly disturb the device. By Taylor's hypothesis (Eq. 11), this implies turbulence of a relatively low frequency. As noted in [18], decreasing turbine inertia tends to increase response bandwidth, which decreases device response time. The expanded bandwidth and the low frequency of energetic turbulence that would substantially disturb the turbine suggests that cross-flow turbine performance may not be significantly enhanced with preview inflow information, especially considering the uncertainty associated with such a measurement, and the cost and complexity of the additional sensing requirements. Secondly, an accurate advection model of upstream-measured turbulence is more critical for a cross-flow turbine, since effect of the turbulence on turbine dynamics (i.e., the value of K_U, in the linearized sense) and the appropriate control action will be a strong function of the turbine blade position (i.e., turbine azimuthal angle) when the turbulence interacts with the rotor. As mentioned in the discussion of turbulence, the long aspect ratio of a cross turbine may require multiple instruments to resolve the incoming flow field, and in an aquatic environment, the sampling methods have not been integrated with control decisions to the same extent as LIDAR-based sampling techniques for wind turbines; a significant hurdle that would limit the utility of preview control.

2.5 Scaling Controller Performance

It is well-established that turbine performance varies with geometric and hydrodynamic parameters that are mathematically impossible to correctly scale simultaneously. This is of concern because turbine controller performance may also be expected to vary with device scale, but it is desirable to pursue development of control algorithms at low-cost on laboratory scale devices. The performance of a candidate controller will depend only on how well-suited the controller is to the observed turbine dynamics, not the underlying hydrodynamic mechanisms driving those dynamics. Thus, if two turbines have similar time-average and phase-resolved performance curves *in the inflows in which control is to be applied* the dynamics of the turbine response to control will be similar if the respective turbine frequency response functions are appropriate for the anticipated excitation frequencies [18]. The emphasized caveat is reflective of the fact that, particularly in low velocity flows (i.e., low Reynolds number, as one might encounter in a laboratory test), turbine dynamics, specifically the C_Q vs. λ curve and the N_Q surface, can be expected to vary with inflow velocity (as a specific example, see Figure 5.2).

For controller performance to also be similar, the controller implementation must be tailored to site-

specific inflow disturbances such that response is similar. For instance, if turbulence affecting a laboratory-scale device occurs at frequencies an order of magnitude higher than turbulence expected to affect a field-scale device, then the controller update rate and sensor acquisition rate must also be increased by an order of magnitude to be predictive of field-scale controller performance.

Section 4 directly explores controller performance scaling between a laboratory and field-scale turbines of similar morphologies that are neither geometrically or hydrodynamically scaled, but have similar time-average performance curves.

3 Time-average Performance Characterization

The majority of this work has been previously published in the *International Journal of Marine Renewable Energy* under the title "Performance characterization of a cross-flow hydrokinetic turbine in sheared inflow" [40]. The version presented here has been shortened to reduce redundant presentation of background information and definitions and has been reformatted for consistency.

3.1 Introduction

A challenge in riverine environments is that variations in bathymetry may give rise to horizontal or vertical shear on the same length scales as a turbine rotor [41]. Because of this, there may not be an obvious choice of U_∞ for the non-dimensional representation of performance (e.g., C_P or η vs. λ).

This paper describes field measurements around a hydrokinetic turbine, the Ocean Renewable Power Company (ORPC) RivGen ® turbine, on the Kvichak River near Iguigig, Alaska (USA). The turbine and the deployment site are first described, followed by a description of measurements of stream velocity. The characterization of turbine performance in the presence of strong lateral (across-rotor) shear is then presented, and the paper closes with a discussion of the implications of these results for resource characterization, turbine control, and performance assessment.

3.2 Background

3.2.1 Turbine

The RivGen turbine is a cross-flow helical hydrokinetic turbine designed to provide community-scale power (10^4 W) as an alternative to diesel generation in remote communities [42]. The turbine consists of two 4.1 m long rotors situated symmetrically about a 2.8 m wide gap housing the generator (Figure 3.1).

Prior to installation, preliminary characterization was performed with tow trials in Eastport, ME. The turbine was lowered below a barge being towed at a constant velocity which resulted in near-uniform flow across the turbine. Using this method, the maximum water-to-wire efficiency was found to be $\sim 19\%$. This performance was in agreement with computational fluid dynamic simulation and is in-line with experimental performance of turbines with similar geometry [43] [44].

3.2.2 Site Description

The turbine was deployed in August 2014 on the Kvichak River just downstream of the village of Igiugig, Alaska (USA). A local coordinate system is defined in Figure 3.2, with $+x$ downstream (U component of

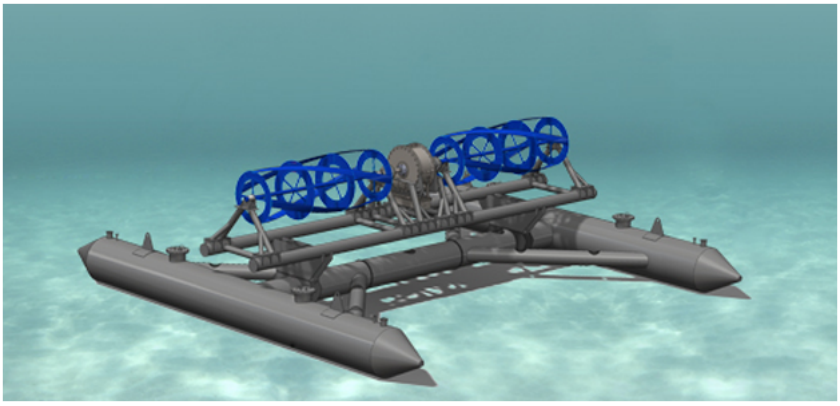

Figure 3.1: Conceptual rendering of the RivGen turbine

Figure 3.2: Turbine deployment location and local coordinate system at Igiugig, AK. Satellite image from Google Earth.

velocity), $+y$ cross-river towards the village (V component of velocity), and $+z$ upwards (W component of velocity). The origin is at the nominal center of the turbine (59.3248^o N, 155.9151^o W) and the rotation from an east-north-up (true) coordinate system is 107^o clockwise.

3.3 Stream Velocity Characterization

3.3.1 Methodology

Measurement

Inflow velocities were measured at points upstream of the turbine from Aug 15 to 25, 2014. Measurements were made with six Nortek Aquadopp profilers (1 and 2 MHz operating frequencies) deployed in a down-looking orientation from surface catamaran platforms (Doppcats, see Figure 3.3). Aquadopps sampled continuously at 1 Hz, with 0.5 m bins (bin #4 is approximately the hub-height of the turbine). The

Figure 3.3: Doppcat platform for down looking Nortek Aquadopp velocity profiler (left) and sounding weight platform for Nortek Vector velocimeter (right) at Igiugig, AK.

platforms were towed on tethers at 10 m spacing astern of a small skiff, which held station for 10 minutes at a variety of locations upstream of the turbine. The station-holding approach was adopted when anchors for the Doppcats were unable to hold sufficiently on the cobbled bottom. Platform locations were recorded at 5 Hz using Qstarz BT-Q1000eX GPS receivers, and this information was used to correct velocity measurements for platform motion in post-processing.

In addition, a Nortek Vector velocimeter was deployed on a sounding weight ("turbulence torpedo") lowered from a davit at the stern of the skiff to provide turbulence measurements at higher temporal resolution (16 Hz). These velocity data are subject to contamination by platform motion which are removed using data from a synchronous Inertial Motion Unit (IMU) on-board the instrument (Microstrain 3DM-GX3-25), following [45] and [46]. These velocimeter measurements were made twice, each for 10 minutes, approximately 60 m upstream and starboard ($+y$) of the center line of the turbine at the turbine hub-height ($z = -2$ m from surface). Turbulence measurements could not be made at closer proximity without risking damage to the turbine in the event of loss of skiff propulsion.

Uncertainty Analysis

The velocity measurements, which vary in space and time, are subject to measurement uncertainties that are dominated by the Doppler noise (ΔU_n) of the instruments. The stream-wise flow U, for example, is decomposed as

$$U(x,y,z,t) = \overline{U}(x,y,z) + U'(x,y,z,t) \pm \Delta U_n \pm \Delta U_{sk} \tag{16}$$

where $\overline{U}$ is the mean flow calculated from 10 minutes of data, $U'(x,y,z,t)$ is an instantanteous turbulent fluctuation, and ΔU_n is estimated as a constant noise level of 0.04 m/s for the 2 MHz Aquadopps and 0.10 m/s for the 1 MHz Aquadopps (based on the "Aquapro" configuration software provided by Nortek). There are additional uncertainties resulting from imperfect station keeping, measured via GPS as $\Delta U_{sk} \approx 0.1$ m/s.

The space and time variables also have uncertainties,

$$\tilde{x} = x \pm \Delta x_{\mathrm{GPS}} \pm \Delta x_{bs} \pm \Delta x_{sk} \tag{17}$$

which are the result of GPS errors ($\Delta x_{\mathrm{GPS}} \approx 5$ m), beam spreading of the down looking Aquadopps ($\Delta x_{bs} \approx 3$ m), imperfect station keeping ($\Delta x_{sk} \approx 5$ m), and Doppcat clock drift ($\Delta t \approx 1$ s). These uncertainties were assumed to be uncorrelated and averaging of results significantly reduced the uncertainty, such that robust estimates of the mean flow $\overline{U}(x, y, z, t)$ at a given position are repeatable. In the analysis that follows, spatial gradients of the mean flow are only reported up to a resolution equal to the uncertainty in x.

Turbulence Characteristics

Turbulence intensity is a simple scalar metric describing the ratio of velocity fluctuations, represented as the standard deviation, to mean velocity. Using Doppler profilers, robust estimates of the turbulence intensity TI are possible if the additional sources of variance from noise are removed [2].

$$TI(x, y, z) = \frac{\sqrt{\langle U'(x, y, z, t)^2 \rangle - \Delta U_n^2 - \Delta U_{sk}^2}}{\overline{U}(x, y, z)} \tag{18}$$

where $\langle U'(x, y, z, t)^2 \rangle$ indicates an ensemble value over 10 minutes of observations at a particular (x, y) station. The removal of noise is essential for determining the turbulence intensity from Doppler profilers, such as the Aquadopps ($\Delta U_n = 0.04$ m/s) on the Doppcat platforms. The results are verified against high-fidelity data from upstream deployments of the velocimeter ($\Delta U_n < 0.01$ m/s) on the turbulence torpedo. The velocimeter measurements also have the advantage of being well-localized in space, since they do not suffer the beam spread issue common to all profiler measurements [47].

Skewness is a measure of the asymmetry in the distribution in velocity fluctuations. Since it is a higher moment of the distribution, it can only be calculated using the low-noise velocimeter data. The skewness metric considered for each window is the adjusted Fisher-Pearson standardized moment

$$G_1 = \frac{n}{(n-1)(n-2)} \sum_{i=1}^{n} \left(\frac{x_i - \overline{x}}{s} \right)^3 \tag{19}$$

where n is the sample size, s the sample standard deviation, and $\overline{x}$ the mean of the sample [48].

Turbulent kinetic energy (TKE) spectra are a measure of the energy contained at particular time scales. This is calculated using the Fast Fourier Transform (FFT) of the velocity data in 10-minute windows, which are first divided into overlapping 256 s sub-windows, detrended, and tapered. After merging every five frequency bands, the resulting spectra have 30 degrees of freedom, resulting in relatively tight confidence intervals.

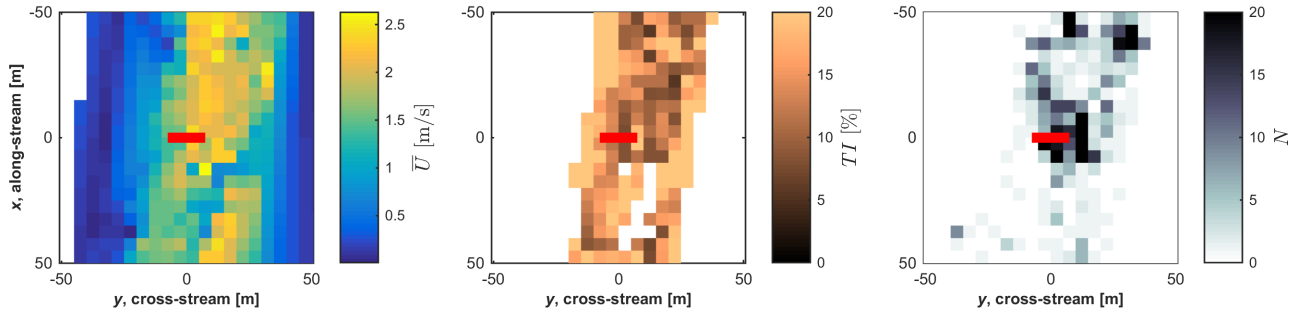

Figure 3.4: All mean stream-wise flow results (left), turbulence intensities (center), and number of 10-minute averages (right) from the Doppcat station keeping measurements at the turbine hub-height, $z = -2$ m below the surface. The turbine location is shown by a thick red line at the origin. Turbulence intensity values are not shown for grid cells with lacking a complete 5-minute data set ($N < 1$).

3.3.2 Results

Spatial Variability

The mean stream-wise flow $\overline{U}(x, y, z)$ shows a robust spatial pattern, with random turbulent fluctuations in time that are $TI \approx 10\%$ of the mean flow at most locations upstream of the turbine and in the center of the river. Figure 3.4 shows gridded observations collected with the Aquadopp profilers over 10 days. The temporal and spatial variations are separated by binning individual 10-minute ensembles into 5-m resolution grid cells (using the local coordinate system) and assessing sensitivity. The spatial variations in the mean flow are extreme, and in many cases the uncertainty in measurement position is a greater source of velocity changes than the $TI \approx 10\%$ turbulence intensity at any given point.

In the following subsections, the spatial patterns are addressed are cross-river y (i.e., lateral shear of inflow velocities) and depth profiles z (i.e., vertical shear of inflow velocities). For each axis investigated, the robustness of the spatial pattern is quantified with the standard error and standard deviation of the gridded mean velocity result and this is compared with velocity fluctuations expected from the average turbulence intensity TI in each grid cell.

Lateral Shear

The lateral shear of inflow velocities across the turbine rotor (i.e., from port to starboard, y-axis) is the most striking spatial pattern. As shown in Figure 3.5, the mean inflow velocity varies from 1.6 m/s at the port side of the turbine ($y = -5.5$ m) to 2.3 m/s at the starboard side of the turbine ($y = 5.5$ m). Results are the average from 338 stations lasting at least 10 minutes each, collected at positions immediately upstream of the turbine ($-20 < x < 0$ m). This 44% increase in speed is a 200% increase in the kinetic power density of the flow. This mean flow pattern is robust, as shown by the standard error lines in Figure 3.5. However

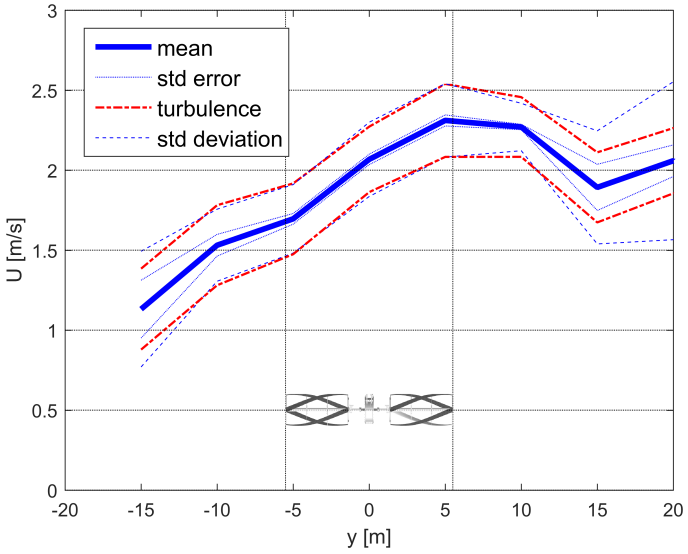

Figure 3.5: Lateral shear shown as the stream-wise flow U versus cross-river dimension y. The blue dotted line is the standard error in determining the mean flow at each y. The blue dashed line is the standard deviation of individual stations. The red dashed line is variation expected from the measured turbulence intensity. The turbine is also shown ($-5.5 < y < 5.5$) m.

the individual ensembles have significant scatter, as shown by the standard deviation lines in Figure 3.5. In fact, the standard deviations obtained from the uncertainties in spatial binning ($\Delta x_{\mathrm{GPS}} \approx 5$ m) are similar, and generally exceed, the velocity fluctuations attributed to turbulence within each ensemble.

The observed shear is expected given the proximity to a river bend and the ADCP surveys completed the previous year [49]. It also appears that a turbine deployed a few meters farther east, at approximately $0 < y < 11$ m, would have experienced a more uniform inflow. Although a few meters may seem an extreme sensitivity in a river that is 150 m wide, the deep region near the river bend is a much narrower feature and controls the overall flow.

Vertical Shear

There is minimal vertical shear in the stream-wise inflow velocities upstream of the turbine. As shown in Figure 3.6, vertical variations are typically less than 10% of the mean flow value at the turbine hub height $z = -2$ m below the surface. As for lateral shear, results are the average from 338 stations lasting at least 10 minutes each, collected at positions immediately upstream of the turbine ($-20 < x < 0$ m). Vertical shear is assessed at three locations in cross-river dimension y, nominally turbine port ($y = -5$ m), turbine center ($y = 0$ m) and turbine starboard ($y = +5$ m). The pattern from these three profiles is consistent with the lateral shear result, in which flow is strongest at the starboard side of the turbine and in which spatial uncertainties exceed turbulent fluctuations.

Turbulence

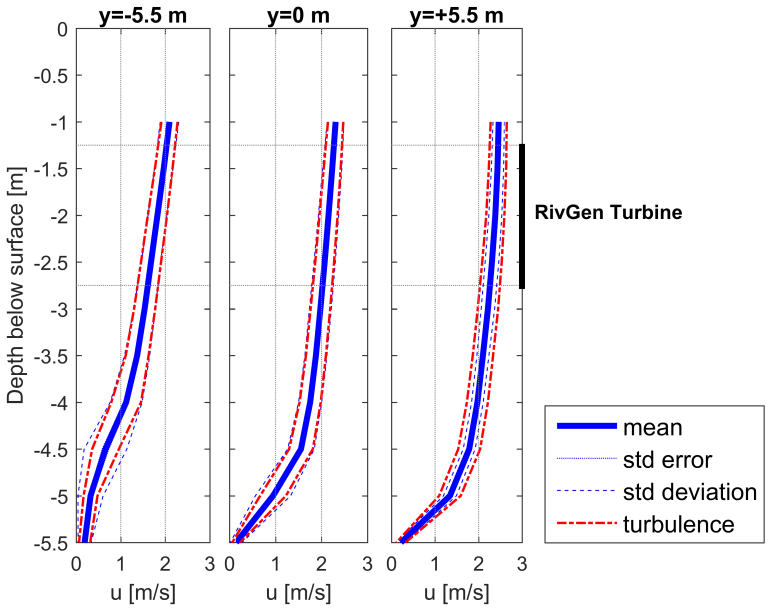

Figure 3.6: Vertical shear shown as the stream-wise flow U versus depth below the surface at three positions in the cross-river direction: nominally turbine port ($y = -5.5$ m), turbine center ($y = 0$ m) and turbine starboard ($y = +5.5$ m). The blue dotted line is the standard error in determining the mean flow at each y. The blue dashed line is the standard deviation of individual stations. The red dashed line is variation expected from the measured turbulence intensity. The vertical extent of the RivGen turbine rotor sweep is shown as a black line ($2.75 < z < 1.25$) m.

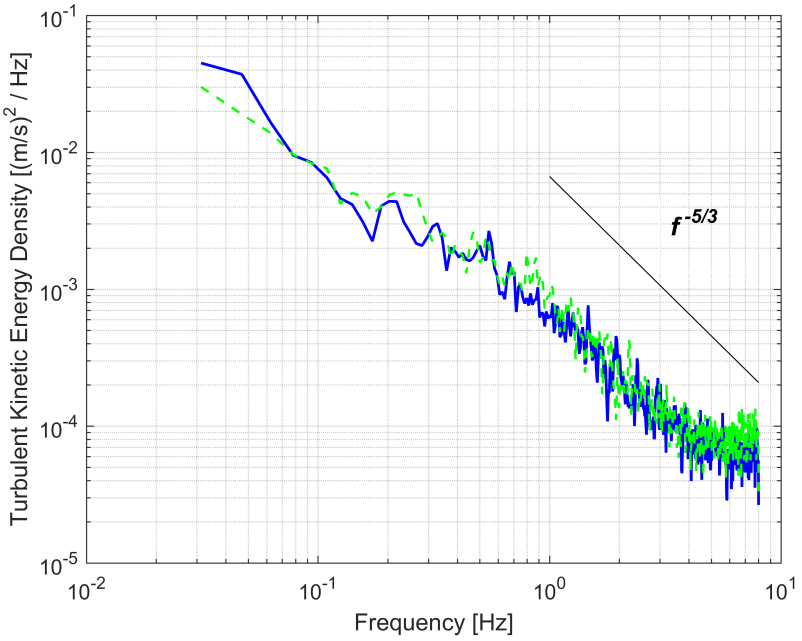

Figure 3.7: Turbulent kinetic energy spectra density versus frequency from two different sets of upstream velocimeter data (10-minute windows each).

Table 1: Turbulence characteristics

Location (m)	**Mean Velocity $\overline{U}$ (m/s)**	**Standard Dev. σ (m/s)**	**Skewness G_1**	**Turbulence Intensity (%)**
[-62.5,8.2]	2.46	0.264	-0.186	10.7
[-48.2,-46.3]	2.40	0.228	-0.171	9.5

The TKE spectra are most energetic at low frequencies, and show an expected $f^{-5/3}$ power law at high frequencies (Figure 3.7). This is consistent with the isotropic cascade of energy from large scales to small scales through the inertial subrange. The vast majority of energetic fluctuations occur at low frequencies, $f < 0.2$ Hz.

The velocity distribution upstream of the turbine shows left-skewness and similar standard deviations and turbulence intensities at both measured locations. Table 1 shows statistics determined for 10-minute windows from two upstream locations taken at turbine hub height. Their locations are given relative to turbine center, with $+x$ downstream and $+y$ towards the starboard edge of the rotor. Though mean flow velocity varies with position, the turbulence characteristics are relatively consistent in this region of the river.

Table 2: Performance data collection periods

Position	Date	Time (24 hr, ADT)
A	8/22/2014	1021-1057
B	8/25/2014	1211-1234
C	8/25/2014	1235-1254

3.4 Turbine Performance Characterization

3.4.1 Measurement Methodology

The turbine shore station included a resistive load bank with 15 discrete settings (nominally $2.3\,\Omega - 60\,\Omega$). During performance testing, a shore operator maintained a specific setting for a period of several minutes, during which time the voltage and current across the load bank were recorded at 1 Hz. From voltage, turbine angular velocity was determined via $\omega = V/k$ where k is a known empirical coefficient that is specific to the generator. All data sets were time-stamped based on an internet-synchronized time server.

On three occasions, the turbine was stepped through sequential resistive loads for performance characterization (Table 2).

Results from the three trials are presented in Figure 3.8 to demonstrate the magnitude of variability associated with different choices of inflow reference velocity (U_∞). In each case, a Doppcat positioned upstream of the turbine rotor provided an estimate for U_∞. To develop these curves, quality-controlled velocity measurements were synchronized with turbine performance and instantaneous η and λ calculated using equations 7 and 3, respectively. These instantaneous values were then averaged for each load setting. In retrospect, given the lateral shear present in the river (Section 3.3.2), the variability in the characteristic curves produced by point measurements is not unexpected.

3.4.2 Effects of Turbulence

Fourier analysis of the generator power time-series generated from this testing shows that the generator responds predominantly to the low-frequency perturbations ($f < 0.2$ Hz) of the flow (Figure 3.9). This time-series is a collection of 10-minute windows during which the resistive load setting was held at $5.4\,\Omega$. A power spectra was determined using the same spectral analysis techniques as in Figure 3.7 except that the velocity time-series (16 Hz) was down-sampled to 1 Hz for consistency with the generator power sampling rate and ensure equal spectral bandwidths. Due to the limited number of points, only adjacent frequency bands are merged to maintain resolution. Blade passage frequency is > 2.7 Hz and turbine rotation frequency is > 0.7 Hz so neither could be captured with this sampling rate. The resulting spectra are normalized by their variance and displayed on a common axis.

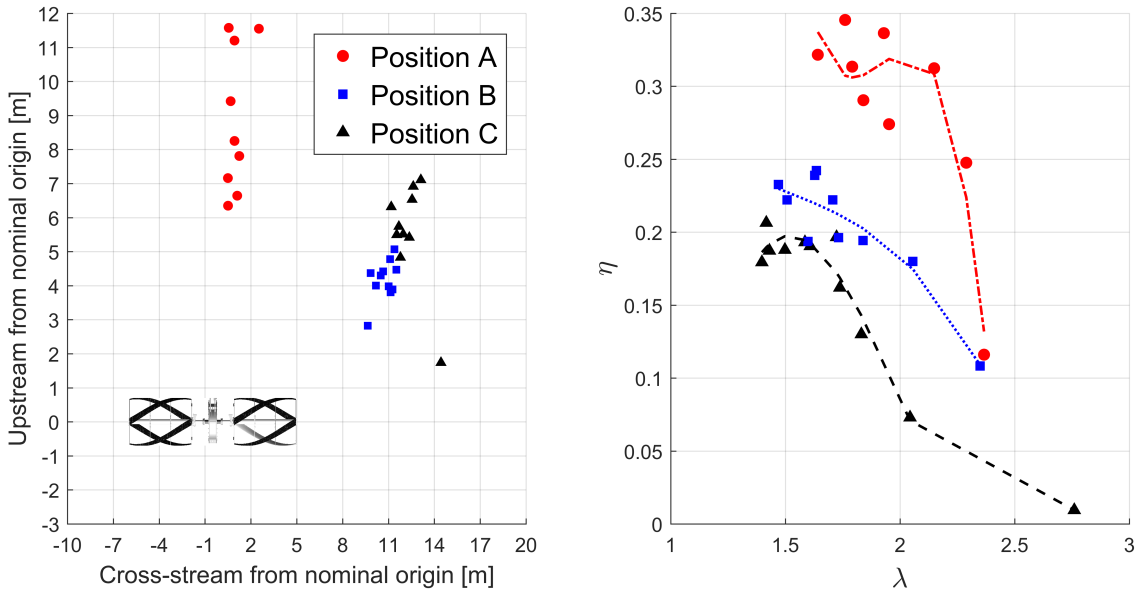

Figure 3.8: Performance curves calculated from time-synchronized point measurements of velocity (right) and the locations at which they were measured relative to the nominal center of the coordinate system with turbine also shown (left). The color coding is consistent between plots.

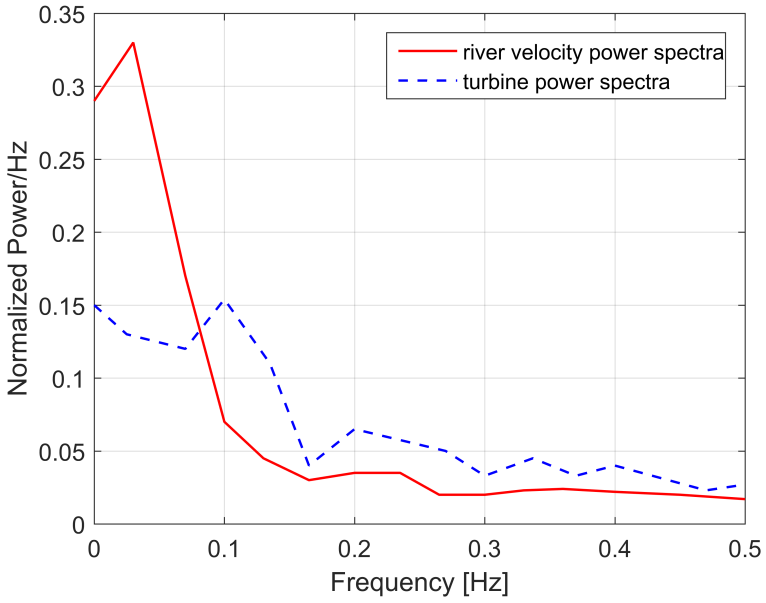

Figure 3.9: Normalized power spectra density of generator power and turbulent kinetic energy.

The turbine power output spectrum demonstrates that it responds most strongly to the energetic frequencies of the velocity spectra, which are $f < 0.2$ Hz. For a mean velocity of ~ 2 m/s, Taylor's hypothesis (Eq. 11) suggests that the turbine is sensitive to length scales l on the order of 10 m or greater. Because this is nearly the length of the rotor assembly, this implies that the turbine is primarily sensitive to "engulfing gusts".

3.4.3 Invariant Velocity Hypothesis

As discussed in Section 3.3, the turbine hub-height mean velocity profile is relatively robust in time. If an assumption of time invariance is made, then the performance time series can be decoupled from the flow velocity time series. If valid, the characteristic performance curve for each of the three performance series collected during the point measurement attempts should be consistent.

Generally, the reference velocity across the turbine rotor is a function of both time and space as

$$U_\infty = U_\infty(x, y, z, t). \tag{20}$$

Here, the infinity subscript denotes a reference inflow condition for turbine performance characterization, rather than the general velocity field described in Section 3.3. At a fixed position upstream of the turbine (constant x), the vertical shear is negligible (Section 3.3.2) and, if the lateral shear velocity profile is time-invariant (Section 3.3.2), a temporal average over a sufficiently long period approximates the lateral velocity profile across the turbine as

$$\langle U_\infty \rangle = \langle U_\infty(y, t) \rangle \tag{21}$$

where the angle brackets denote a temporal average. This corresponds to the mean velocity data presented in Figure 3.5. To select a $\langle U_\infty \rangle$ representative of the flow across the entire turbine, the spatial average is calculated as

$$\overline{\langle U_\infty \rangle} = \overline{\langle U_\infty(y) \rangle} \tag{22}$$

where the overbar denotes a spatial average in the lateral direction, excluding the region occupied by the generator and drive shaft. From the time-averaged flow profile in Figure 3.5, the span of points from end-to-end of the rotor were populated through linear interpolation at a resolution of 0.1 m and then averaged to obtain a single, representative value. The resulting profile is insensitive to this interpolation resolution provided it is fine enough to resolve the features of the flow (e.g. it is finer than the profile resolution).

From this temporally and spatially averaged free-stream velocity, an effective $\hat{\lambda}$ and $\hat{\eta}$ may be calculated as

$$\hat{\lambda} = \frac{\omega R}{\overline{\langle U_\infty \rangle}} \tag{23}$$

$$\hat{\eta} = \frac{\langle IV \rangle}{\frac{1}{2}\rho\alpha\overline{\langle U_\infty \rangle^3}A} \tag{24}$$

The correction factor (α) is introduced because the cube of the temporal mean is not equal to the mean of the temporal cube. However, the instantaneous velocity cubed is not observable by Doppcat measurements due to the Doppler noise associated with 1 Hz sampling. An empirical correction factor is generated from 16 Hz velocimeter data (low noise sampling) as

$$\alpha = \frac{\langle U_\infty^3 \rangle}{\langle U_\infty \rangle^3}. \tag{25}$$

This yields $\alpha = 1.03$, which does not significantly change the results, but is included for completeness.

Alternatively, the discrepancy between the cube-of-means and mean-of-cubes could be addressed in a similar manner to wind-resource assessment over longer time scales. Fitting a Weibull distribution to velocimetry data, a correction factor α accounting for the discrepancy can be derived using the properties of the distribution [50], which also yields $\alpha = 1.03$.

3.4.4 Invariant Velocity Results

Performance characteristics obtained from equations 23 and 24 during temporally-discontinuous measurements are presented as Figure 3.10. The consistency of the curves suggests that the time-invariant assumption is valid over this time period. A third-order polynomial fit over the range $1.5 < \hat{\lambda} < 3$ is also shown and taken as representative of turbine performance in subsequent analysis. The differences between the performance at each load setting is likely the result of slight differences in mean stream velocity between the three data collection periods. For example, the highest $\hat{\eta}$ points for each case range from 0.25 to 0.27. This difference could be caused by a 1% difference ($\sim$ 0.02 m/s) in flow velocity. The relative insignificance of these differences supports the time-invariant hypothesis for the mean lateral inflow.

If the resulting performance curve is assumed to be valid at any position along the turbine rotor (that is $\hat{\eta}(\hat{\lambda}) = \eta_i(\lambda_i)$), then an analytical model can be constructed to evaluate local performance and the contribution of each segment of the rotor to aggregate power output. This model assumes a span-wise constant ω with spatially varying U_∞, resulting in local variations in λ_i that translate to local variations in

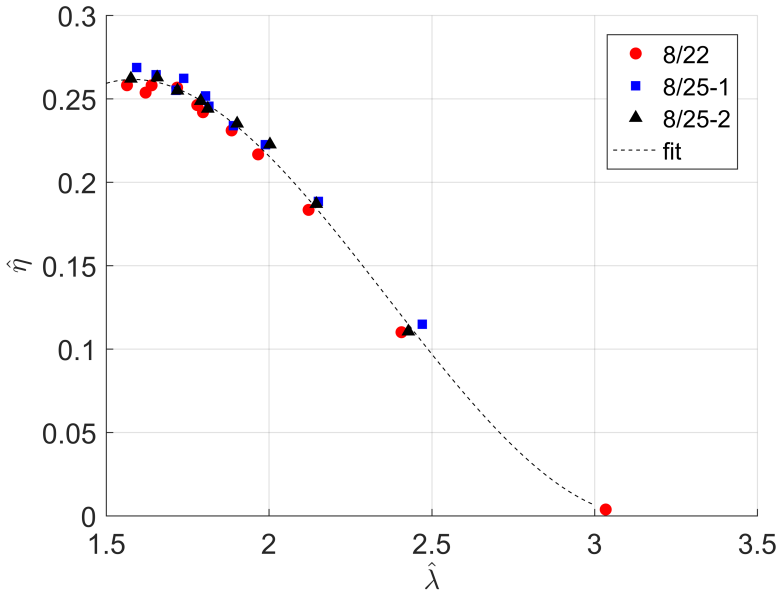

Figure 3.10: Turbine performance assuming a temporally-invariant inflow, shown with 3rd-order fit. The clustering of the points is a result of the discrete load settings used for characterization

η_i. For this model, the power curve is assumed symmetric about $\hat{\lambda} = 1.5$, so rotor sections operating locally $\lambda_i < 1.5$ generate power. However, if the average $\overline{\lambda_i} < 1.5$ across the rotor, the turbine is assumed to have stalled, generating no power (as was observed in the field). As for performance characterization, the turbine is approximated as a series of independent elements, $\Delta l = 0.1$ m. The power output is the summation of the relative contribution from each rotor element (i.e., $P = \Sigma P_i$).

Figure 3.11 shows the aggregate power output from the turbine if performance is optimized at $\lambda_i = 1.59$, at a specific span-wise location. The maximum power output is 12.5 kW, in agreement with field observations. This does not provide additional certainty in the results (it is simply a different expression of turbine performance using the previous method). Overall, these results suggest that the location along the rotor where λ should be defined to maximize power generation is the one that maintains λ_i close to the global maxima for rotor elements in the most energetic flow, while keeping the average $\overline{\lambda_i} > 1.5$. This optimal location is a function of shear profile, shape of the performance curve, and rotor geometry.

This is illustrated by the pronounced discontinuity in power output if λ_i is "optimized" over the left-most rotor elements. The majority of the rotor is operating below $\lambda_i = 1.5$, and is stalled (below the minimum operable $\hat{\lambda}$ in Figure 3.10). As the point defining $\lambda_i = 1.59$ moves farther right, the majority of the rotor begins to exceed $\lambda_i = 1.5$ and comes out of stall, producing power (in reality, the jump from a stalled rotor to near peak power would likely occur somewhat more gradually). Because the stall point is close to the $\hat{\lambda}$

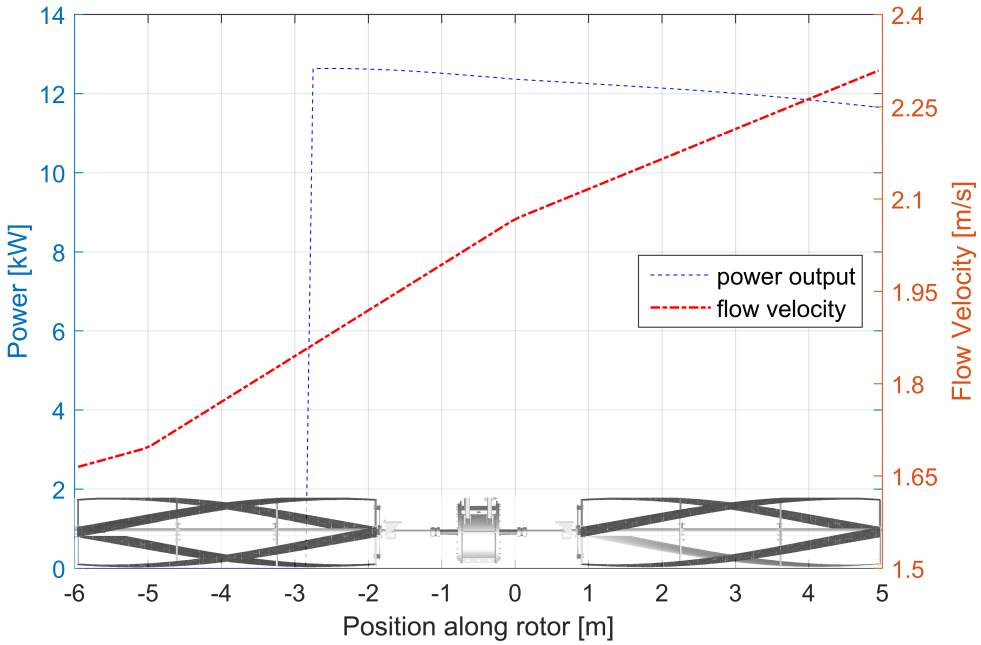

Figure 3.11: Aggregate power output in sheared flow as function of point along the rotor where local performance is optimized. Also shown is the 2-D velocity profile (assumed time-invariant) at turbine hub depth. Turbine schematic superimposed for reference.

for which $\hat{\eta}$ is maximized, (Figure 3.10), once the rotor is no longer stalled, the sections in higher velocity are also at a near optimal λ_i, maximizing power output for the entire rotor, as shown in Figure 3.12. As the defining point continues right, more of the rotor operates sub-optimally, slightly decreasing power output.

The power contribution of a rotor element to the total power when the maximum power-generating governing point is selected is shown in Figure 3.13. The highest contributing sections, as expected, fall within the high-velocity flow areas, though, less intuitively, the optimized point where $\lambda_i = 1.59$ does not.

3.5 Discussion

3.5.1 Resource Assessment

The strong gradients in mean flow observed here are likely to be present at many other river turbine sites. This suggests that high-resolution site assessments prior to installation, precise placement during installation, and post-installation surveys should be considered as best practices for commissioning river current turbines. The gradients also suggest that coarse numerical models are unlikely to accurately represent the velocity shear at river sites. Although the flow is turbulent, the time variations in the flow are minor in comparison with the spatial patterns. This is, in part, because the time variations are slow (> 5 s) and occur synoptically over scales that correspond to an "engulfing gust" for the turbine (> 10 m). The hybrid approach of mapping the flow with Doppler profilers and obtaining high-resolution turbulence data with Doppler velocimeters at

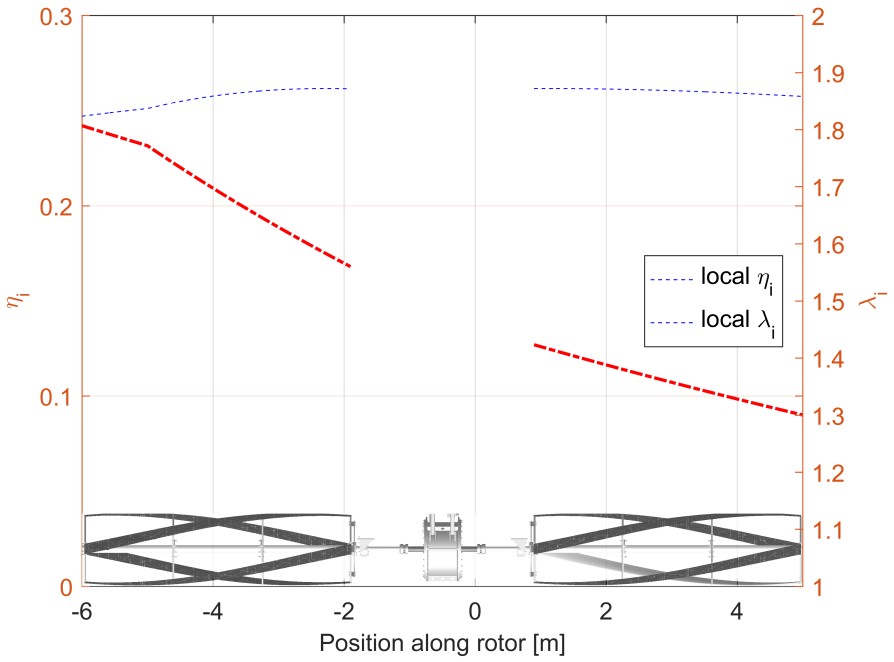

Figure 3.12: Rotor element efficiency η_i shown with λ_i over the rotor for $\lambda^* = 1.59$ defined at $x = 2$. Note η_i is near its maximum in the highest energy flow regions.

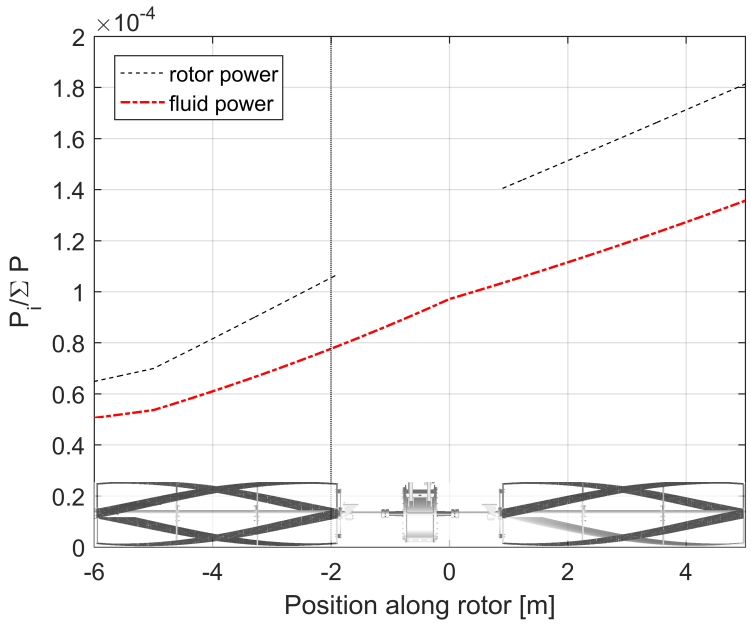

Figure 3.13: Power generation and fluid power available as a fraction of the total over 0.1 m turbine sections for $\lambda^* = 1.59$ defined at $x = 2$ (vertical line).

a few locations is recommended.

3.5.2 Performance Assessment

The maxima of the derived performance curve (Figure 3.10) is substantially higher than maximum efficiency observed in pre-installation tow trials and computational modeling (27% vs. 19%). The disparity is also apparent if one were to assume $\hat{\eta}_{\max} = 19\%$ for the deployment in Igiugig, AK. A 12 kW power output would require an equivalent uniform velocity of 2.3 m/s, which is higher than inflow velocity measured across nearly all of the turbine at 5 diameters upstream (Figure 3.5). Clearly, turbine performance is improved at this site relative to pre-installation tow trials. Blockage is not an entirely satisfactory hypothesis for this increase. As conventionally defined, the rotor swept area accounts for 3% of the river cross section. However, the rotor swept area accounts for 20% of the river depth. The free-surface deformation observed over the turbine suggests that vertical blockage or free surface proximity might affect performance or enable additional momentum transfer from the faster-flowing region of the river. Further investigation of this hypothesis requires information about inflow velocity on length scales equivalent to the turbine rotor both pre- and post-installation. Velocity surveys of this resolution carried out before and after turbine installation are recommended for robust performance assessments.

3.5.3 Turbine Control in Sheared Flow

Laterally-sheared flow results in a spatially-varying λ and η along the turbine rotor. Control architectures that attempt to control either of these variables will need to define setpoints based on a specific location in the flow. For example, a linear proportional-integral controller on λ will require the correct combination of setpoint λ_s and definition location (i.e., location where $\lambda_s = \lambda_i$), as shown in Figure 3.11. Non-ideal setpoints can be used without diminishing turbine performance, provided the velocity at the governing point results in an optimal λ_i for the potions of the rotor in the high-velocity flow. Because site conditions or turbine geometry may limit the allowable locations for a flow sensor, this technique could be used to implement an optimal control strategy. For example, if flow measurement was only possible in a lower velocity region, $\lambda_s = 2.0$ would result in optimal λ_i in the high-velocity region, maintaining a power output of 12.5 kW. Although the lateral shear profile observed at Igiugig appears to be synoptic on time scales of a week, a turbine deployed for longer periods might need to adjust to lower-frequency changes in the inflow. In the absence of any electromechanical changes to the turbine, a change in peak power output could indicate a change in shear profile or mean velocity magnitude. A periodic adjustment of λ_s could be used to compensate using performance data alone to identify a new optimum set point (albeit at the cost of lost generation during this re-evaluation) following an extremum-seeking control algorithm [51] [52].

In theory, a turbine could be deployed with adequate instrumentation to provide knowledge of its instantaneous inflow profile (i.e. an along-turbine array of upward looking Doppler profilers). If the turbine was characterized by the averaging method described above,the appropriate velocity to use for defining the ideal tip speed ratio would be the instantaneous spatial average, although it is likely this quantity would need to be averaged over several measurements to acquire a low-noise estimate.

3.6 Conclusion

Point measurements of inflow velocity cannot provide consistent power-performance curves when non-uniform velocities are present upstream of the rotor. At a specific site (Igiugig, AK (USA)), a limited number of point measurements provide temporally-resolved information about turbulence characteristics. These are combined with spatially-resolved mean flow measurements, shown to be robust over time-scales on the order of a week, to obtain a representative inflow velocity through spatial averaging. Spatially-averaged forms of the non-dimensional performance coefficients (tip-speed ratio and water-to-wire efficiency) are presented. Performance curves calculated from discrete observations of turbine power generation are consistent, suggesting that the temporal-spatial averaging method is reasonable. Velocity shear has implications for turbine control schemes. Defining a representative reference velocity will be a challenge for any control strategy that requires knowledge of free-stream velocity (e.g. tip-speed ratio control). A substantial performance variation is observed between these results and prior performance characterization in a uniform inflow. While several hypotheses for the cause of this discrepancy are possible, the underlying reason cannot be determined conclusively from available data. This result highlights how rigorous characterization of early turbine deployments can benefit resource and performance assessment methodologies.

4 Power-Maximization Control and Scaling

The proceeding chapter has been previously published in the *International Journal of Marine Energy* as "Multi-mode Development of Cross-flow Turbine Controller" [53].

The version presented here has a reduced background and introduction section to avoid redundancy, and the formatting has been modified for consistency with the rest of this document.

All simulation work presented in this chapter uses only time-average models of the turbine systems (i.e., N_Q was assumed to be 1 for all turbine azimuthal positions). There was insufficient data and sensing to reliably construct a field-scale phase-resolved turbine model, and, because the intent of the paper was partially to explore the validity of simulation results across scale, a time-average simulation was used throughout. The methodology presented in the previous section informed the time-average characterization effort.

4.1 Introduction

Here, we evaluate three candidate control algorithms intended to maximize power capture. In the wind and hydrokinetic turbine literature, this is often referred to as "Region 2" control, denoting a region of flow speeds between turbine cut-in and rated power, in which the control objective is to maximize power. These controllers were tested in simulation, scale-model experiments, and on a full-scale cross-flow turbine deployed at a field site. The usefulness of metrics to differentiate between control performance at each mode of testing are considered and compared to results of full-scale testing. The ability of the proposed methods to anticipate the best-performing controller from among several candidates is examined, and the necessary caveats for extrapolating laboratory results to full-scale devices are explored. This study is unique in its exploration of cross-flow turbine control across multiple development modes and device scales.

4.2 Background

4.2.1 Turbine dynamics and performance

Implementing control schemes in scaled testing and simulation can, theoretically, streamline integration on a full-scale system. For example, knowledge of discrete controller requirements (e.g., update rate) can aid in selection of full-scale turbine equipment and control software. However, knowledge of the extent to which these results are applicable across scales is necessary to confidently extrapolate scaled results to a full scale system.

Time-domain simulation of the turbine dynamics (Equation 1) is straightforward provided that estimates of J and $C_Q(\lambda)$ are available.

The dynamics of a cross flow turbine generally obey the first order non-linear differential equation given in Equation 1. Experiments offer a more realistic test of control algorithms, as there is uncertainty in control inputs and the environment is not perfectly controlled. This can be used to validate simulation results. Electromechanical emulation (i.e., hardware-in-the-loop simulation) of a turbine system, an approach not pursued in the present study, aims to bridge the gap between experimental and simulation environments, and may be considered a viable alternative [54] for some controller development.

4.3 Methods

4.3.1 Candidate controllers

Several controllers attempting to maintain λ^* were investigated. These included an optimal nonlinear control law and two linear controllers. All candidate controllers relied on a measurement of ω to determine the control torque, τ_c, while one required a measurement of U.

Nonlinear $K\omega^2$ control, in which the control torque is specified by Eq. 13 is widely used for wind turbines as a maximum power-point tracking (MPPT) scheme [11]. The gain, K, is selected based on knowledge or a model of the performance curve by Eq. 14. This controller tracks time-varying inflow, maintaining λ^*, without a real-time measurement of U [11].

Linear set point-maintaining controllers enjoy widespread industrial application and benefit from extensive treatment in the literature [55]. Therefore they were considered for regulating turbine operating conditions. Linear proportional integral (PI) controllers were considered of the form

$$\tau_c = K_p(\omega(t) - \omega_s) + K_I \int (\omega(t) - \omega_s)dt \tag{26}$$

where K_p and K_I are the proportional and integral gain, respectively, and ω_s is the set point angular velocity. For PI speed control (PI-ω), ω_s is a user-defined constant speed, and this controller therefore does not adjust for changes in U and cannot strictly maintain a λ^* set point for time-varying inflow.

For PI-λ control,

$$\omega_s(t) = \frac{U(t)\lambda^*}{R} \tag{27}$$

where the appropriate instantaneous ω set point is determined from a measurement of U. In the absence of turbulence (where $U(t) = U$, a constant) PI-λ and PI-ω controllers behave identically. PI controllers have the advantage of well-understood linear behavior, and appropriate gains K_p and K_I can be tuned (in an ideal case) by linearization of the Equation 1 about the desired operating point, provided a model of the

turbine performance curve in the vicinity of that set point is available. However, for non-ideal, non-linear component behavior, present in the laboratory and field test cases, gains must be tuned manually or be based on a more detailed model for turbine dynamics to achieve the desired turbine response.

The addition of sensing requirements and the uncertainties associated with the upstream measurement adds significant complexity to the implementation of the PI-λ control algorithm. However, this controller offers a closed-loop means to track energy-containing turbulence without a model of the turbine performance curve (as is required for the non-linear controller), which may be non-trivial to obtain in some conditions [40]. All controllers evaluated are relatively simplistic as the focus of is on the effectiveness of the evaluation methods in predicting performance, not identifying an optimal controller.

4.3.2 Advection time correction

A determination of a representative "undisturbed" inflow velocity upstream of a turbine must be taken far enough upstream to not be affected by its presence (i.e., outside of its induction zone), but near enough so that the measured velocity can be assumed representative of the flow incident to it. An assumption regarding the advection and evolution of this upstream measurement must be made to apply it at the turbine. Taylor's "frozen field" hypothesis, in which turbulent features are assumed to advect with the mean flow without evolution, was adopted for this purpose [32].

$$T_a = l/\langle U \rangle \tag{28}$$

describes the advection time T_a (s) of a turbulent structure in terms of the distance upstream l (m) and the mean free-stream velocity $\langle U \rangle$ (m/s), determined from a time-average over an approximately statistically stationary interval (30 s in the laboratory, 5 minutes in the field). It should be noted that this representation ignores induction which reduces advection velocity within 1-2 diameters of the rotor.

4.3.3 Performance metrics

Three metrics were used to quantify controller performance in simulation, experiments, and field testing. First, to quantify maximization of energy capture, energy loss E_{loss} is defined as either

$$E_{loss,Cp} = 1 - \frac{\int_0^T \tau_h \omega dt}{\int_0^T C_P^* P dt} \tag{29}$$

$$E_{loss,\eta} = 1 - \frac{\int_0^T IV dt}{\int_0^T \eta^* P dt} \tag{30}$$

where T is a specified duration (s). Whether mechanical (C_P) or electrical (η), an ideal controller that perfectly compensates for time-varying forcing and maintains $\lambda(t) = \lambda^*$, will have an E_{loss} of zero.

Second, variability in performance metrics (e.g., λ, τ_c, F_x) was quantified by the interquartile range (IQR) of the time series. It is desirable for a controller to closely hold a set point (e.g., λ^*) with minimal fluctuations. Excess fluctuations in τ and ω can reduce power quality and drive-train fatigue life, and structural fatigue life can be reduced by fluctuations in F_x [11]. Percent error is calculated between simulated performance and experiment or field testing as

$$\frac{\beta_{simulated} - \beta_{tested}}{\beta_{tested}} * 100\% \tag{31}$$

where β is the statistic under consideration (e.g. median or IQR of ω or τ_c), such that an underestimation by the simulation results in a negative percent error. Within a single turbine rotation, these parameters also may vary, and a time-average quantity may not be reflective of this persistent periodic fluctuation. To consider these intra-rotation effects in experiment, the phase-average is calculated

$$\hat{\beta}(\theta_k) = \frac{\sum_{j=1}^{N} \beta(\theta_j)}{N} \tag{32}$$

where $\hat{\beta}$ represents the phase average of the quantity under consideration at a particular angular position bin θ_k, θ_j is the angular position bin at which the average β is to be taken, and N the number of bins of θ considered. Throughout this analysis, $N = 100$, so each bin has an angular width of 3.6^o.

4.3.4 Cross-flow turbines

The full-scale system is the Ocean Renewable Power Company RivGen Power System ®. It is a four-bladed helical turbine with two rotors on either side of a centrally-located direct-drive generator (Figure 4.1, left). The turbine foils are fixed-pitch, and the system operates in a variable-speed mode, rotating about a horizontal axis.

The experimental turbine is also a four-bladed helical turbine, but with a single rotor in a vertical orientation (Figure 4.1, right). A servomotor acts as the PTO. Though functionally similar, the laboratory-scale turbine is not a geometrically-scaled version of the full-scale turbine. The blades have different profiles and helical sweeps, the aspect ratios are different, and the turbines utilize different blade support structures.

4.3.5 Full-scale turbine testing

The full-scale turbine was deployed in the Kvichak River, near Igiugig, Alaska (USA) during summer months of 2014 and 2015. Details regarding the 2014 deployment and characterization can be found in [40]. During

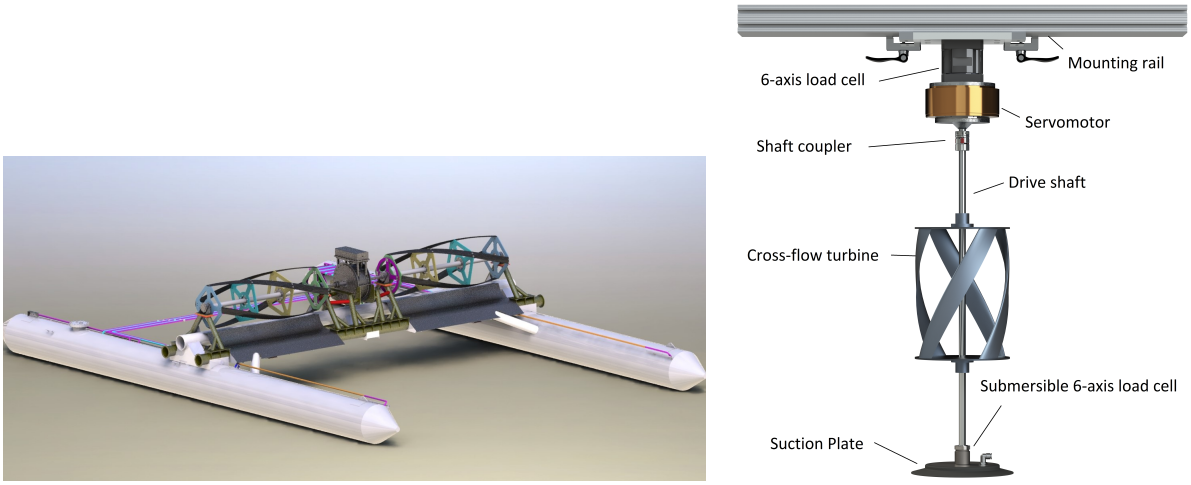

Figure 4.1: A rendering of the full-scale RivGen Power System (left) and the laboratory-scale setup (right).

both deployments, its electrical performance curve (i.e., η as a function of λ) was quantified by stepping through constant τ_c settings and measuring device electrical power output averaged over a roughly 5-minute test duration. V and I of Equation 30 were measured as direct-current (DC) values across either rectifier converting generator output (in 2014) or the DC-link of a back-to-back inverter (in 2015). Over this interval, U was statistically stationary [40]. In 2015, the turbine frame was instrumented with two upstream-looking two-beam acoustic wave and current (AWAC) devices. The AWACs provided a time-resolved estimate of effective free-stream velocity at 1 Hz according to a spatial averaging scheme described in [56] and summarized in Appendix A. The AWAC time series was used in simulations of the full-scale device. The average free-stream velocity was 2.0 m/s with a noise-corrected turbulence intensity [2] of 8%, as shown in Table 3. Turbulence spectra for the inflow were estimated from an acoustic Doppler velocimeter (ADV) survey [40]. The turbine has a blockage ratio (B_R)

$$B_R = \frac{A_{turbine} + A_{substructure}}{A_{channel}} \tag{33}$$

of 3%, where $A_{substructure}$ accounts for the submerged projected area of the generator, turbine frame, and pontoon support structure, and $A_{channel}$ is calculated based upon shore-to-shore river bathymetry parallel to the turbine axis of rotation [40].

Control actuation was implemented through a shore-based power converter consisting of a 'back-to-back' inverter arrangement. A 'grid-side' inverter maintained power output at the AC voltage and frequency of the village's isolated grid. A 'generator-side' inverter received variable frequency and voltage power from the turbine's generator and allowed actuation such that electrical current (resulting in τ_c on the rotor) could

be commanded based on real-time calculation of ω (based on 100 Hz measurements of electrical frequency). The drives were coupled via a common DC bus. Turbine torque was calculated by the inverter using 100 Hz measurements of voltage and current. The inclusion of this electrical machinery differed widely from the simplified linearized model used to derive K_p and K_I, and these gains were tuned manually in the field to achieve acceptable performance (e.g., stability, set point overshoot). A time-synchronized measurement of this DC power (prior to inversion and export to grid) provided an estimate of turbine power. Power output of the RivGen turbine system was (by design) insufficient to meet the full demand of the village; the balance of the load was supplied by diesel-fired generation. The turbine was not instrumented to measure structural loads or directly measure mechanical torque and rotation as is possible in a laboratory setting.

Candidate controllers were stepped through a variety of set points at and around λ^*, each maintained for 5 minutes. If a turbine stalled as a consequence of control actuation, restarts were attempted until the test duration was completed and the turbine was restarted to test the next set point. Several repeated cases are available near λ^*. While the AWACs provided an estimate of inflow velocity, time stamps on U were found to be inconsistent with ω, preventing meaningful evaluation of PI-λ control and obviating pointwise comparisons of electrical power to river currents.

4.3.6 Laboratory-scale testing

The laboratory-scale turbine was tested in the Bamfield Marine Science Centre recirculating flume at a mean velocity of 1.0 m/s. The flume test section is 12 m long, 0.98 m wide and was filled to a static depth of 0.75 m. This yielded a B_R of 6.7% calculated as in (33), where $A_{substructure}$ accounts for the submerged projected area of the drive shaft outside the turbine sweep, load cell, and vacuum plate. An ADV positioned 5 turbine diameters upstream of the turbine sampled inflow velocity at 32 Hz at the center point of the turbine projected area. The advection-corrected output of the ADV was used directly in real-time when needed for PI-λ control, while a de-spiked and advection-corrected estimate of U was used in post-processing calculations (e.g., η, E_{loss}). Additionally, this post-processed time series free-stream velocity served as the input for the numerical simulation.

The turbine was controlled by a servomotor capable of closed-loop speed or current regulation. Angular position was measured with an encoder with a resolution of 2^{32} counts per revolution and system loads were measured with a pair of six-axis load cells (one positioned between the servomotor and mounting frame and the other interfacing with a lower rotary bearing secured by a vacuum plate, Figure 4.1, right). This combination allowed high-resolution measurement of rotor torque as well as forces perpendicular to the axis of rotation (e.g., F_x). Angular velocity and load data were acquired at a sample rate of 1 kHz. As for the full-scale turbine, the laboratory-scale turbine performance was characterized at near-constant inflow velocity

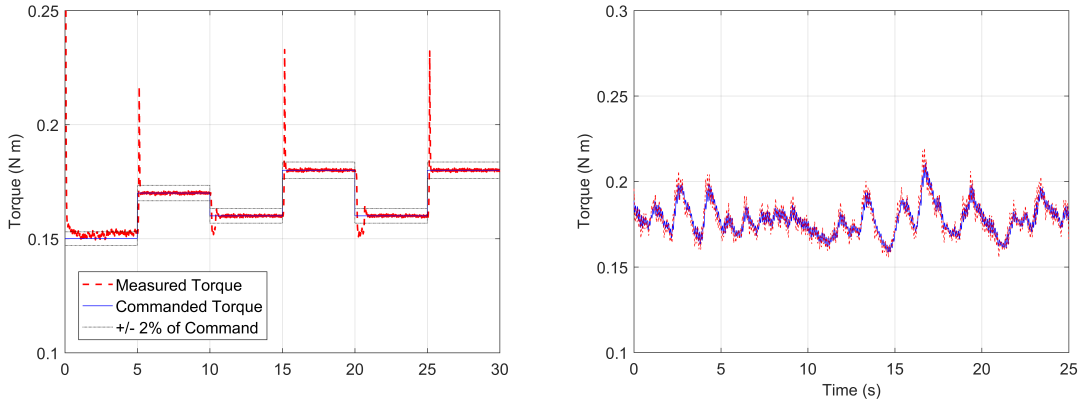

Figure 4.2: A time series of command torque and measured torque demonstrating the performance of the secondary PI controller through a set of step changes in command torque (left) and a controller test (right).The measured torque has been low-pass-filtered to 4 Hz to improve visualization.

while stepping through constant τ_c set points (Figure 4.3). Providing power from the servomotor where necessary, the characterization was repeated in constant ω mode by stepping through a series of constant velocity set points. At the peak of the performance curve, C_p^* was identical between the two approaches to within measurement uncertainty. C_T was characterized via torque control, the control mode attainable in both laboratory and full-scale testing (Figure 4.4). Uncertainty in C_T was calculated using the method of [57].

Candidate controllers were tested on the laboratory-scale turbine in 30 s durations at an update rate of 100 Hz.

Secondary PI control of laboratory turbine

Because of the non-linear relationship between commanded servomotor current and applied torque, a secondary PI loop operating at 1 kHz (10x faster than the primary controller update) adjusted the motor current command so that the load-cell measured torque matched the command torque. The gains of this PI controller were adjusted manually to minimize settling time for a series of step changes in command torque (Figure 4.2, left). The $+/-2\%$ settling time is less than 0.75 seconds for all set point changes. Note that the magnitude of these step changes are much larger than those commanded during controls testing, so the dynamic effect of this secondary controller is relatively insignificant (Figure 4.2, right).

4.3.7 Comparison of laboratory-scale and full-scale testing

A comparison of laboratory-scale and full-scale turbulence is shown in Figure 4.5 and flow statistics are summarized in Table 3. The standard deviations of mean flow and turbulence intensity averaged over the testing interval T (30 s for the laboratory, 300 s for the field) are also listed, as a measure of statistical

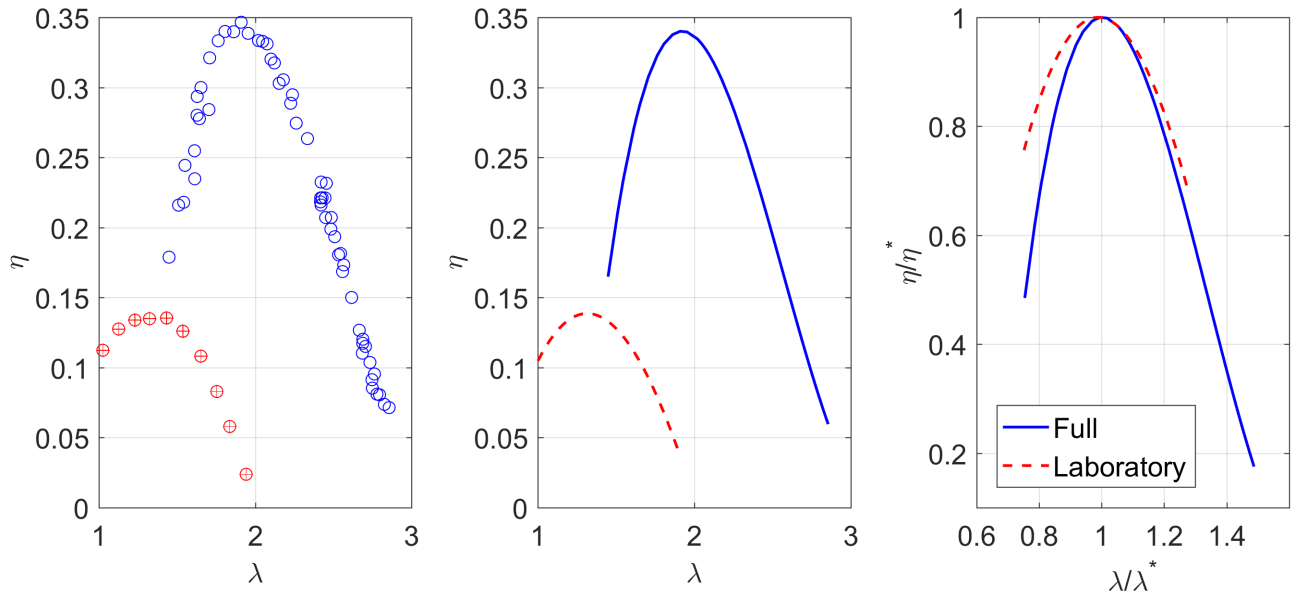

Figure 4.3: Point values with error bars (left), absolute performance curves (middle) and normalized performance curves for the full and laboratory scale turbines (right). Note that η and η^* imply C_P and C_P^*, respectively for the laboratory cases. Error bars are shown, but uncertainty is small, not generally exceeding the size of the circular marker.

stationarity.

The laboratory flume has a slower mean velocity and is less turbulent than the full-scale site. Inspection of Figure 4.5 shows that energetic turbulence at the full-scale site is contained below 1 Hz. The less-energetic laboratory flume turbulence does not have as definitive a roll-off frequency, but most energy-containing turbulence has a frequency less than 4 Hz. The mean U is consistent between controller tests for both the laboratory and full-scale turbines. The turbulence intensity is more consistent for the flume than the full-scale site.

Performance curves from the full-scale and laboratory scale turbines are shown in Figure 4.3. Point data are fitted with a third-order polynomial. For the laboratory tests, error bars for C_P and λ are shown, calculated using the method of [57]. The manufacturer of the VFD used in the full-scale implementation does not provide estimates of the quantities necessary to calculate uncertainty for the full-scale turbine. The full-scale turbine has a peak η^* occurring at $\lambda^* = 1.95$, and the laboratory turbine has C_P^* occurring at $\lambda^* = 1.31$. When normalized (Figure 4.3, right), both curves are similar, though the laboratory turbine performance curve is slightly flatter.

Simulation of Equation 1 requires an estimate for the turbine's rotational moment of inertia (J). For the full-scale turbine, this was determined from solid modeling of the rotor and generator specifications. Because power was available from the servomotor, the flume turbine J was determined by driving the turbine in air

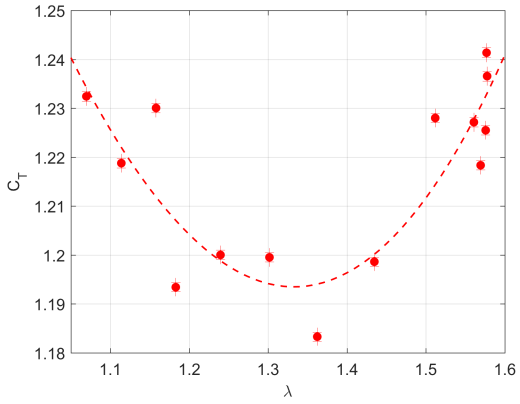

Figure 4.4: C_T vs. λ for the laboratory scale turbine, shown with uncertainty range and polynomial approximation.

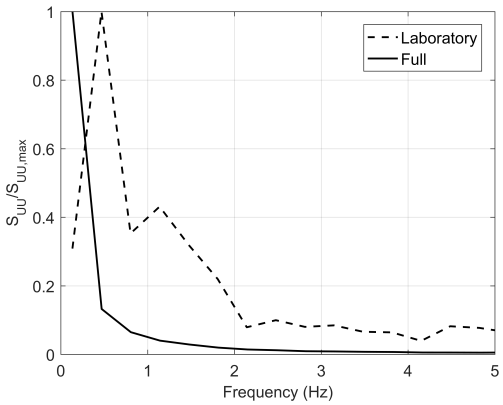

Figure 4.5: Normalized turbulent energy spectra for laboratory and full-scale cases. The sampling rates are 32 Hz and 16 Hz, respectively.

Table 3: Flow Statistics

Quantity	**Laboratory**	**Full**
Mean (m/s)	1.0	2.0
Turbulence Intensity	5%	8%
Std Dev. T Avg. Mean (m/s)	0.01	0.02
Std Dev. T Avg. TI	0.1%	2%

Table 4: Turbine Parameters

Parameter	**Laboratory**	**Full**
J (kg m^2)	0.010	277.5
$A_{turbine}$ (m^2)	0.040	11.48
$A_{substructure}$ (m^2)	0.007	25.09
$A_{channel}$ (m^2)	0.735	338
R (m)	0.086	0.7

through a series of velocity sine waves of variable frequency and amplitude. Using the known acceleration of the turbine and the measured torque, J could be calculated for each waveform. Estimates were within numerical precision for all waveforms.

For the full-scale turbine, C_P was estimated from η and an estimate of η_0 from dynomometer testing of 90% around the peak of the performance curve. Turbine dynamic parameters are shown in Table 4.

4.3.8 Simulation

Equation 1 was integrated using Matlab Simulink for candidate controllers and set points. The simulation used the turbine parameters (Table 4), the performance curve (Figure 4.3, middle), and was forced by a free-stream time series from either the laboratory (ADV data) or the field (spatially-averaged AWAC data). Simulations of laboratory data were also provided with the polynomial approximation of the thrust curve (Figure 4.4) to simulate $F_x(t)$. Laboratory free-stream time series were low-pass filtered back-to-back with a first-order Butterworth filter with a cut-off frequency of 4 Hz (the selection of the cut-off frequency is informed by the characteristics of the inflow discussed in Section 4.3.7). Because the field data was already spatially averaged across multiple time-synchronous measurements (Appendix B), additional time-domain filtering was unnecessary to reduce measurement noise.

4.4 Results

4.4.1 Time-resolved comparison of performance metrics

The laboratory experimental data set provided time-synchronous measurements of inflow velocity and turbine behavior. This allowed simulations to be carried out for which the inflow time series, turbine, and control parameters could be matched to the experiment and the simulated time series of turbine parameters compared directly to measurements. A comparison of operation of each controller is shown in Figure 4.6. The comparisons are slightly truncated due to the advection time correction for the inflow measurement. The start of the time series ($t = 0$) corresponds to the first instant that advected inflow is available to drive the simulation.

For all controllers, the simulation of the laboratory-scale turbine closely tracks the time-resolved measurements of ω, τ_c and F_x for when the turbine operates near the peak of the performance curve. Simulated ω, τ_c and F_x, are smoother than the experimental data primarily because they do not include any measurement noise. Additionally, simulation does not capture intra-rotation variability in the hydrodynamic torque, present in the actual turbines (Figure 4.7). These ~ 10 Hz oscillations in measurements are notably elevated relative to simulated values. Spectral analysis of measurements shows these energetic oscillations

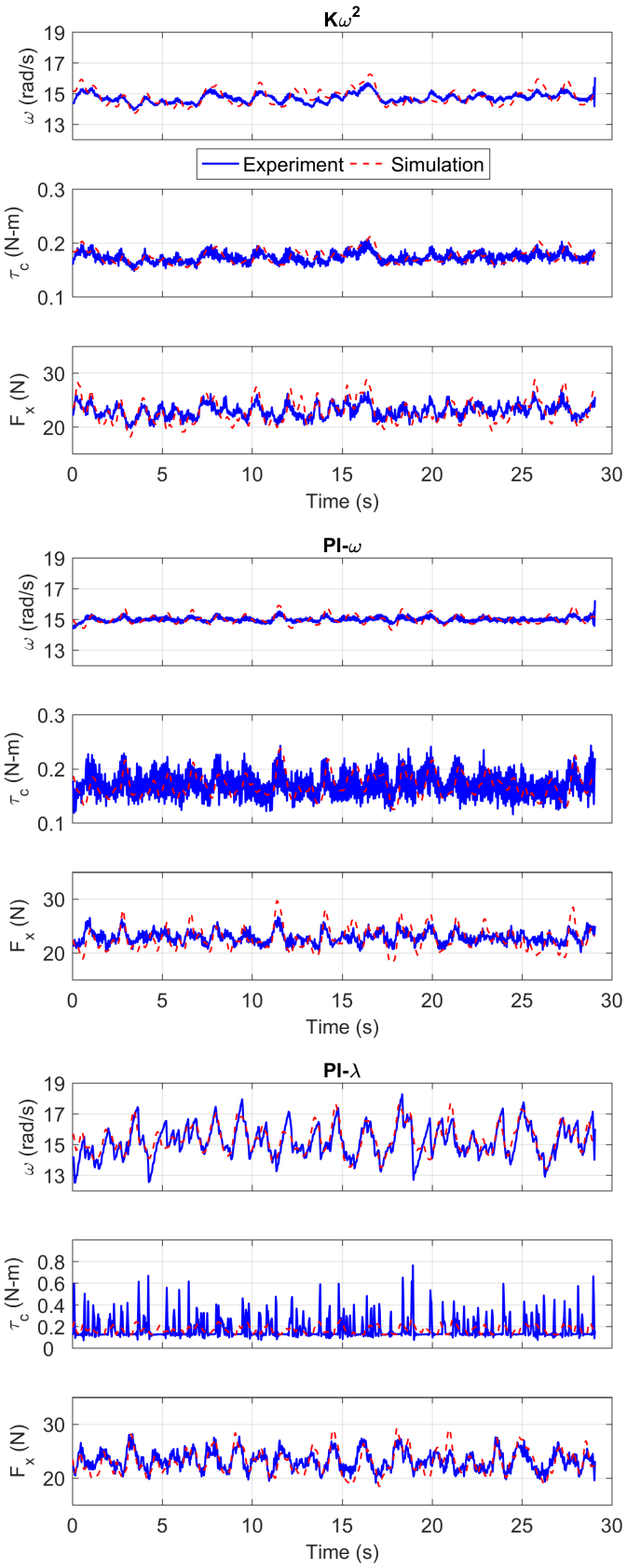

Figure 4.6: A comparison of simulation results to laboratory results for Kω^2 (top), PI-ω (middle), and PI-λ (bottom). Note that the scale differs on the PI-λ time series of control torque to show the extrema.

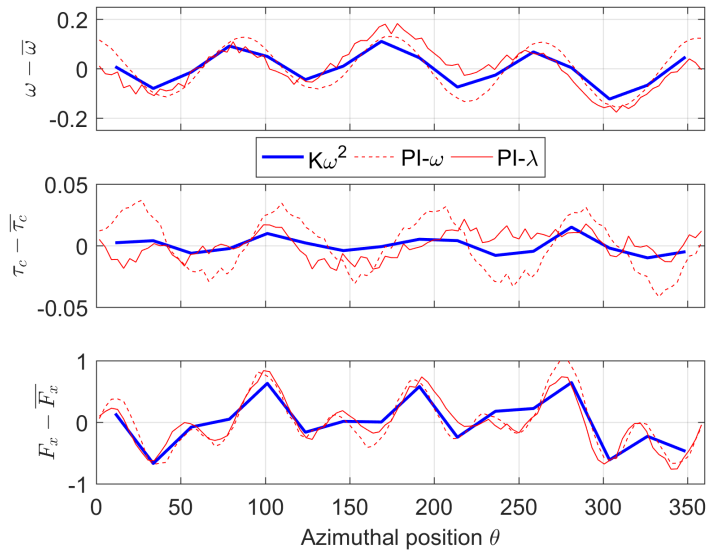

Figure 4.7: Phase-averaged ω, τ_c and F_x (relative to the mean) from laboratory testing. At $\theta = 0^o$ the leading edge of a blade is pointing directly upstream.

occur at a frequency corresponding to blade passage (i.e., four times the rate of rotation). This implies that intra-rotation effects, such as flow separation (e.g., dynamic stall) or vortex shedding by the blades, affect variance of measured quantities in a way that is not represented by the low-order simulation. However, for operations near λ^*, intra-cycle variation is small compared to the mean values and variations caused by turbulence (those captured by the simulation), and do not depend strongly on controller type. The relatively small intra-cycle torque variation is one of the motivations for helical designs [58].

Low-frequency oscillations in τ_c are well-estimated in frequency and amplitude, except in the PI-λ case. This is likely an effect of the secondary PI-loop used on the laboratory turbine. The increased complexity of the PI-λ controller, relying on both a raw estimate of U and an ω measurement produced a greater range of torque commands.

4.4.2 Statistical comparison of performance metrics

Variability in τ_c, ω, λ and F_x between simulation and laboratory-scale turbine experiments under Kω^2, PI-ω, and PI-λ control are summarized in Figure 4.8. Laboratory turbine data was filtered to 100 Hz, the control actuation frequency, to limit the contribution of high-frequency measurement noise.

The simulation is an excellent predictor of median ω, τ_c, λ, and F_x for the laboratory-scale turbine for all candidate controllers except τ_c for the PI-λ controller, as would be expected from the time-resolved comparison (Section 4.4.1). F_x medians are slightly but consistently under-predicted. For ω, the simulation tends to over-predict the IQR, likely due to the assumption of spatially-uniform, time-varying inflow. In

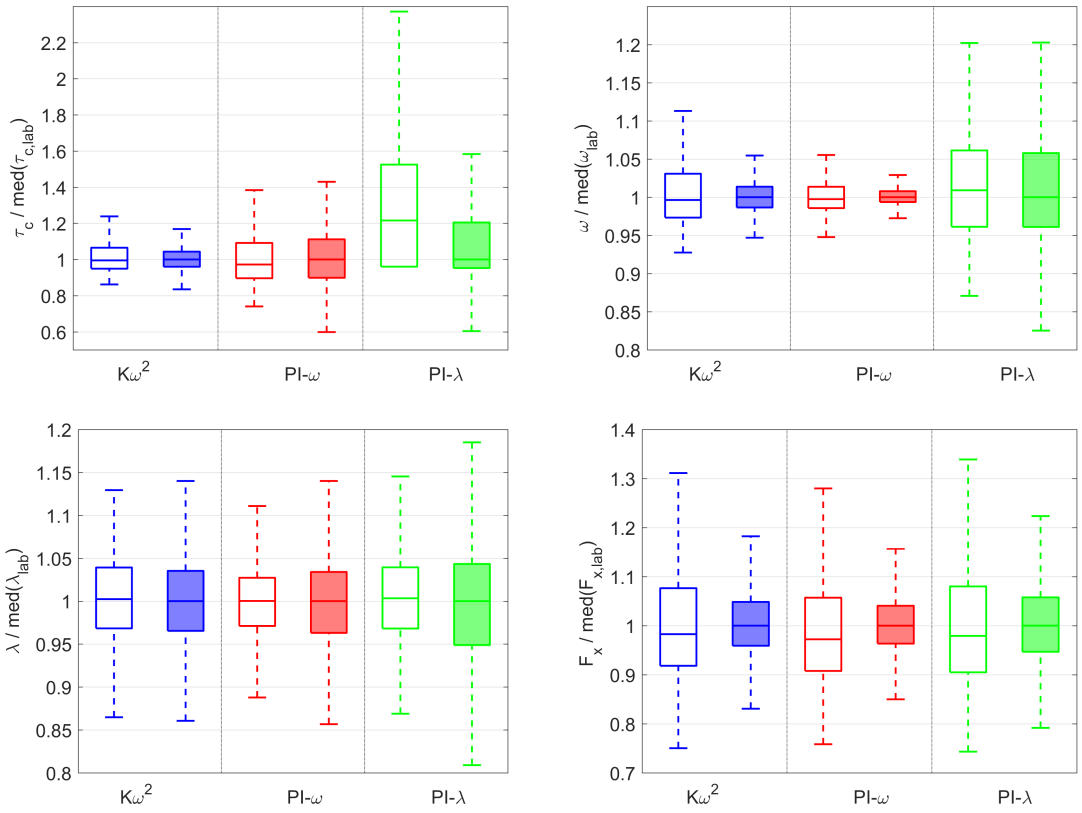

Figure 4.8: A comparison of torque demands (top left), angular velocity (top right) and tip speed ratio (bottom left) and thrust loads (bottom right) under Kω^2, PI-ω, and PI-λ control for the laboratory-scale turbine. Simulated results are given in unshaded box plots, and experimental data is shown in shaded plots. Boxes are normalized by the median of the laboratory data. Note that though all cases are near λ^*, tests between different candidate controllers were not evaluated at the exact same λ, given how the discrete set points were chosen for PI-ω and PI-λ control.

Table 5: Percent error of performance metrics in simulation of experiments.

Set point metric	**Kω^2**	**PI-ω**	**PI-λ**
τ_c median	-0.6	-2.8	27.7
τ_c IQR	38.9	-8.2	113.1
ω median	-0.4	-0.3	0.6
ω IQR	111.3	97.5	17.4
λ median	0.2	0.0	0.7
λ IQR	1.4	-20.9	-10.0
F_x median	-1.98	-2.37	-1.43
F_x IQR	31.0	19.8	-1.90

reality, the point measurement of U used to drive the simulation is varying over the turbine rotor area, such that not all fluctuations substantially affect hydrodynamic torque. This trend can also be seen to some extent in F_x. While the omission of intra-cycle variations in simulation somewhat counteracts this, the intra-cycle variations are comparatively smaller in magnitude than these variations due to turbulence, as evidenced by the relative scale of Figure 4.6 and Figure 4.7.

The simulation predicts the IQR of τ_c fairly well for all cases except PI-λ, where it is over-predicted. The PI-λ τ_c experimental result may seem contrary to Figure 4.6, but is to be expected: the box plot (Figure 4.8) excludes outliers more than $\pm$2IQR from the median and the larger peaks seen in the time series are outliers. In this case, the statistical summary in Figure 4.8 is a misleading presentation of controller performance. This indicates that, when possible, time-resolved controller performance should be evaluated.

The IQR of λ values are predicted well by the simulation. This is not unexpected. The engulfing flow assumption led to the over-estimate of simulation ω IQR, but these variations in ω are synchronized with (likely over-estimated) variations in U time-series used to drive the simulation, reducing simulation λ IQR when compared to simulation ω IQR.

Experimental results indicate that all controllers use approximately the same median torque to hold a near-peak set point, which is to be expected. Kω^2 has the smallest IQR of τ_c, followed by PI-ω. PI-λ control has a significantly broader τ_c range, due to the added uncertainties associated with incorporating U measurement into the torque calculation. Although the magnitude of the torque ranges between controllers is not consistently well-estimated by simulation, the trend of τ_c IQR between controllers is accurately predicted. F_x IQRs do not appear to be sensitive to controller type, which is well-reflected by simulation.

Similar comparisons were made between simulation and full-scale field testing under Kω^2 and PI-ω control (PI-λ control was not implemented in the field). Because the specific inflow time series is not known for the full-scale tests, it is not meaningful to compare λ IQR, and F_x was not measured in the field. As for the laboratory-scale turbine, the cases shown in Figure 4.9 and Table 6 are associated with stable operation at the peak of the performance curve.

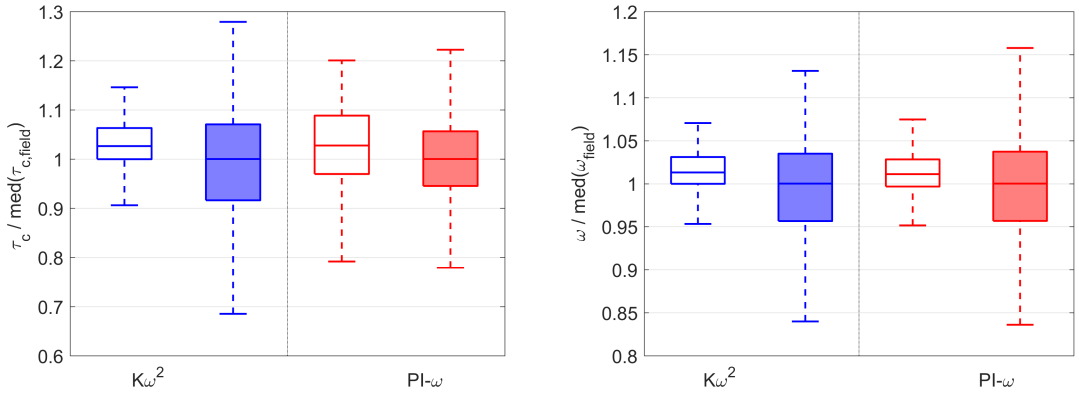

Figure 4.9: A comparison of control torque (left) and angular velocity (right) for the full-scale turbine under Kω^2 and PI-ω control for the full-scale turbine. Boxes are normalized by the median of the field data. Simulated results are given in unshaded box plots, and field data is shown in the shaded plots.

Table 6: Percent error of performance metrics in simulation of field tests.

Set point metric	**Kω^2**	**PI-ω**
τ_c median	0.9	0.2
τ_c IQR	-42.9	31.0
ω median	0.4	1.0
ω IQR	-44.2	-61.2

As for the laboratory turbine, median values for τ_c and ω are fairly well-predicted by simulation, though not as accurately as for the laboratory experiments. However, with the exception of τ_c in PI-ω control, the IQR for performance metrics is consistently under-predicted by simulation and the trend in IQR for τ_c across candidate controllers is not qualitatively correct. In absence of time-synchronized free-stream data, it is possible that some of these differences could be because the simulated time series is not sufficiently representative of the free-stream experienced by the turbine during these cases (e.g., relatively large standard error in turbulence intensity in Table 3). Further, it is likely that noise and measurement uncertainty are present in the field that were not represented in simulation (e.g., torque and angular velocity were not measured directly, but calculated internally by the inverter based upon electrical current measurements).

As in the laboratory-scale turbine experiments, the full-scale turbine under Kω^2 control has a larger IQR of τ_c than PI-ω control. This is undesirable, as higher amplitude torque oscillation will increases the fatigue damage of drive-train components.

4.4.3 Energy Loss

Table 7 provides the E_{loss} values for the full-scale and laboratory-scale turbines in simulation and in measurements. Simulation suggests an appreciable difference in E_{loss} between controllers applied to the full-scale

Table 7: E_{loss} (%) by candidate controller for simulation and measurement in laboratory and field settings

Test Mode	*Simulation*		*Measurement*	
Controller Type	**Field**	**Laboratory**	**Field**	**Laboratory**
Kω^2	0.05	1.02	4	2
PI-λ	1.36	1.07	-	-2
PI-ω	1.74	1.05	6	0

system and more limited differences at the laboratory scale. While the qualitative trends appear to be borne out by the field measurements, the non-physical results from laboratory application of this metric (i.e., negative E_{loss}) suggests that the field trends may be simply fortuitous. For the full-scale turbine, simulation suggests that PI-ω control, which is not capable of tracking energetic turbulent fluctuations, should perform the poorest, while Kω^2 should perform the best, with nearly 0% E_{loss} (i.e., effectively converting all of the hydrokinetic resource possible for the turbine design). The hypothetically superior full-scale performance (in simulation) of the Kω^2 controller is likely due to the assumption of a continuous and deterministic performance curve: a controller with perfect information about the plant would reasonably outperform an error controller, and a turbulence-tracking controller (PI-λ) will tend to outperform one that does not (PI-ω).

In simulation, the lack of distinction between minimum simulated E_{loss} for the laboratory-scale turbine controllers indicates that the turbine does not respond as rapidly as the full-scale turbine to the turbulence present in the flow, elevating minimum E_{loss} and lessening the differences in performance between turbulence-tracking and PI-ω controllers. The simulated laboratory inflows have less turbulence at frequencies to which the laboratory turbine is capable of responding, due to its relatively higher inertia than the full-scale device (Table 3), diminishing the potential improvement from turbulence-tracking. If the laboratory turbine is simulated with a more turbulent synthetic time series, the turbulence-tracking controllers show less E_{loss} than the PI-ω controller: however the E_{loss} can be elevated for all controllers if more energy is present as high-frequency turbulence that the laboratory turbine is unable to capture.

E_{loss} represents the maximum power capture for a candidate controller, given perfect information about U and a continuous and deterministic performance curve (the polynomial fits in Figure 4.3). Because inflow in laboratory and field settings is an estimate, this introduces significant uncertainty into E_{loss} outside of simulation. Additionally, in the field, synchronous measurements of turbine performance and U were not collected. Finally, the relatively broad peak in the performance curve (Figure 4.3) means that controllers for these turbines that do not hold the prescribed λ^* set point are not significantly penalized in terms of E_{loss}.

While E_{loss} was not effective at differentiating controller performance, it can provide useful information about candidate controllers' implementation. For example, in simulation, the effect of the rate at which the controller updates τ_c does manifest as substantial variations in E_{loss}. By examining Figure 4.5 and 4.10, it

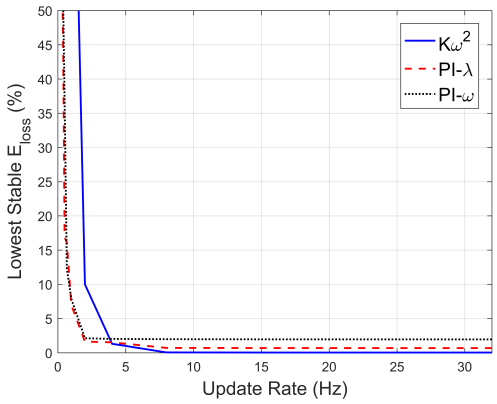

Figure 4.10: Simulated E_{loss} as a function of update rate for the full-scale turbine under Kω^2, PI- ω, and PI-λ control.

is apparent that performance of the full-scale turbine would be expected to degrade considerably when the update rate is less than $\sim$ 10x the frequencies of energy-containing turbulence (i.e., below the inflection point at $\sim$ 0.5 Hz). Substantially degraded performance indicates that the controller was not able to operate stably at λ^* (i.e., the controller drives the turbine to stall). This suggests a minimum control update rate that scales with the environment-specific turbulence and turbine dynamic properties (e.g., J). The laboratory and full-scale update rates used in experiment (100 Hz) are well above this threshold, with both laboratory and field implementations informed by early simulation results.

4.5 Discussion and conclusions

4.5.1 Performance metrics advising controller evaluation and implementation

While conceptually attractive, E_{loss} is only able to differentiate controller performance in simulation for these turbines. Simulation suggests that the Kω^2 controller should have the lowest E_{loss}, but this could not be verified through laboratory or field testing. Variability in other performance metrics (e.g., F_x, τ_c, ω, λ) was a more effective means of differentiating candidate controllers. From experimental and field data, it is apparent that higher-frequency turbulent fluctuations in point measurements do not produce hydrodynamic torque or significant changes in thrust loads, likely because the length scale of this higher-frequency turbulence is such that it will only affect a small portion of the turbine swept area (Equation 28) and the time scale of these disturbances is not long enough to overcome turbine inertia. Because simulations assume this point measurement represents uniform inflow to the turbine rotor, a low-order simulation response over-estimates variability in performance metrics. This suggests that simulation inflow should be adjusted to include only responsive scales of turbulence, as well as corrected for advection time. These responsive scales could be

approximated by the length scale of the characteristic turbine size (e.g. rotor length), but by Equation 28 and Tables 3 and 4, we see that this suggests 4 Hz as the low-pass cut-off frequency, which was applied to the inflow time series when simulating laboratory-scale turbine performance. This suggests that excluding "non-engulfing" turbulence requires a lower cut-off frequency, implying a longer streamwise length scale. Because a point-wise ADV free-stream measurement advects with the mean flow, a time-domain low-pass filter, like that used in simulation, applies a length-scale constraint in only the streamwise direction. Because energy-containing turbulence is often anisotropic in marine energy applications [30], this streamwise length scale will differ significantly from the cross-stream and vertical length scales. As such, a transfer function more complicated than a low-pass filter may be required to allow only turbulence that affects torque and loads to drive a simulation.

Turbine inertia was estimated from turbine mass in air. In water, this inertia will also include the added mass of water accelerated with the rotating elements of the turbine [59]. Neglecting added mass will lead to an overestimate of turbine sensitivity to higher-frequency turbulent fluctuations. Because controllers depend on an ω measurement to determine τ_c, an over-predicted ω IQR, in general, would lead to an over-prediction of τ_c IQR as well. However, no methods currently exist to accurately parameterize added mass in low-order simulation.

Contrarily, time-resolved simulation and statistical analysis show under-estimation of τ_c IQR for PI-λ control. In this particular case, under-prediction of τ_c is likely due to noise present in the measurements used as control signals, especially the raw ADV estimate of U. If this noise were significant enough in the PI-λ case to force the controller to its low-torque saturation limit, (the servomotor was not allowed to motor the turbine) the turbine would then over-compensate due to the large integrated error, resulting in the observed behavior. It is unlikely that the noise level that will be present in measurements will be known exactly *a priori*, but adding noise based on estimated levels to simulation could aid in exploring controller sensitivity to this parameter, and advise alternative controller gains and filter implementations for these noise-contaminated signals to limit torque oscillation amplitude [56]. Further, an anti-windup scheme could be utilized for the integrator [55].

The performance metrics considered here focus on power generation, powertrain component performance, and thrust loads at the peak of the performance curve. Generalizing these conclusions to all operating conditions and control objectives (i.e., constant power in changing current) will require examination of off-peak control cases and specific study of power-tracking control algorithms. This future investigation is motivated by deployment environments, which experience a wide range of inflow velocities, such that it would not be economic to operate the turbine under Region 2 control at all times.

4.5.2 Consideration of turbine scale

Though dynamic scaling has not been applied in the usual sense (e.g., matching Froude/Reynolds number between laboratory and field experiments), the turbine dynamics under consideration are derived from the shape of the normalized performance curve (Figure 4.3), turbine inertia, and the scales of energetic turbulence. Scales of turbulence were considered in selection of the controller update rate (Figure 4.10) and the sensing method through which turbulence was estimated. These results suggest that useful conclusions can be drawn from this evaluation methodology, even though specific flow physics and absolute performance may vary at different scales. In particular, low-order simulation represents flow interaction simply as a performance curve and does not have any dependence on device scale.

4.5.3 Effectiveness of testing modes

The low-order simulation was able to predict the verifiable performance metrics at both the laboratory and full-scale turbines near the peak of their performance curve. Predictions were less accurate for simulations of the field turbine, possibly indicating uncertainty in the perfomance curve (the uncertainty could not be calculated, Section 4.3.7). Simulation provides an adequate first-order design tool and can, without modification of the underlying physics, accurately model important turbine dynamics across multiple scales. It should be noted, however, that the simulation represents an idealization of sensing capability and the difficulties associated with controller implementation, particularly, the determination of an instantaneous free-stream velocity interacting with the turbine, should be considered. Further, it is critical that the tested and simulated time series are of appropriate length to be statistically stationary. Because U in both testing modes was statistically stationary over the time scales of a test, the statistics of simulations agreed closely with laboratory and full-scale test results.

For the PI control cases, the implementation of the sensing and control hardware required that the gains be re-tuned manually, and, though they were effective for control of the full and laboratory-scale turbines, the resulting gains were different from the simulated gains for the full-scale turbine. Without an adequate model of the electro-mechanical interactions in the control hardware, simulations more representative of the field implementation cannot be carried out to confirm this hypothesis. This suggests that, for PI-controls, simulation is insufficient to identify optimal gain settings without a detailed model of the specific implementation method. In absence of a higher-order model, emulation on device hardware could inform gain selection [54]. In this respect, a $K\omega^2$ controller is easier to implement, if an estimate for the performance curve is available.

To improve the simulation, these results suggest that the most significant improvement would be strength-

ening the U estimate used by simulation. A superior inflow model that provides space-and-time resolved turbulent structures representative of a test site would provide a more representative simulation input that did not rely on 'engulfing gust' assumptions. The 2015 AWAC measurement approach on the RivGen turbine could, in theory, provide this spatial-temporal resolution of inflow, and may be useful for future deployments. Time-synchronized AWAC and turbine measurements would greatly inform turbine sensitivity to turbulent length scales and advise simulation implementation.

Controller performance results from scaled laboratory experiments are also adequate predictors of full-scale, provided controller update rate is scaled appropriately with energetic turbulent time scales. However, unique dynamics resulting from different dynamic parameters, performance curves, and inflow conditions should be explored in simulation and considered when attempting to extrapolate controller performance metrics across scales. This highlights a key limitation of laboratory-scale experiments: they are useful for exploring fluid-turbine interactions, but the exact controller dynamics of a full-scale device often cannot be predicted by experiment alone. Electromechanical emulators, described in [54], are capable of replicating turbine dynamics with the benefit of using sensing from actual hardware, but rely on a model of fluid-turbine interaction in the same manner as simulation. This suggests that a more rigorous method of controller evaluation would involve simulation, laboratory-scale experiment, electro-mechanical emulation, and finally field testing — a logical progression.

By almost all performance metrics across evaluation modes, the Kω^2 controller is superior. This demonstrates the potential for consistent relative performance evaluations using this methodology. Because this controller does not rely on a continuous measurement of inflow velocity, implementation is simplified relative to a PI-λ controller. An accurate measurement of inflow velocity is still necessary to characterize performance, but this can be a stand-alone effort, rather than a continuous measurement. The full-scale turbine implementaion of Kω^2 control, did, however, have a larger IQR of command torques than the PI-ω controller, which could reduce service life due to higher fatigue on drive-train components. The extent of this reduction will depend on the specific geometry and materials of the turbine. However, because this deficiency was not present in either the simulation of the full-scale turbine or in laboratory experiments, it is possible that it was specific to the method of that implementation on hardware specific to the full-scale turbine, and is not inherent to this controller architecture. Finally, experiments suggest that none of the candidate controllers are substantially distinguished by the thrust loads imposed on the turbine while operating at the peak of the performance curve.

5 Power-tracking Control of Cross-flow Turbines

In the previous chapter, a combined approach of simulation and laboratory-scale experiment was found to be fairly predictive of field-scale controller performance for power-maximizing controllers provided that the turbines have qualitatively similar performance curves and the relevant controller parameters (e.g., update rate) are appropriately adjusted for each device. With this result in mind, a controller capable of meeting power-maximizing and power-tracking objectives as well as transitioning between them is pursued in simulation and experiment. The investigation is performed with two cross-flow turbines: one with four helical blades (used in the previous chapter) and another with two straight blades. The sensor and actuation requirements for the proposed controller are minimal to facilitate eventual implementation on a broad range of field-scale devices.

The Region 3 control law pursued in this chapter is an overspeed control law, meaning the turbine increases its operating λ to maintain P_{rated} when the power available under a power-maximizing control law would exceed P_{rated}. Further, a qualitative discussion comparing performance of a variety of underspeed and overspeed Region 3 control laws is presented in Appendix D. A detailed examination in simulation and experiment of off-peak turbine performance was conducted in [35] and [34], and summarized here, as both advised selection of the overspeed approach. In general, simulation was found to be more predictive of time-resolved laboratory turbine response at higher tip speed ratios, suggesting (as per the previous section) that an overspeed control strategy may be more easily implemented on a field-scale turbine. The simulation also accurately predicted the low-speed limit of stable controller operation near the peak of the time-average C_Q curve, the onset of non-minimum phase behavior for torque control algorithms. This suggests that, barring a complex field implementation strategy, the peak of the time-average C_Q curve is a good approximation of field-scale stability limits. In the particular case of the 2015 RivGen turbine, this approximation was found to be accurate and well-predicted by simulation. Consequently, there is a domain of λ for which underspeed Region 3 control is predicted to be stable in a time-average sense: between the peak of the C_P curve and the peak of the C_Q curve. This results in a reduced range of available power set points, implying a more limited range of flow conditions in which the turbine can operate. Finally, both simulated and experimental results showed more extreme oscillations in torque actuations and thrust loads on the turbine during underspeed operation.

Thus, an overspeed control law is pursued in this section due to its superior stability properties (e.g., there is no non-minimum phase behavior right of the time-average C_Q maximum), reduced amplitude of torque actuations, turbine responses that are more predictable by simple simulation, and that implementing underspeed control significantly left of the C_Q maximum in the laboratory was unsuccessful. Drawbacks of

overspeed control include generally higher thrust loads and faster turbine rotation rates which may wear drivetrain components more rapidly. Further, in the event of an emergency shut-down, unless it can be mechanically braked, the turbine must transiently increase both power and torque as it decelerates through the peak of the C_Q and C_P vs. λ curves prior to stopping.

This chapter has been submitted for publication to the *Journal of Renewable and Sustainable Energy* under the title "Power Tracking Control of Cross-flow Turbines". The version presented here has been formatted for consistency with other sections of this document and the introduction and background sections have been removed to limit repetition.

5.1 General Turbine Dynamics

The dynamics of a cross flow turbine generally obey the first order non-linear differential equation given in Eq. 1. Hydrodynamic torque is the torque produced by the blades less fluid drag on rotating components and is defined mathematically by Eq. 2, depending tip speed ratio (Eq. 3) and turbine azimuthal position θ. Reference fluid power is defined by Eq. 5. This implies a phase-resolved non-dimensional power coefficient

$$C_P(\theta, \lambda) = \frac{\tau_h \omega}{P_{fluid}} \tag{34}$$

where the numerator is the mechanical power produced by the turbine. It can be shown further that

$$C_P = C_Q/\lambda \tag{35}$$

[21]. Because of the phase variation in C_P, periodic changes in turbine rotation rate and power output occur even in constant inflow. It is common to average $C_P(\theta, \lambda)$ over all phases and present it in a time-average sense as a function of λ [21], which yields a non-dimensional performance curve with a single maximum C_P^*, occurring at λ^*. In Region 3 control, where a fixed-pitch cross-flow turbine is purposely operated away from λ^* to maintain constant power, the turbine can be operated under-speed, where time-average $\lambda < \lambda^*$, or over-speed, where time-average $\lambda > \lambda^*$. The mechanical shaft power available to the power take-off is defined by Eq. 8.

If turbine rotation rate is held constant, then the torque applied to the power take-off is equal to the hydrodynamic torque (Eq. 1). However, if the rotation rate evolves in time, as is the case for the controller evaluated here, then rotational acceleration or deceleration requires an imbalance between control torque and hydrodynamic torque. Consequently, power tracking effectiveness is evaluated relative to shaft power at the power take-off (Eq. 8), rather than hydrodynamic power produced by the rotor. For a purely resistive

control strategy (i.e., one in which the power take-of cannot motor the turbine at any azimuthal phase), control torque is constrained according to Eq. 9.

5.2 Control Strategy

To maintain broadest potential applicability a resistive torque controller operating with only a time-average model and minimal sensor requirements is formulated. A maximum-power-point "Kω^2" non-linear, open-loop controller [60], defined by Eq. 13 and Eq. 14, has been found to perform adequately under Region 2 control [21], [53]. This controller relies only on a measurement of turbine angular velocity and a time-average performance model. Because it does not account for intracycle dynamics, oscillations at turbine blade passage frequency are expected in command torque and angular velocity. For power-tracking control, a non-linear control law is selected to operate in the over-speed region [53]. The control law

$$\tau_c = P_{rated}/\omega \tag{36}$$

prescribes control torque where P_{rated} is the power-tracking set point. To maintain constant power, intracycle variation in angular velocity is accompanied by a complementary adjustment in control torque. In effect, this is a simplistic "model-inverse" controller, with a requirement that the control torque update rate must be substantially faster than the intracycle hydrodynamics.

5.3 Controller Stability

The power-maximizing control law increases control torque with increasing angular velocity. If the turbine is operating at a point where the hydrodynamic torque decreases with deceleration (e.g., the maximum of the C_Q vs. λ), a decrease in the hydrodynamic torque (as a result of turbulence) can cause the turbine to decelerate to zero speed [61]. Contrarily, under power-tracking control, control torque increases with decreasing angular velocity at a given rated power. If the turbine is operating in this mode and the maximum power the turbine can produce drops below rated power (e.g., a turbulent gust reduces inflow speed while the turbine operates at the maximum of the C_P vs. λ curve for a given θ), then the control law will also decelerate the turbine to zero speed. Because $C_Q = C_P/\lambda$, when these control laws are applied to a lift-based cross-flow turbine ($\lambda > 1$), the power-tracking controller can cause the turbine to decelerate to zero speed at a higher λ than the power-maximizing controller [62]. In addition, because $C_P(\lambda, \theta)$ and $C_Q(\lambda)N_Q(\lambda, \theta)$ are negative for some phases), both control laws are steady-state unstable at certain phases of the turbine rotation if control actuation is constrained to resistive torque. However, this does not prevent operation in practice if the turbine has sufficient rotational inertia to reach a steady-state stable phase prior to decelerating below

the critical λ. Critical values of λ are, consequently, well-predicted by the time-average performance model [53],[26].

Given these limitations, it is desirable that the control law maximizes power when

$$P_{available} = P_{fluid} C_P^* < P_{rated} \tag{37}$$

and maintains rated power at other times, where $P_{available}$ is the time-average power available to a turbine rotating at λ^*. Consequently, as the available fluid power decreases, a power-tracking controller must transition to a power-maximizing controller at λ^* and vice-versa. This suggests a combined control law

$$\tau_c = \min(K\omega^2, P_{rated}/\omega). \tag{38}$$

Since $K\omega^2$ specifies control torque such that the turbine is in time-average equilibrium at λ^* [60], any time $P_{rated}/\omega > K\omega^2$, the equilibrium operating condition of the power-tracking controller would cause λ to drop below its critical value of λ^*. This strategy results in a continuous torque command when transitioning between regions and does not require knowledge of $P_{available}$ (i.e., no measurement of inflow is necessary for implementation).

5.4 Methods

5.4.1 Turbine Characterization

Experiments to develop time-average and phase-resolved turbine models and evaluate the proposed control law were carried out in the Alice C. Tyler recirculating water flume at the University of Washington. The flume has a test section 5 m long and 0.75 m wide and was filled to a static depth of 0.5 m. The turbines were supported as shown in Figure 4.1 (right), such that the turbine geometric center-point was aligned with the center of the flume cross-section. At this location, flow velocities up to 1.2 m/s could be obtained with 2% turbulence intensity (TI) as calculated by

$$TI(\%) = 100\sqrt{(\overline{u} - u')^2 + (\overline{v} - v')^2 + (\overline{w} - w')^2}/\overline{u} \tag{39}$$

where u, v, and w are flow velocity (m/s) in the stream-wise, cross-stream, and vertical directions respectively, with an overbar implying the temporal mean and the apostrophe implying an instantaneous variation. The frequency spectra of this turbulence at a mean velocity of 1.15 m/s are shown in Figure 5.1, as measured by a profiling ADV (Nortek Vectrino) sampling at 100 Hz at the turbine location. This indicates the turbulence is approximately isotropic for frequencies greater than 1 Hz, as the flattening of the horizontal and vertical

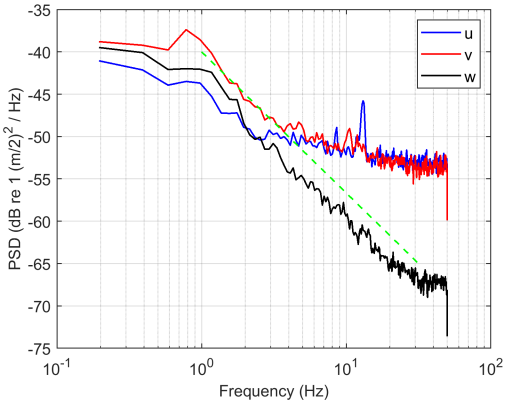

Figure 5.1: Power spectral density of flume turbulence measured at turbine location. The dashed line indicates the $f^{-5/3}$ decay for isotropic turbulence

components are a consequence of the instrument noise floor.

Since the turbine cross-sectional area is 10% of the flume cross-section, performance is likely to be augmented relative to unconfined conditions [8]. However, since both turbines have the same flow confinement, no correction is required to interpret results.

During turbine characterization and controls testing, a Nortek Vector ADV, sampling at 64 Hz at the flume centerline five turbine diameters upstream of turbine center provided inflow velocity estimates. These were despiked using the method of Nikora and Goring [63].

Two types of cross-flow turbines were considered: a helically-bladed turbine with four blades and circular endplates and a straight-bladed turbine with two blades and rounded-rectangular struts connecting the blades to the central shaft. Both turbines have the same blade chord length, diameter, and height. These morphologies were selected to yield different intracycle dynamics. Details of the turbine geometry are given in Table 1.

A servomotor (Yaskawa SGMCS-05B3C41) applied a time-varying, resistive control torque (Eq. 38). An encoder internal to the servomotor with 2^{18} counts/rotation recorded turbine position. A polynomial fit to position was differentiated to provide a smoothly-varying estimate of angular velocity and acceleration. The control torque applied to the turbine was measured by a pair of 6-axis load cells (ATI Mini45 at the top and ATI Nano25 at the base). These sensors were sampled in real-time at 1000 Hz (National Instruments 6353 PCI DAQ) and low-pass filtered to 100 Hz to limit the impact of sensor noise and high-frequency structural vibrations of the test apparatus but retain disturbances due to turbine intracycle dynamics (< 15 Hz), energetic turbulence (< 5 Hz), and controller update rate (100 Hz).

The chord-based Reynolds number

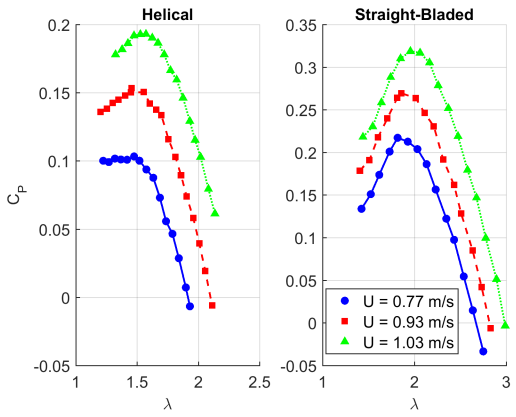

Figure 5.2: Time-average characterization for each turbine at three inflow velocities.

$$Re = Uc/\nu \tag{40}$$

where c is turbine chord length and ν is the kinematic viscosity of water, is $\sim$ 55,000, which is in the laminar-to-turbulent transitional regime. As such, characteristic performance of the turbine is expected to vary with flow speed. Mean inflow velocity was held constant with the turbine rotated at a constant angular velocity for 30 s, a length of time found to yield statistically stationary estimates for power performance. Angular velocity set points were selected to populate the power-producing region of the C_P-λ curve for each turbine. Characterizations were carried out for three different mean inflow velocities (nominally 0.77, 0.93, and 1.03 m/s), that bounded time-varying velocities the turbine would encounter in controller testing. Time-average power performance curves for each turbine at each velocity are presented as Figure 5.2. Using turbine position data and the time-average characterization, N_Q was then determined by phase-averaging measured turbine torque over an angular range of 3.6° and dividing by the time-average torque for each characterized λ. This is visualized in Figure 5.3. Over the power-producing regions of turbine operation with which we are concerned, this is expected to be nearly identical to performance under constant torque control [64].

Based upon each time-average characterization, K was calculated using Eq. 14. To ensure stability during varying inflow, the smallest of these K values were utilized during controls testing. Further, as shown in Table 8, K is small relative to ω (Eq. 3) and therefore small variations in K due to flow speed will not significantly affect control torque (Figure 5.2, Eq. 13).

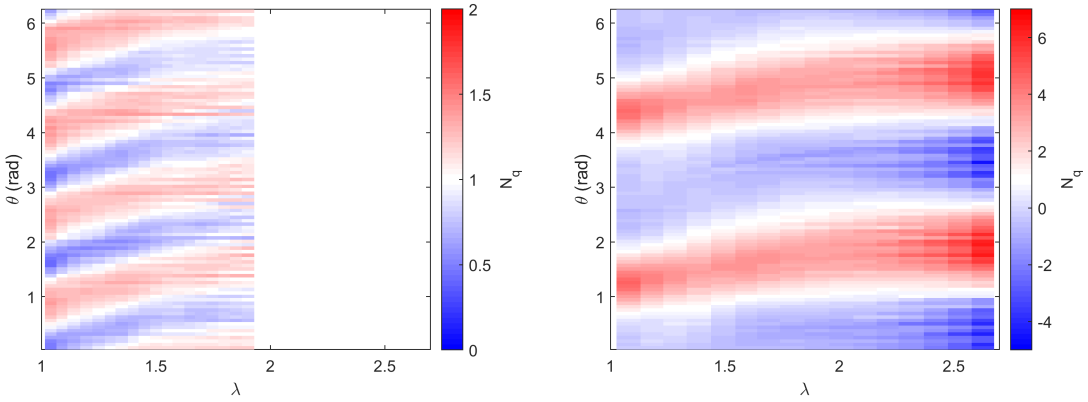

Figure 5.3: Dependence of torque coefficients on phase and tip speed ratio for helically-bladed (left) and straight-bladed turbines (right) under constant-velocity control and constant mean velocity ($U = 0.93$ m/s). Note the difference in the color bar scales.

Table 8: Turbine Geometric and Operating Parameters

Parameter	**Helically-Bladed**	**Straight-Bladed**
Blade Profile	Helical, 90° sweep	Straight
Blade Count	4	2
Blade Shape	NACA 0018	NACA 0018
Chord length (m)	0.04	0.04
J (kg m^2)	0.01	0.0074
A (m^2)	0.0402	0.0402
R (m)	0.086	0.086
C_P^* (at U=1 m/s)	0.19	0.32
λ (at U=1 m/s)	1.57	1.96
Evaluated rated power (W)	[1:1:6]	[2.5:1:8.5]
K (Eq. 14)	6x10^{-4}	5x10^{-4}

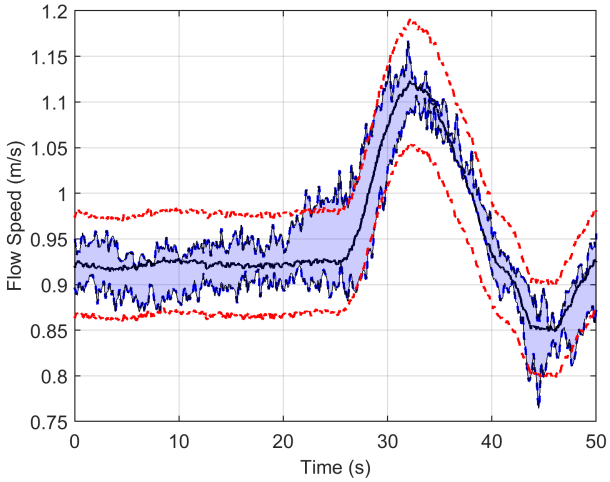

Figure 5.4: A selection of flow time series from control experiments. The median of all time series is shown along with the maximum and minimum bounds of flow speed encountered at a given time in the pump cycle (blue shading), and the $(\pm 3TI)U$ bounds (red dashed lines), estimating the potential expected contribution of turbulence at every point.

5.4.2 Controller Evaluation in Laboratory Experiment

To evaluate the control law, inflow was varied continuously over a 50-s cycle by prescribing the pump drive frequency for the flume. This yielded inflow conditions that, depending on P_{rated}, placed the turbine entirely within Region 2, entirely within Region 3, or transitioned between the regions. Though the pump frequency was precisely regulated, there was limited run-to-run variability in amplitude and phase due to long-period transients in the flume and turbulence, as shown in Figure 5.4.

For each combination of rated power and turbine (Table 8), the experiment was repeated three times. Control torque was updated at 100 Hz based upon an ω measurement sampled by an encoder at 1000 Hz and filtered to 50 Hz. The torque applied by the servomotor can be commanded by a current output from the DAQ to its drive. However, we found that there was not a linear relationship between the current output and torque produced. Consequently, a PI feedback controller was used to ensure that the intended control torque was imposed on the turbine. This 'inner' control loop was manually tuned to minimize overshoot and settling time in the time-domain, and showed good frequency-domain agreement between measured and commanded torques at frequencies of interest (i.e., < 20 Hz) as shown in Figure 5.5.

5.4.3 Controller Evaluation in Simulation

Investigation of the control algorithm in simulation approximates an "ideal" implementation and thus separates performance limitations of the algorithm from limitations of the laboratory implementation. Therefore, the control law (Eq. 38) was also examined in Matlab Simulink ® by integrating the turbine dynamic equa-

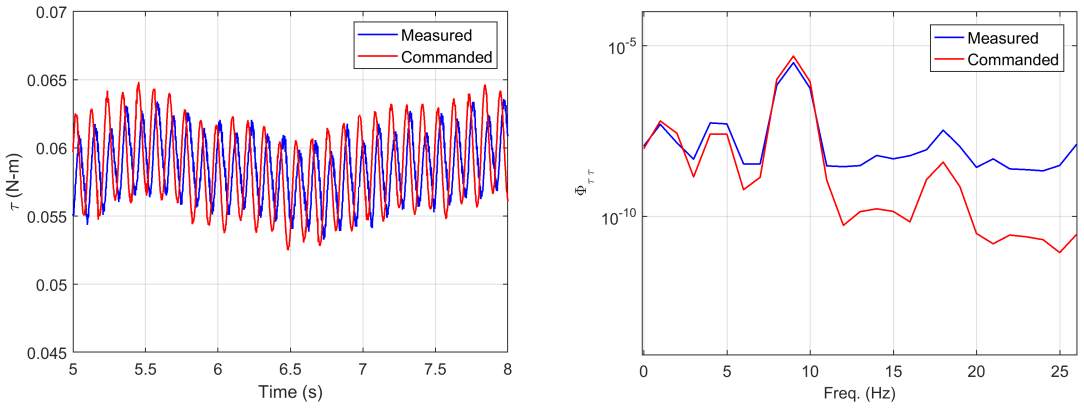

Figure 5.5: 3-second detail view of measured and commanded control torques (left), spectra from an inner loop tuning test (right) under power-maximizing control in approximately constant inflow.

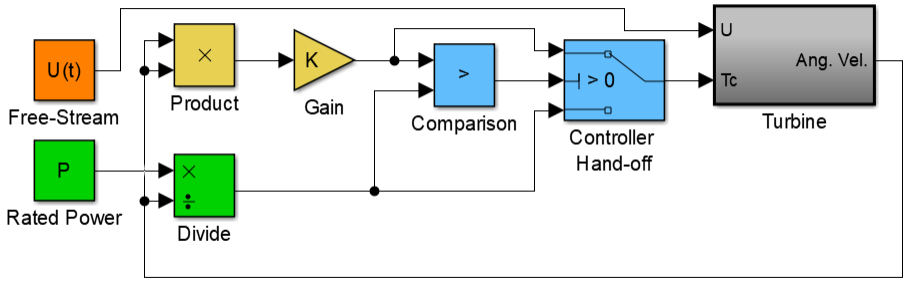

Figure 5.6: Simplified schematic of turbine simulation.

tion (Eq. 1) in the time domain with a 0.001 s fixed time step. In simulation, the hydrodynamic torque was specified from a phase-resolved model of turbine performance (Figures 5.2 and 5.3). We note that hydrodynamic torque is influenced by phase variations in ω imposed by the control law [19] (as opposed to the constant ω characterization), but this simplification is a suitable first-order approximation [64]. An experimentally-measured time series of inflow velocity was used to drive the simulation and allow a comparison of idealized control law performance in simulation and experimental results. In simulation, the inflow was assumed to be spatially uniform across the rotor. Because the experimentally-measured inflow was a point measurement from an acoustic Doppler velocimeter (ADV), the time series was low-pass filtered at 4 Hz with a zero-phase digital filter, a cut-off frequency corresponding roughly to the turbine's maximum dimension using Taylor's Hypothesis [32]. This has been previously shown to improve the accuracy of simulated turbine excitation by turbulence [53]. A representation of the simulation logic is shown in Figure 5.6.

5.4.4 Controller Performance Metrics

The performance of the power-tracking controller was evaluated by the mean absolute percent error between generated and rated power (Eq. 8) for periods of operation in Region 3 (constant power objective):

$$\epsilon_p = \frac{100\%}{N} \sum \left| \frac{(P - P_{rated})}{P_{rated}} \right| \tag{41}$$

To consistently distinguish between Region 2 and 3 operation, P_{rated}/ω and $K\omega^2$ were calculated, with ω filtered to 2 Hz by a zero-phase digital filter to filter intracycle variations. Region 3 performance was then defined as all times for which $P_{rated}/\omega < K\omega^2$. Finally, to eliminate high frequency noise present in experimental torque measurements, while preserving frequencies of interest, Region 3 power data were low-pass filtered to 20 Hz by a zero-phase digital filter.

Controller effectiveness was also evaluated qualitatively in terms of smoothness, continuity, and the presence or absence of transience upon transition between control objectives.

A comparable analysis of the performance of power-maximizing Kω^2 algorithms is given for helical turbines in [53].

5.5 Results

An example time series demonstrating power-maximizing, transition, and power-tracking operations in experiment for both turbines is shown in Figure 5.7. An example time series of solely power-maximizing operation for each turbine in experiment is shown in Figure 5.8.

At a macro level, it appears that the control objectives are roughly achieved, with turbine power generally tracking available power in Region 2 and tracking rated power in Region 3. Overall, the transition behavior appears satisfactory as there are no large power transients and close power-tracking is achieved. However, in both transitioning (Figure 5.7) and strictly power-tracking (Figure 5.8) operations, accelerating flow yields $P > P_{rated}$, and decelerating flow (Figure 5.4) yields $P < P_{rated}$ for each turbine. This behavior is present when no controller transition has occurred and suggests is it the result of changing inflow velocity, as opposed to an effect of the controller objective transition. As anticipated from the relatively small phase variation in hydrodynamic torque (Figure 5.3), the helical turbine produces significantly smaller intracycle power variations than the two-bladed turbine. For the straight-bladed turbine, intracycle variations appear to be reduced during power-tracking operations (entirety of Figure 5.8 and the indicated Figure 5.7). The transition behavior and power-tracking performance are examined in more detail in subsequent sections.

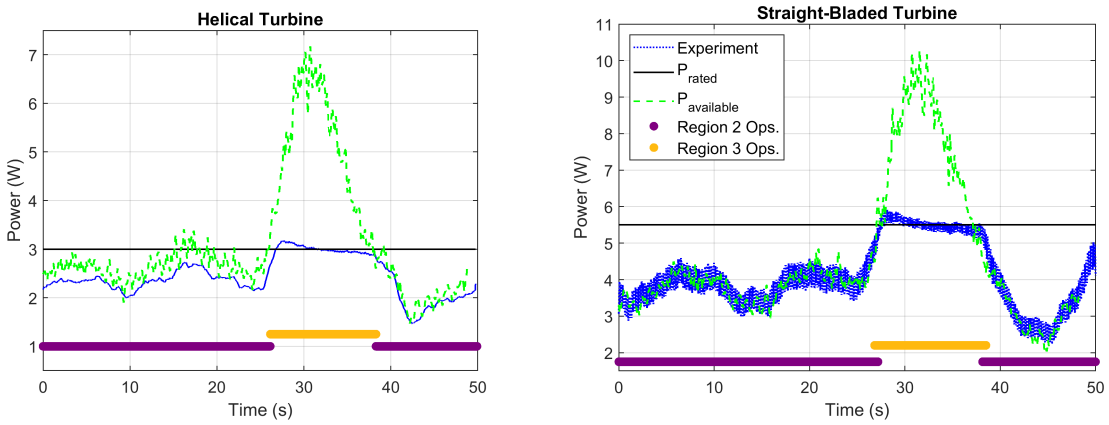

Figure 5.7: Time series of the helical turbine (left) and the straight-bladed turbine (right) under an intermediate rated power set point such that the controller objective transitions. Times for which the controller is in Region 2 operation is indicated by the purple dots, and Region 3 operations are indicated by gold dots. Note that the overlap between the beginning and ending of Region 2 and Region 3 operations indicate numerous rapid transitions due to turbine intracycle variations in control torque command.

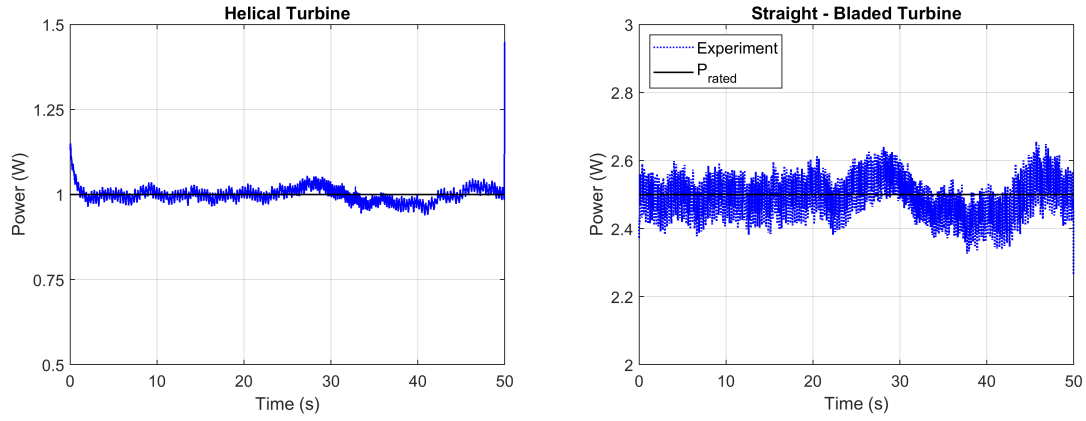

Figure 5.8: Time series of the helical turbine (left) and the straight-bladed turbine (right) under the lowest rated power set point such that $P_{rated} < P_{available}$ for the test duration and the controller objective thus does not transition away from the power-tracking objective.

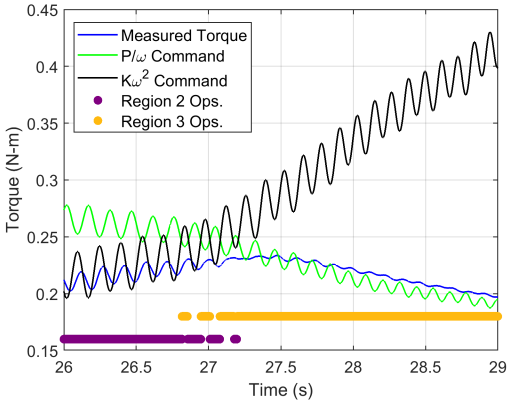

Figure 5.9: A detail view of $K\omega^2$, P/ω, and measured control torques during objective transition. Periods of Region 2 operations are indicated by purple dots, and Region 3 operations are indicated by gold dots.

5.5.1 Transition Behavior

As detailed in Figure 5.9, controller objective transition is achieved in experiment without large torque transients, discontinuities, or sharp changes in torque gradient. However, the measured command torque does not perfectly track either $K\omega^2$ or P/ω torque commands, an indication of the limitations of the laboratory-implemented PI feedback loop on command torque.

To analyze the power overshoot that occurs during flow acceleration, a detail view of Figure 5.7 highlighting the transition to power-tracking control is presented in Figure 5.10, alongside analogous simulation results. The presented results have been filtered to 2 Hz to remove intracycle effects and focus on the low-frequency overshoot behavior.

The overshoot error is significantly smaller in simulation, and is only visible if examined closely (Figure 5.10, right). This indicates that $P > P_{rated}$ during accelerating inflow (and the opposite in decelerating inflow) occurs even in ideal simulated conditions, but is exacerbated by limitations of the laboratory implementation. At each time step, the prescribed torque is based upon the ω measurement at the previous time step, but the turbine is being accelerated by the current inflow. For accelerating inflow in over-speed power-tracking control, this implies $\omega_n > \omega_{n-1}$, and thus $\tau_{c,n} < \tau_{c,n-1}$, where n represents a discrete time-step index (Eq. 36). Thus the delay in controller update results in an instantaneous control torque that is too large to achieve P_{rated} for the current (i.e., time-step n), angular velocity causing the overshoot behavior. In decelerating flow, the inverse argument explains why $P < P_{rated}$. In simulation, this 0.001 s delay is small, such that $\omega_n \sim \omega_{n-1}$. However, in experiment, the ω measurement is filtered to 50 Hz. Further, there is a time-constant associated with the inner PI feedback loop that further delays application of the commanded control torque (also observable in the imperfect command tracking seen in Figures 5.5

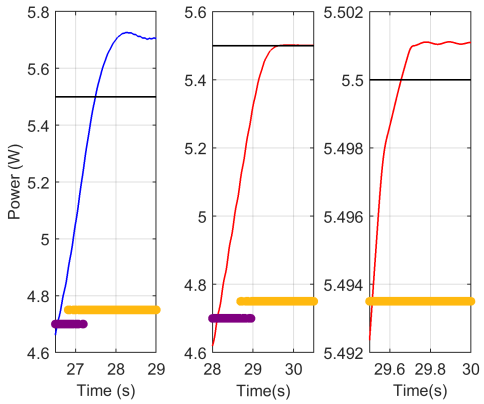

Figure 5.10: A detail view of the controller transition to power-tracking control for the straight-bladed turbine in experiment (left), simulation (middle) and a detail view of simulation (right). Because advection time between flow velocity sampling location and the turbine was not modeled in simulation, the transition occurs at a time stamp that is distinct from experiment. Region 2 and 3 operations are indicated with the purple and gold bars, respectively, as in previous figures.

and 5.9). These additional delays explain the larger magnitude of the error observed in experiment during accelerating and decelerating inflow.

5.5.2 Power-Tracking Performance

As noted in preceding sections, errors in power-tracking are the result of steady-state error during flow accelerations related to controller update rate and imperfect mitigation of intracycle power fluctuations.

The power spectra of power for power-maximizing and power-tracking objectives in experiment are compared against power-tracking objectives in simulation for each turbine in Figure 5.11. Note that because the turbine velocity is changing over the evaluated time series, the indicated turbine rate of rotation and rate of blade passage represent an average over the power-tracking test duration. Power-maximizing $K\omega^2$ control is derived from a time-average model of the turbine: it does not attempt to compensate for intracyle fluctuations in power. As such the highest P_{rated} (for which $P < P_{rated}$ and the control objective is power maximization over the test duration) set point is also plotted for comparison. Because the power-tracking controller is over-speed, the indicated average turbine rate of rotation and average blade passage frequency are lower for power-maximizing operations, so the spectral peaks corresponding to these effects are to the left of the labeled vertical lines for the power-maximizing trace.

For the straight-bladed turbine under power-tracking control, variations at the average turbine rotation frequency (4 Hz) and the average blade passage frequency (8 Hz) are the primary contributors to the power-tracking error. The power-tracking control law cannot entirely eliminate intracycle variation for the straight-bladed turbine, as indicated by the presence of spectral peaks at turbine rotation rate and the

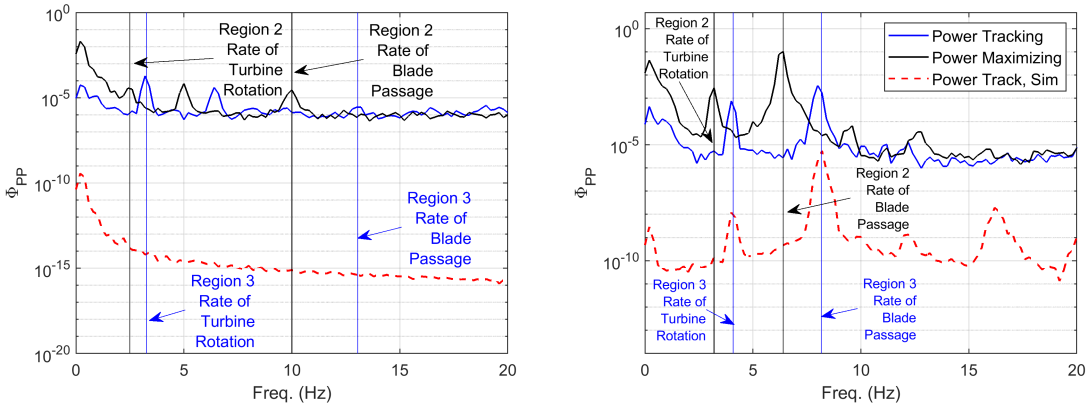

Figure 5.11: The power spectra of power for the helical turbine (left) and the straight-bladed turbine (right) in power-maximizing and power-tracking operation in experiment and power-tracking operation in simulation.

rate of blade passage in simulation data, but the magnitude of these peaks is reduced by several orders of magnitude compared to experiment. The helical turbine data shows more variation once and twice per cycle than at the rate of blade passage, though both are an order of magnitude smaller than the intracycle excitations of the straight-bladed turbine. This may indicate that mechanical imbalance in the helical turbine (e.g., imperfections in one blade) excites more variance in power at the rotational frequency than the blade passage frequency. These spectral peaks are not present in simulation for the helical turbine, indicating that idealized power-tracking control can remove any significant intracycle fluctuation for this turbine. The two-bladed turbine also shows variation once-per-rotation, implying that the component of the variance at the rate of blade passage is a combination of the rate-of-rotation harmonic and the blade passage effect. The lower frequency variations (< 2 Hz) are caused by turbulent excitation and the steady-state errors during inflow accelerations.

Comparing to the power spectra for power-maximizing control in experiment against power-tracking spectra shows reduction in intracycle power fluctuations, as expected. For the straight-bladed turbine, fluctuations at blade passage frequency were reduced by two orders of magnitude, and nearly an order of magnitude at turbine rotation rate. For the helical turbine, a smaller reduction was achieved, indicating that the laboratory implementation did not reduce these smaller intracycle fluctuations significantly during power-tracking operations for this turbine.

The contribution of the intracycle fluctuations to the total ϵ_p is estimated by low-pass filtering the power data to 2 Hz by a zero-phase digital filter prior to calculating the mean absolute percentage error (Eq. 41), retaining (approximately) only errors related to the delayed controller response during accelerating inflow. The difference of the total and filtered error then approximates the error contribution due to unmitigated

Table 9: ϵ_p for power-tracking control of the helical turbine in simulation and experiment

Set point (W)	Experiment ϵ_P			Simulation ϵ_P		
	Total	Flow Acceleration Overshoot	Unmitigated Intracycle Variation	Total	Flow Acceleration Overshoot	Unmitigated Intracycle Variation
1.0	1.53	1.24	0.29	2.8e-3	2.8e-3	2.5e-5
2.0	1.36	1.29	7.0e-2	1.4e-2	2.9e-2	-1.6e-2
3.0	2.19	2.18	1.0e-2	1.1e-2	5.4e-2	-4.3e-2
4.0	1.57	1.59	-2.3e-2	1.2e-2	8.6e-2	-7.4e-2
5.0	0.74	0.79	-4.4e-2	2.0e-2	0.21	-0.18

Table 10: ϵ_p for power-tracking control of the straight-bladed turbine in simulation and experiment

Set point (W)	Experiment ϵ_P			Simulation ϵ_P		
	Total	Flow Acceleration Overshoot	Unmitigated Intracycle Variation	Total	Flow Acceleration Overshoot	Unmitigated Intracycle Variation
2.5	1.87	1.14	0.73	4.2e-2	2.7e-3	3.9e-2
3.5	2.07	1.16	0.91	7.0e-2	2.4e-2	4.6e-2
4.5	2.47	2.27	0.20	0.24	0.22	1.9e-2
5.5	2.56	2.21	0.35	0.21	0.23	-1.7e-2
6.5	1.61	1.00	0.61	0.55	0.53	2.4e-2
7.5	1.81	0.90	0.91	0.60	0.60	1.0e-2

intracycle variations. Formally,

$$\epsilon_{p,intracycle} = \epsilon_{p,total} - \epsilon_{p,overshoot} \tag{42}$$

where $\epsilon_{p,total}$ is the total mean absolute percentage error, $\epsilon_{p,overshoot}$ is the error calculated from 2 Hz filtered data, and $\epsilon_{p,intracycle}$ is the remaining error, an estimate of error contribution due to unmitigated intracycle variation. These values are presented for simulation and experiment for the helical turbine in Table 9 and for the straight-bladed turbine in Table 10.

In relative terms, the mean power tracking errors are quite limited, less than 3% for all set points tested. Particularly for the helical turbine, the error associated with the overshoot is a substantial portion of the total error, indicating that unmitigated intracycle fluctuations are a comparatively small contribution to the total error. As expected due to the larger intracycle variation in power, errors for the straight-bladed turbine have a larger component resulting from intracycle fluctuations, but error associated with an overshoot remains a substantial portion of total error. In simulation, where the response to intracycle fluctuations is nearly ideal, nearly all of the error can be attributed to overshoot. In fact, for the helical turbine, filtering to remove the effect of intracycle fluctuations actually increases the mean absolute percentage power-tracking error, since filtering effectively lengthens the periods of controller overshoot. This, in turn, results in a negative error

estimate for the contribution of unmitigated intracycle fluctuations.

The largest total power tracking error in experiment occurs at an intermediate set point for both turbines. This is the influence of overshoot error. For the lowest power set points, both turbines operated in Region 3 for the test duration. For the next-lowest power set points, both turbines are operating in Region 2 operations only near the flow speed minimum, roughly at times 40 to 45 s. At the points of maximum error (Figure 5.7), both turbines operate in Region 3 primarily during large flow accelerations. Finally, at the highest power set points for which Region 3 operations occurred, they only occur near the maximum inflow velocity, where (by definition) inflow velocity gradients are small. Therefore, the lowest and highest power set points only experience large inflow accelerations for small portions of their Region 3 operation and have correspondingly small overshoot error, while intermediate set points operate in Region 3 principally during large flow acceleration and experience the largest power tracking errors due to more significant overshoot.

5.6 Discussion

5.6.1 Achievement of Control Objectives

Overall, mean absolute percent power-tracking error for the laboratory implementation is consistently less than 3% for a significant flow acceleration. Though the controller response is imperfect, excellent power-tracking performance is achieved for both turbines. The observed transition behavior does not result in detrimental transients in power or torque (Figures 5.10 and 5.9). Further, the observed power-tracking overshoot appears to occur due to flow accelerations and not controller transitions, since it is also present in strictly power-tracking operations (Figure 5.8). Close inspection of Figure 5.9 demonstrates that the control law objective transitioned multiple times due to intracycle fluctuations. Because stability and smoothness was maintained across multiple objective transitions at blade-passage frequency with no relatively large values of torque or power-tracking error, there appears to be no need for a transitional "Region 2.5" controller.

5.6.2 Potential Improvements

The comparison of laboratory to simulation results suggests that the laboratory implementation was not ideal as a consequence partially of the inner feedback loop on commanded torque in experiment, which provides generally effective, but imperfect, tracking (Figure 5.5). More aggressive gains with a faster response were attempted. However, digital noise in the measured torque (electromagnetic interference from the servomotor) required more aggressive filtering to maintain stability, thereby decreasing responsiveness to frequencies of concern. Because the control torque was not exactly as commanded, intracycle oscillations in experiments were not mitigated to the extent predicted by simulation, as indicated by the intracycle power-tracking error

in Tables 9 and 10. Further, this necessary filtering effectively slowed the controller update rate, limiting the extent of intracycle fluctuation mitigation and resulting in the steady-state errors during flow accelerations. Necessary filtering (50 Hz) on the angular velocity signal used for control calculations also contributed to these errors.

If lower noise measurements were available, it may have been possible to tune the inner loop more aggressively or sample angular velocity and torque more quickly to improve this response and increase the effective update rate of the command torque. This would reduce the errors due to both intracycle fluctuations and the steady-state error during flow accelerations. This highlights the importance of adequate sensor and actuator selection to maximize the efficacy of a turbine control law. However, resistive torque control is fundamentally limited in that it relies on inflow to accelerate the turbine. As such, below a certain inflow, the necessary accelerations to achieve an intracycle control trajectory that wholly mitigates intracycle fluctuations may not be achievable for turbines for which those fluctuations are significant. This is evidenced by the performance of the simulated power-tracking operation of the straight-bladed turbine: even under ideal conditions, power fluctuations remain at turbine rotation and blade passage frequencies (Figure 5.11). The limitations of a resistive torque controller are explored analytically for an example control trajectory in Appendix C.

5.6.3 Extensions to Field Implementation

The performance of the control law in varying turbulent inflow in laboratory experiments suggests it may be viable for field implementation. In this evaluation, the prescribed time-variation in inflow produced a transition between control objectives. In a real environment, there will likely be many objective transitions at different time scales. In the present study, a turbine encountered several objective transitions as the instantaneous power output varied above and below the set point power due to intracycle variation. While there was some overshoot and imperfect power-tracking, there did not appear to be any instability or large variation in control torque during oscillatory transition at time-scales less than 1 s. Consequently, the flume evaluation can be considered representative of control objective transition behavior if the time-scales associated with intracycle variations are faster than those associated with changing inflow. Considering that the length scale of such high-frequency turbulence is unlikely to affect turbine dynamics, this should be generally true and, as such, these results are likely applicable to a turbine operating in realistic turbulence.

Larger turbines with higher inertia are only sensitive to larger turbulent length scales (i.e., lower frequencies via Taylor's Hypothesis) [18] [40] [32]. Larger inertia turbines will accelerate more slowly for a given flow acceleration (Eq. 1), which will reduce the steady-state power-tracking error during a flow acceleration for a given update rate. However, such a turbine will also be less responsive to turbulent gusts and therefore

will not operate as efficiently in power-maximizing operations. For a given λ, a turbine with a larger radius will also rotate more slowly, implying lower-frequency intracycle variations. Conceivably, there may exist particular scales and turbines for which the intracycle excitation bandwidth and the turbulent bandwidth overlap. The present study only examined controller performance with distinct excitation frequency bands. While there is not a theoretical reason the controller would not continue to be effective for overlapping excitation bandwidth, this has not been explicitly examined and is a potential area for future study.

Practically, if the controller update rate is limited by the specifics of the implementation in hardware or the control law is applied to a turbine that has λ^* approaching 1, it may be desirable to make the transition between regions at a slightly larger value λ' (e.g., $\lambda' = 1.1\lambda^*$). This would provide an additional margin of stability during objective transition at moderate cost to power generation. To ensure a continuous torque command, K' (for which the turbine is in equilibrium at λ') can be utilized in lieu of K during transition to the power-maximizing control objective [29].

In field implementations, measurements of torque and rotation rate may not be available. However, assuming that the control torque update rate is sufficiently fast [53], the control law can be approximated using only a power measurement as

$$\tau_{c,n} = \min(K(P_n/\tau_{c,n-1})^2, P_{rated}/(P_n/\tau_{c,n-1})) \tag{43}$$

where P_n is the measured power at time step n. This presumes the input mechanical power to the generator can be measured; if only output electrical power measurements are available, the dynamics of the generator must also be considered, though these are typically at least an order of magnitude faster than the hydrodynamics. However, using lagged measurements to approximate ω will decrease the effective controller update rate, and, as shown here, increase power-tracking error by limiting the mitigation of intracycle fluctuations and the steady-state error during changing inflow.

The limited intracycle variations observed for the helical turbine allowed for reduced power-tracking error overall and smaller fluctuations than the straight-bladed turbine. However, the helical turbine has lower time-average efficiency than the straight-bladed turbine (Figure 5.2). Because deployment sensors and power electronics must be selected based in part on the potential peak power/torque/speed the device will experience, this suggests potential trade-off between larger power-tracking error (and potentially larger peak loads) and lower time-average power output that may drive turbine system selection. Grid-scale deployments are likely to consist of an array of several turbines. In this instance (particularly if approximately uniform inflow can be presumed), several straight-bladed turbines could be deployed at various azimuthal angles such that the overall array power output could be smoothed while also utilizing a more efficient turbine

morphology.

5.6.4 Limitations of Control Method

Under this control strategy, torque actuation will occur at the frequencies at which angular velocities are perturbed. If a control design objective requires reducing command torque perturbations (e.g., to minimize drive-train fatigue or other loads), the measurement can be cascaded with a low-pass filter. However, care must be taken to not introduce a phase-shift to the measurement that leads to instability at the frequencies of intracycle variation, as these frequencies will be regularly excited. As such, a filter cut-off frequency must either be well-above this frequency (as utilized in this study) or far enough below it that the magnitude of any controller response to intracycle excitation will be greatly attenuated. This latter approach is akin to treating the turbine in a time-average sense, as it will not attempt to compensate for disturbances at blade passage frequency, which will increase intracycle power-tracking error particularly for low-solidity, straight-bladed turbines.

Though simple to implement, purely resistive torque control may be overly restrictive for modern power electronics. External or stored power may be available to periodically accelerate a turbine using the generator as a motor. Consequently, the present study represents a worst-case scenario for power-tracking control of a cross-flow turbine and demonstrates the extent to which control objectives can still be achieved with this limitation.

5.7 Conclusions

The proposed controller successfully tracks power and transitions between power-maximizing and power-tracking objectives in unsteady flow. The controller requires only a measurement of angular velocity and a time-average turbine model (a measurement of control torque is needed only if torque feedback control is necessary). Even though the control law only allowed a resistive torque to be applied to the turbine, it accurately tracked a variety of set points in time-varying inflow for both helical and straight-bladed turbines. Further, the algorithm transitioned smoothly and repeatedly between power-maximizing and power-tracking objectives based on available flow power, such that a transitional controller is unnecessary. The power-tracking controller mitigated intracycle variations as compared to the power-maximizing controller, but did not eliminate them. Helical turbines (generally lower efficiency, but with smaller intracycle fluctuations) will be able to hold a more stable power output than straight-bladed turbines, albeit with a lower time-average power output. In simulation, an idealized implementation of the controller mitigated all significant intracycle variation for the helical turbine. This suggests a trade-off that may affect power electronic and

sensor selection. In an array, particularly if a spatially uniform flow field can be presumed, operating several straight-bladed turbines may smooth the array power output without sacrificing hydrodynamic efficiency. The extent to which mitigation of intracycle variations is possible in a physical implementation depends on the speed and accuracy with which the commanded torque value can be realized, which is a function of sensor noise, controller update rate, and any feedback control tuning.

The controller examined herein was purposely selected for ease of implementation on a physical system. The relationship between power-smoothing at the turbine (as in this study), power smoothing achievable at the power electronics, and the associated availability of external power to periodically drive the turbine rotor, should be investigated. Further, power-maximization and power-tracking are likely to not be the only control objectives utilized on a field-scale device. Performance of the investigated control law should be considered in the context of turbine structural loads and actuation cost.

6 Conclusions

The presented investigation progresses from the development of a time-average characterization appropriate for realistic non-uniform inflows to an evaluation of controller development methodologies in the context of power-maximizing controllers, and culminates with the presentation of an effective and simple control law capable of power-maximization and power-tracking appropriate for cross-flow turbines. The extent to which simulation and small-scale laboratory testing is predictive of field-scale controller performance is considered with the intention that the presented methodologies, if not the results, are device-agnostic and can facilitate controller development for a prospective field-scale turbine. The ultimate objective of this investigation is to demonstrate the extent to which control under the limited implementation utilized herein is attainable, such that the cost-benefits of deploying more capable systems have a performance reference, and the design trade-offs relating to turbine morphology are better understood.

6.1 Performance Characterization in Non-Uniform Inflow (Section 3)

A characterization procedure is presented that is appropriate for a turbine deployed in spatially-varying inflows that are robust in time. The method relies on a series of temporally-and-spatially distinct measurements of inflow velocity and turbine power performance measurements taken over the same time period (though not necessarily with exactly-overlapping sampling times). Assuming that the spatial variation of the inflow is approximately constant, a spatial velocity profile can be estimated from a set of distinct sampling locations taken at different times. The effective inflow velocity observed by the turbine rotor can then estimated by averaging the spatial inflow velocity profile over the turbine rotor area. Finally, time-average performance curves (η and/or C_P vs. λ) can be constructed using time-averaging turbine power performance data and the constant estimate of effective inflow velocity. Because sets of turbine power performance data taken at different times yield nearly identical performance curves when a constant effective inflow velocity is assumed, this suggests that the spatial-temporal averaging method is valid for this inflow, and the characterization method is applicable to turbines operating in similarly synoptic inflow. The implications of non-uniform inflow for turbine control strategies is explored in simulation. From a time-average characterization, the critical control parameters needed for implementation of the controllers proposed in Section 5 can be calculated.

The key assumption of this work, that the spatial variation in inflow is robust in time, was observed directly the following year by the sensor array detailed in Appendix B, when the turbine was deployed in roughly the same location with alternate instrumentation.

The difficulties persistently non-uniform inflows present for time-average turbine characterization suggest that controllers relying on real-time estimates of inflow velocity will be challenging to implement. Unless a

significant increase in turbine performance under these control strategies can be demonstrated, the added expense and complexity of upstream sensing is unlikely to be justifiable.

6.2 Evaluation of Controllers in Simulation, Laboratory Experiment, and at Field-Scale (Section 4)

Three potential Region 2 torque controllers were evaluated in computer simulation, laboratory experiment, and field-scale testing. Time-average turbine performance characterizations were performed for each turbine. Simulation of proposed controllers was found to be predictive of laboratory and field-scale controller performance with two limitations. Firstly, limitations of the physical control implementation, such as sensor noise, were not captured in simulation. Secondly, a simple low-pass filter was used in laboratory testing to restrict measured inflow to engulfing length scales to which the turbine would be responsive, a presumption of isotropic turbulence that is likely unrealistic. In addition, subsequent investigation using phase-resolved turbine models suggests that a portion of the under-prediction of variation of turbine dynamics is the result of intracycle disturbances not modeled by a time-average representation, but this discrepancy may be small in this case because both studied turbines were helically-bladed.

One of the evaluated controllers required a measurement of upstream inflow. This controller did not demonstrate significant increases in turbine performance in simulation or laboratory testing, and was not successfully implemented in the field. Further, effective gains for feedback control laws in physical implementations were difficult to predict using simulation alone. Including electromechanical emulation in the controller development process can address this shortcoming. This suggests simulation and small-scale experiment will be most predictive of controller performance when the controller does not rely on feedback gain tuning or upstream flow measurement. For Region 2 control, $K\omega^2$ control meets both of these criteria and consistently demonstrated the best performance among the evaluated algorithms.

6.3 Power-tracking Control and Control Objective Transition (Section 5)

An open-loop model-inverse Region 3 controller was selected to complement $K\omega^2$ for Region 2 control, and was examined in time-varying inflow for two cross-flow turbines in simulation and experiment. The combined Region 2 and Region 3 control law requires only a time-average turbine characterization, a measurement of angular velocity, and the application of resistive control torques. To ensure simulation results are accurate for the straight-bladed turbine, which exhibits significant intracycle variation, a phase-resolved model of the turbines was used in simulation to estimate control algorithm behavior in an ideal implementation. The algorithm demonstrates effective power-tracking and smooth and stable transitions between controls objec-

tives for both turbines. Errors in power-tracking are due to unmitigated intracycle variations and delayed control response to flow accelerations. Errors are significantly lower in the simulated ideal implementation, but intracycle variations are not completely mitigated, indicating a theoretical performance limit for resistive torque control algorithms. The latter is explored analytically in Appendix C, and the impact of this limitation is found to decrease with increasing turbine radius, suggesting field-scale device performance may be less limited by an implementation capable of only resistive torques. A low-solidity straight-bladed turbine showed more significant unmitigated intracycle variations in both experiment and simulation than a higher-solidity helically-bladed turbine, but had a higher time-average efficiency than the helical turbine, suggesting performance trade-offs. The extent to which power smoothing is necessary at the turbine will depend on the selection of power electronics, but the efficacy of the explored control algorithm suggests relatively high performance is attainable with a simplistic implementation.

6.4 Future Work

6.4.1 Cross-flow Response to Anisotropic Turbulence and Sheared Inflow

Point measurements of velocity via acoustical instruments were used throughout this investigation and are also common in field deployments. When these measurements were applied to simulation, a low-pass filter was applied with the intention that retained turbulence would be an engulfing gust relative to the long axis of the cross-flow turbine, and would act over the entire rotor area. However, applying Taylor's Hypothesis (Eqn. 11) only implies a length scale in the direction of mean inflow, while the long axis of a cross-flow turbine will be perpendicular to this. Thus, this approach to filtering, as noted in Section 4, is akin to assuming isotropic turbulence, which is a poor assumption at these large length scales.

In a laboratory, anisotropic turbulence can be generated intentionally and studied via Particle Image Velocimetry (PIV). Examining the turbine response to turbulence of different orientations and length scales would better inform characterizations of turbine deployment sites and turbine dynamic simulations. This represents an aquatic analog to axial-flow wind turbine characterizations based on spatially-resolved LIDAR-measured flow fields that underpin preview control and model-predictive control laws [39], albeit with the key distinction that PIV investigation is largely confined to laboratory-scale devices. While this implies that laboratory results would need to be extrapolated to field-scale, characterizations of turbulence anisotropy at prospective marine hydrokinetic sites have been undertaken [46] [30], and the impact of this observed turbulence on turbine response could likely be at least qualitatively predicted.

Investigating turbine response to sheared inflow would be similarly useful. While a method to generate a robust characterization from point-measured flow velocities for a turbine in persistently sheared inflow was

developed in Section 3, time-average turbine performance was not directly explored as a function of inflow profile. In a laboratory flume, sheared inflow of multiple orientations and gradients could be generated and turbine performance characterized for each for comparison to a uniform-inflow characterization. At present, the characterization standard developed from work presented in Section 3 addresses potentially sheared inflow by prescribing the number and distribution of upstream flow-measurement devices based upon the turbine cross-section when the inflow has been determined to be non-uniform across the turbine face. Given the difficulty of securing a site for a field-scale device characterization, alternative testing locations may not be available. A means to relate sheared-inflow performance to uniform-inflow performance (or alternative sheared-inflows) would help ensure field-scale device characterizations can be extrapolated to other sites and inflow conditions, and could potentially reduce the number of sensors required to perform a characterization in sheared inflow.

Scaling associated with these studies will be more difficult than the controls work. While scaling controller performance results depended upon turbine output performance metrics and basic assumptions about the power spectra of turbulence, (i.e., the hydrodynamic interactions were treated more as a "black-box" disturbance), study of the turbine response to anisotropic turbulence and sheared inflow must directly address the specific hydrodynamic interactions of the inflow on the blades. Laboratory investigations (in which the desired inflow characteristics can be more easily created) will need to be carefully scaled to be predictive of field-scale response in analogous inflow. If possible, this sort of investigation should be performed at multiple device scales and Reynolds numbers.

Utility-scale hydrokinetic turbine installations are likely to consist of several devices deployed as an array. Depending on the shape, downstream turbines of the array may see persistent flow perturbation from upstream turbines. This potential complication of array deployments also encourages future study of turbine response to sheared inflows and anisotropic turbulence.

6.4.2 Consideration of Power Electronics

Power-smoothing attainable at the turbine rotor itself has been considered, but a field-scale implementation will incorporate power electronics to connect the turbine generator electrical output to the grid. Ultimately, a torque control algorithm will be implemented on the power electronics such that manipulation of the generator coil current will impart the prescribed torque. The selection of specific power electronics will depend on the size, current, and speed of the generator as well as the demands of the selected torque controller. As such, the relationship between torque controller selection and power electronic selection must be considered during field-scale system design. Power-maximizing and power-tracking controllers suggested in this work have consistently presumed that no reactive power is available to motor the turbine, with the

intent to minimize implementation complexity and ensure the controllers are broadly applicable. However, control objectives can be more tightly obtained in a broader range of flow speeds if some reactive power is available. Finally, overall system efficiency will depend strongly on electrical component selection.

Overall, an economic analysis on a system-by-system (or array-by-array, as appropriate) basis considering both controller performance and requisite component cost will dictate controller/power electronic selections. As such, the proposed control law needing only purely resistive control torque may not be the best choice for all implementations. A more complete controller development procedure would incorporate electrical hardware-in-the-loop emulation of any proposed turbine control law to predict field-scale device electrical performance, rather than solely hydrodynamic performance. An example of this sort of investigation can be found in [26].

As mentioned previously, arrays of hydrokinetic turbines may have differing control objectives than those developed in this work on a single device, and this extends to the selection and implementation of appropriate power electronics. For example, if multiple devices are coupled together and the aggregate power is input to the power electronics, ensuring individual turbines are out of phase with one another could decrease the peak-to-average power ratio, reducing the need to smooth power via control of an individual turbine and allowing for more limited smoothing capability at the power electronics.

In summary, selection of a controller and power-electronic implementation should be made conjunctively. The development of multiple generalizable turbine controller forms appropriate for a variety of implementations would also be useful.

6.4.3 Definition of Optimal Trajectories

The combined capabilities and limitations of power electronics can be incorporated into an implementation-specific cost function to advise controller development. As noted, phase-resolved turbine models are difficult to develop and have potentially high uncertainties. However, if a model is available, the controls problem can be framed as a nonlinear optimization problem for a given cost function to prescribe an optimal controls trajectory. Actuation limitations (e.g., purely resistive torque) based upon device mechanical limitations or power electronic selection can be incorporated as constraints in the problem statement. Additionally, because the optimization need only occur over a single turbine rotation, the trajectory must also be periodic. Finally, and perhaps most prohibitively, turbine response varies with λ, implying that the optimization must be carried out for multiple flow speeds for power-tracking objectives.

The output of the optimization for a single inflow velocity will be a periodic $\lambda(\theta)$ profile and the appropriately constrained control torque to achieve that profile. As mentioned throughout, the computational difficulty solving this problem is not likely to be justified by the performance of the specific algorithm on an

actual physical device, but it could suggest generalizable control forms under implementation-specific sets of constraints. As mentioned, a key hurdle for cross-flow turbines are the limited examples in literature and industry that have demonstrated effective control. Computer simulations for a number of reasonable hypothetical implementations could provide some guidance to developers. For example, recent work by Ennis et. al., proposed a hysteresis-style control law for an offshore vertical axis wind turbine [6]. And, as previously discussed, Strom et al. has demonstrated the efficacy of smooth periodic angular velocity variation to increase power capture [19]. A selection pool of controllers with distinct features and requirements would facilitate device-specific controller development by providing a general control law architecture as a starting point.

Though shown to be a function of particular morphology, cross-flow turbine intracycle excitations have two over-arching commonalities: the N_Q surface will be periodic (though the period will depend on the blade number) and intracycle fluctuations will likely occur at faster time scales than energetic turbulence. The periodicity and separation of time-scales suggests that it may be beneficial to implement a form of non-linear model predictive control in which a prediction of near-future turbine behavior can be constructed from the previous several periods of turbine measurements and an assumption of invariant inflow. This side-steps the need for an upstream flow measurement and could potentially address latency issues like those observed in Section 5. However, due to the relatively short prediction horizon over which the assumption of invariant inflow could be valid, an effective control response to the predicted behavior would need to be determined and actuated rapidly. A good initial guess, determined from the computational study of optimal trajectories, would facilitate successful implementation of this type of control law, and allow on-line adaptation that could potentially accommodate uncertainties in the presumed phase-resolved turbine model.

6.4.4 Final Remarks

This dissertation suggests a methodology for developing a time-average characterization of a cross-flow turbine in non-uniform inflow. Power-maximizing and power-tracking control laws are suggested that rely on only a time-average turbine characterization, and a means to transition stably and smoothly between these controls objectives is demonstrated in simulation and laboratory-scale experiment. Simulations and laboratory-scale experiments are found to be predictive of field-scale controller performance in a time-average sense provided that the turbines have similar performance curves and intracycle behavior, and that the controllers implemented for each turbine are sufficiently fast to respond to the energetic turbulence present in their respective inflows.

While this work seeks to address some of the challenges presented by cross-flow hydrokinetic turbines and suggest a path forward, significant hurdles remain. Axial-flow and cross-flow systems each have unique

advantages in different hydrokinetic applications and environments. At present, the diversity of market opportunities in aquaculture, remote vehicle charging stations, ocean sensing and monitoring, and other applications in the so-called blue economy, implies diverse power needs and restrictions and will likely call for different turbine morphologies to best address these needs.

When considering the eventual goal of grid-scale power generation, the figure-of-merit will be the levelized cost of energy. In large deployments, the principle advantage of cross-flow turbines is the potential to more easily construct dense arrays to boost aggregate power output. An optimal control law must therefore be considered in terms of array performance. While this work with a cross-flow single turbine can certainly advise array control algorithm development, array design and control presents unique challenges and opportunities, and is a somewhat distinct research effort from single-turbine design and control optimization: the best turbine and controller combination for a single device will likely not be the best of either for an array. It is advised that, while pursuing blue-economy markets, opportunities to explore and utilize even small turbine arrays are not overlooked. Incremental research in this area will decrease the knowledge gap needed to implement cross-flow technologies in grid-scale power generation.

Appendices

A Linearization of the Turbine System

The turbine dynamic system is first-order and nonlinear.

$$J\dot{\omega} = \tau_h - \tau_c - B\omega \tag{44}$$

Here, to follow the method of [18], a form of the equation is used in which the resistive torque resulting from mechanical damping in the power-take-off ($B\omega$) is separated from the resistive control torque deliberately applied at the PTO, where B is the torsional damping coefficient (N-m-s/rad). In the laboratory implementation, the torque measurements at the load cells could not distinguish between the sources of resistive torque, and further, the inner PI loop (Figure 4.2) ensured that the load cell measured torque was equal to the prescribed control torque, effectively ensuring negligible damping. As such, Equation 1 was used. At steady state, the damping torque is equal to the difference between hydrodynamic torque and the control torque.

Linearization of this system is used to develop power-tracking pitch controllers for axial-flow wind turbines [65], and provides theoretical limitations on turbine stability under constant-torque control [18]. Following the method of [18], we select an operating point ϕ defined by a flow velocity and rotation rate pair

$$\phi = [\overline{U}_\infty, \overline{\omega}] \tag{45}$$

Note that this is an analogous formulation to [65] for fixed-pitch blades. From this, Eq. 2 can be linearized as

$$\hat{\tau_h} = K_\omega \hat{\omega} + K_U \hat{U_\infty} \tag{46}$$

where a hat indicates a perturbation from the linearized state and K_U and K_ω are first-order Taylor expansions about ϕ, linearizing the hydrodynamic torque response to a small $\hat{U}$ or $\hat{\omega}$ respectively, or

$$K_\omega = \left.\frac{\partial \tau_h}{\partial \omega}\right|_\phi \tag{47}$$

and

$$K_U = \left.\frac{\partial \tau_h}{\partial U_\infty}\right|_\phi . \tag{48}$$

From this, the linearized version of Eq. 1 becomes

$$\dot{\hat{\omega}} = \frac{(K_\omega - B)\hat{\omega}}{J} + \frac{K_U \hat{U_\infty}}{J} - \frac{\hat{\tau_c}}{J} \tag{49}$$

and, the transfer function $G_1(s)$ estimating turbine acceleration due to $\hat{U_\infty}$ (a small change in inflow velocity) is

$$G_1(s) = \frac{K_U/J}{s + \frac{B - K_\omega}{J}} \tag{50}$$

and due to $\hat{\tau_c}$

$$G_2(s) = \frac{-1/J}{s + \frac{B - K_\omega}{J}}. \tag{51}$$

.

Note that G_1 and G_2 share a common pole, and both have the form of a first-order low-pass filter with a cut-off frequency that (for a given ϕ) is a function of B and J. The ratio B/J is the mechanical time constant, and characterizes linearized frequency-domain response [18]. In the limiting case where damping is negligible $B = 0$, there will be poles in the right half-plane when $K_\omega > 0$. This implies the system will exhibit non-minimum phase operation when hydrodynamic torque decreases with decreasing angular velocity under closed-loop control [66]. Under constant torque, the turbine is unstable in this region, as any decrease in τ_h will decelerate the turbine, further decreasing τ_h, eventually resulting in low-speed turbine stall.

Considering turbulence as a disturbance to the linearized turbine transfer function, the turbine will act as a low-pass filter on the exciting turbulence and will only show significant dynamic response to turbulence within its bandwidth.

A.1 Limitations of Linearization for Cross-flow Systems

As shown by [18], system linearization of a cross-flow turbine is a useful tool in characterizing the time-average stability of different turbine operating conditions, or controller design wherein intra-cycle variations are small or neglected [66] [11], but is inadequate for a cross-flow turbine with significant intracycle variation, as the following example will demonstrate.

Consider a turbine with significant intracycle variations operating at ϕ, selected so that for the time-

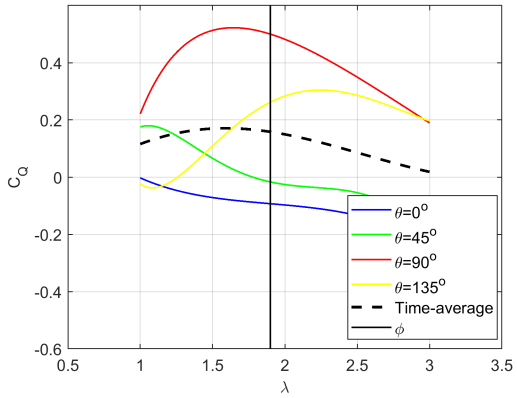

Figure A.1: C_Q **as a function of** λ **at various turbine phases for a straight-bladed cross-flow turbine. An operating point** ϕ **is presumed at** $\lambda = 1.91$**, and is indicated by a vertical line. The time-average** C_Q **vs.** λ **relationship is indicated by the hashed line.**

average C_Q vs. λ, the turbine is stable. On Figure A.1, each colored trace is the C_Q vs. λ curve at a specific θ value (i.e., the product of $C_Q N_Q$ in Eq. 2). Therefore, if we assume slowly varying or static inflow $\hat{U}_\infty \sim 0$, then ϕ implies a particular $\overline{\lambda}$, indicated by the vertical line. Over a single rotation (i.e., the set of intersections of all C_Q vs. λ traces with a vertical line at $\overline{\lambda}$), we see that the sign of K_ω at a given phase position changes for some choices of $\overline{\lambda}$, implying that the turbine exhibits non-minimum phase behavior (and is potentially unstable) at these positions. Under constant torque control, the turbine will stall unless there is sufficient inertia stored in the turbine rotor to reach an azimuthal position at a stable operating condition [61]. Further, a set of control gains (e.g., for proportional-integral-derivative control) derived based on a time-average model at a stable ϕ may be unstable at some other turbine azimuthal positions. For any such controller to be useful on a cross-flow system with significant intracycle variation in dynamics, the selected gains must not be overly aggressive, or else the turbine may stall during unstable transients (during which the system is poorly described by the linearized, time-average model). In this way, the assumption of small-perturbations integral to useful linearized models is violated in this case: the continued operation of the turbine ensures these perturbations will not be small.

The limitation of a time-average linearization suggests, at first, that linearization of a phase-resolved turbine model of the form

$$\hat{\tau_h} = K_\omega \hat{\omega} + K_U \hat{U_\infty} + K_\theta \hat{\theta} \tag{52}$$

about

$$\phi = [\overline{\omega}, \overline{U_\infty}, \overline{\theta}]$$

where

$$K_\theta = \left.\frac{\partial \tau_h}{\partial \theta}\right|_\phi \tag{53}$$

may be more useful approach for controller design, if gains were scheduled for a sufficient number of points ϕ at unique $\overline{\theta}$ spanning the interval from 0 to 2 π (this is akin to periodic gain scheduling, [28]). There are several practical limitations to this approach. Firstly, this would require a phase-resolved model of the turbine (i.e., the generation of an N_Q surface), which is non-trivial to acquire. In absence of experimental data, computational fluid dynamics (CFD) models must be of sufficient complexity to develop the phase-resolved turbine response. This involves modeling the flow interaction with the upstream blade, advecting the developed wake (and capturing the dynamic stall effect present at specific angles of attack [16] [67] [68], [69] [15]), and then modeling the interaction of the developed wake with the downstream blade, the position of which depends on the effect of the hydrodynamic torque that has been developed on the turbine, integrated through time. While time-average CFD models of cross-flow turbines have been demonstrated, accurate phase-resolved modeling of a cross-flow turbine remains a challenging objective. This suggests that evaluation in experiment may be a superior approach. Of course, this presumes the physical existence, detailed instrumentation, and successful deployment of the device in question, or an appropriate laboratory-scale analog. Because realistic inflows are turbulent, intracycle fluctuations will be convolved with turbulence, leading to uncertainty in the phase-resolved model. Higher turbulence levels will yield higher uncertainties, implying that a small-scale test in closely controlled flows would yield a more accurate estimate for the phase-resolved model. However, small-scale testing introduces further uncertainties related to scaling the model to a field-scale device [18]. Finally, the manner in which the turbine is controlled during characterization has some effect on the developed model [64]. This suggests that applying control torque by a different algorithm (e.g., the algorithm developed based upon the phase-resolved model) than used during characterization may result in a turbine response distinct from that predicted from the characterization.

Accumulation of these difficulties in model development can lead to significant model uncertainty. In controller design, model uncertainty, coupled with sensor noise/uncertainty, system latency, and other implementation-specific difficulties, implies that the developed controller must be robust to these uncertainties. Typically, robustness trades with aggressive attainment of control objectives (i.e., such a controller will sub-optimally obtain controls objectives in favor of more stable operations). Additionally, correctly switching between control gains based on θ requires additional sensing to measure θ in real-time. Overall, this suggests that linear control capable of addressing intra-cycle variations, and, more generally, control that depends on a phase-resolved model of the turbine system, will require a complex characterization pro-

cedure, and, potentially, a complex implementation, to achieve likely sub-optimal performance. In short, while controllers based upon linearized system models may be effective in the time-average sense, extending this methodology to reject intracycle perturbations introduces numerous and significant practical limitations that encourage other approaches.

A.2 Extremum-Seeking Control

In absence of a turbine model, attainment of controls objectives can be obtained automatically via an extremum-seeking controller. The general approach to an extremum-seeking controller is to systematically vary operating parameters (in the context of axial-flow wind, the varied parameters are λ [or its analog, e.g., K] and turbine blade pitch) and record performance, with the algorithm attempting to find local performance extrema that minimize the cost-function. There is no need to presume a turbine model. Examples for axial-flow turbines include [70] and [51], in which time-average turbine models are utilized. Extremum-seeking control can also be used to compensate for changes to the system that have decreased the accuracy of any previously utilized models, such as component wear. In any extremum seeking control algorithm, it is critical that the controller-introduced perturbations (i.e., the systematic changes in operating parameters) are at frequencies distinct from any external excitation, including turbulence and intracycle variations, to allow the turbine to distinguish performance differences due to control action from performance differences due to external disturbance. This is a limiting restriction: Creaby et. al used introduced control perturbations at 0.01 Hz [70]. Higher-frequency perturbations would need to be distinct from turbulence and intra-cycle variations. Actuation at high-frequencies may limit the life of the turbine drive train, and at overly-high frequencies, turbine response may not be distinguishable from sensor noise.

Strom et. al (2017) implemented an extremum-seeking control law on a cross-flow turbine to maximize power capture using a periodic angular velocity profile without foreknowledge of a phase-resolved turbine model [19]. This approach showed a substantial increase in power capture over time-average optimal controls approaches, and highlights the potential benefits of addressing intracycle fluctuations in control. An adaptation of this approach could likely be used for power-tracking objectives as well. However, this algorithm regularly relies on motoring the turbine. Further, the developed controller does not track inflow turbulence. An extension would be necessary to adapt this work to realistic time-varying inflow or power-tracking objectives.

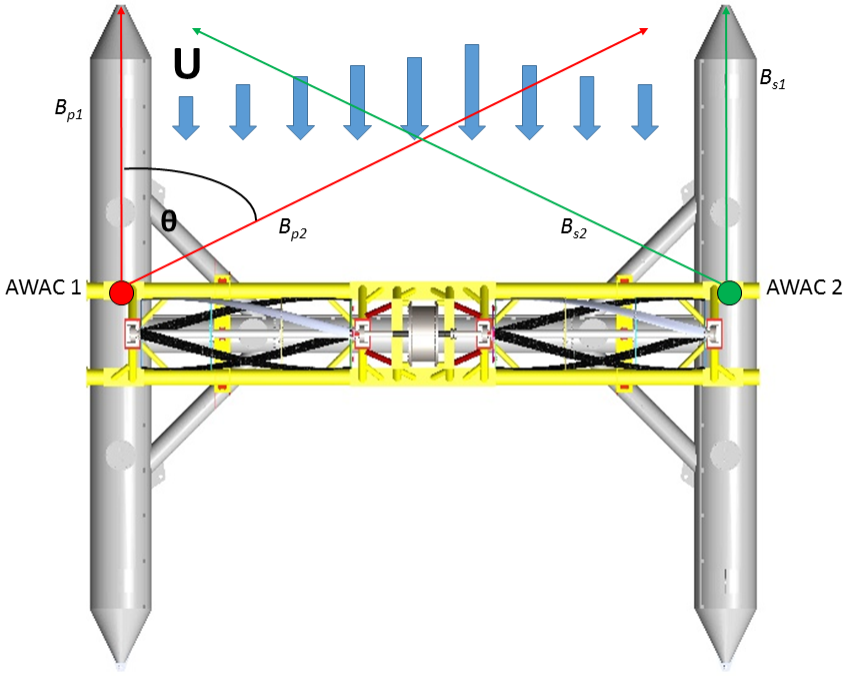

Figure B.1: The AWAC arrangement for the 2015 deployment. AWACs are indicated by the circular dots, and the beam path center lines are indicated. Wide arrows approximate the direction and magnitude of the sheared inflow free-stream.

B 2015 free-stream determination

Two 2-beam AWAC instruments are on mounted on the RivGen turbine, one at each end, such that their beams look directly upstream and across the turbine (Figure B.1). There is a $\theta = 50^o$ angle between the cross-looking beam and the axis formed by the pontoon structure of the turbine. Each instrument has a 1 m blanking distance and a 2 m bin size, so that in the along-beam direction, the edges of the 10 bins (denoted B_1 through B_{10}) are

$$L = [1 : 2 : 21]$$

where L is the distance (m) from the AWAC device. Thus, B_1 gives a velocity over a volume 1 to 3 m along-beam from the device, B_2 samples 3 to 5 m, etc. Inflow velocity measured for a given bin is assumed uniform across that bin, and adjacent bins are not entirely independent as a consequence of processing algorithms internal to the AWAC.

B.1 Distance weighting vectors

Representative inflow velocity is calculated as a weighted spatial average from the port AWAC (denoted p) and the starboard AWAC (denoted s) using their four total beams with bins $B_{p1,i}, B_{p2,i}, B_{s1,i}, B_{s2,i}$ where i

is the bin number of the respective beam. Upstream-looking beams are denoted 1, while cross-turbine beams are denoted 2. Generally

$$U_\infty = \frac{\left[\left(\frac{\sum_{i=1}^{10} W_{p1,i} B_{p1,i}}{\sum_{i=1}^{10} W_{p1,i}}\right) + \left(\frac{\sum_{i=1}^{10} W_{s1,i} B_{s1,i}}{\sum_{i=1}^{10} W_{s1,i}}\right) + \left(\frac{\sum_{i=1}^{10} W_{p2,i} B_{p2,i}}{cos(\theta)}\right) + \left(\frac{\sum_{i=1}^{10} W_{s2,i} B_{s2,i}}{cos(\theta)}\right)\right]}{(\sum_1^4 W_{[p1,s1,p2,s2]} + 2)} \tag{54}$$

where W is an arbitrary set of weights containing a multiplier for each bin in B. The sum is divided by the total of all weight plus two to account for the fact that a bin at each edge of the turbine is sampled twice, once by an upstream and once by a cross-stream looking beam.

It is likely that bins closer to the turbine are better estimators of turbine inflow velocity. Assuming both port and starboard AWACs are equally good estimators, let the weight vector due to distance from the turbine $D_{p1,s1} = [10 : -1 : 1]$. (The selection of this weighting vector is somewhat arbitrary, but a sensitivity analysis indicates that the resulting U_∞ is very similar for reasonable alternative choices of D (e.g., constant, weighted by square of distance)). Thus, $B_{[p1,s1],1}$, the closest bin to the turbine, is weighted ten times as heavily as $B_{[p1,s1],10}$, the farthest bin from the turbine. Noting that a distance of 18 m separates $B_{[p,s],1}$ from $B_{[p,s],10}$, a linear function for determining bin weights based on distance can be written

$$D(x) = 10 - 0.5(x - 2) \tag{55}$$

where x is bin center distance in m upstream from turbine. Applying this function to the projected distances from the turbine for the across-turbine beams, we see that

$$D_{p2,s2} = 10 - 0.5(L_{p1,s1} \cos(\theta) - 2) \tag{56}$$

or $D_{p2,s2} = [10.36 : -0.64 : 4.57]$. We now have weighting vectors D that weight each bin based on stream-wise distance to the turbine.

B.2 Geometry Weighting Vectors

The rotor is 11 m from end to end. Taking the horizontal (across-turbine) projection of the cross-looking beams, we see that bins far from the device sample flow outside of the rotor projected area

$$\sin(\theta) L_{[p2,s2],[8,9,10]} > 11$$

and are not used for velocity estimation.

Additionally, there is a 2.8 m wide rotor gap 4.1 m from each end of the turbine that includes the

generator and surrounding gap spaces. Bins sampling this area should also be excluded from calculation, as this is not part of the turbine rotor projected area. Bins meeting this criteria are

$$4.1 < \sin(\theta) L_{[p2,s2],4]} < 6.8.$$

Bins 3 and 7 of the cross-turbine looking beams are only partially over rotor areas. Multiplying Bins 3 and 7 by the fraction of projected area over the rotor area accounts for this. These geometry-related corrections are combined as a geometric weighting vector G where

$$G_2 = [1, 1, 0.18, 0, 1, 1, 0.68, 0, 0, 0]$$

for each across-turbine beam. Note that for the upstream-looking beams, $G_1 = [1, ...1]$ because these bins project entirely onto the rotor.

To account for both distance from the turbine and fraction of bin area projected onto the rotor, weighting vectors D and G can be multiplied element-wise.

$$W = D * G$$

where $*$ is element-wise multiplication. Following this procedure, we find

$$W_{p2,s2} = [10.36, 9.71, 1.60, 0, 7.79, 7.14, 4.42, 0, 0, 0]$$

and

$$W_{p1,s1} = [10 : -1 : 1].$$

From these, an effective inflow velocity can be calculated from the raw AWAC data in real-time.

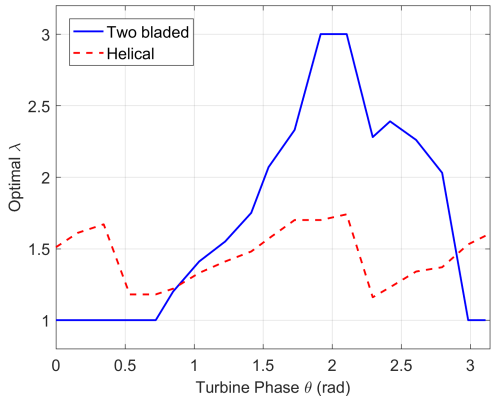

Figure C.1: Example control trajectory from the turbines utilized in Section 5.

C Limitations of Resistive Torque

Even under idealized simulation conditions, it is not possible to fully eliminate intracycle power fluctuations (Figure 5.11). Under resistive torque control, the available turbine acceleration depends upon the inflow velocity (Equation 1 and 2). This suggests that a particular intracycle angular velocity trajectory can be attained above a particular inflow velocity. Here, we assume phase-resolved and time-average turbine performance models are available (Figures 5.3 and 5.2 are adopted for this example, though these constant-velocity characterizations are an imperfect approximation to turbine hydrodynamics while under an arbitrary control law [64]), such that a sort of power-maximizing trajectory is known (i.e., a maximum C_P and corresponding λ is known at each θ). Further, we neglect the effects of turbulence, since the frequency of an engulfing gust is substantially lower than the primary rotation frequency (i.e., the flow can be reasonably approximated as constant within a single turbine rotation).

As shown in Figure 5.3, τ_h varies with azimuthal position, implying azimuthal variation in C_P by Eq. 6. Consider a control trajectory that tracks the maximum of the C_P vs. λ curve over all θ for a turbine with little hydrodynamic dependence on azimuthal position (e.g., high-solidity helical) and another with strong azimuthal variations (e.g., low solidity straight-blade). This is shown in Figure C.1. Note that for some portions of the straight-bladed turbine rotation, the C_P value decreases monotonically with increasing λ, and so the optimal trajectory follows the lower bound of the characterization at $\lambda = 1$. Under the assumption of constant inflow velocity, these trajectories imply angular acceleration and deceleration.

Under purely resistive torque, the turbine can only be accelerated by the fluid forcing (i.e., hydrodynamic torque), such that the gradient $\frac{\partial \lambda}{\partial \theta}$ implies a minimum flow velocity for which this turbine acceleration, and thus, this trajectory, is attainable. Under constant U, $\frac{\partial \lambda}{\partial t} = \frac{\partial \omega}{\partial t}$. Because $\theta = \theta(t)$, by the chain rule $\frac{\partial \lambda}{\partial t} = \frac{\partial \lambda}{\partial \theta}\frac{\partial \theta}{\partial t}$ and, noting $\omega = \frac{\partial \theta}{\partial t}$, the turbine dynamics (Eq. 1) under constant U are described by

$$\omega \frac{\partial \lambda}{\partial \theta} = \frac{1}{2J} \rho A R C_Q N_Q U^2 \tag{57}$$

where $\tau_c = 0$ to maximize turbine acceleration. Note that this assumption implies that, although the maximum C_P is maintained, this trajectory is distinct from a power-maximizing trajectory because power capture during any turbine acceleration is zero. This trajectory was selected as an example because it can be readily defined from Figures 5.2 and 5.3, and provides a conservative estimate of the minimum flow velocity. Rearranging, and invoking the definition of tip speed ratio,

$$\frac{\partial \lambda}{\partial \theta} = \frac{1}{2J} \rho A R^2 C_Q N_Q U / \lambda \tag{58}$$

from which the minimum necessary flow velocity to achieve a maximum $\frac{\partial \lambda}{\partial \theta}$ can be calculated from Figures 5.3 and C.1. Treating $\frac{\partial \lambda}{\partial \theta}$ as a discrete derivative based on Figure C.1 and $C_Q N_Q$ as the mean over the interval $[(\lambda_1, \theta_1), (\lambda_2, \theta_2)]$, the minimum U is given as

$$U_{min} = \frac{\lambda_2 - \lambda_1}{\theta_2 - \theta_1} (\lambda_2 + \lambda_1) J / \rho A R^2 C_Q N_Q. \tag{59}$$

For the example trajectory, U_{min} for the helical turbine is 0.56 m/s, and U_{min} for the straight-bladed turbine is 1.27 m/s. This suggests that larger azimuthal variations imply larger minimum flow velocities.

From this, we see that flow speeds can be prohibitively high for the attainment of optimal control trajectory in laboratory facilities. While the specific critical $\frac{\partial \lambda}{\partial \theta}$ utilized here was for a simple example trajectory, any optimal intracycle velocity trajectory defined by a control law will imply a $\frac{\partial \lambda}{\partial \theta}$ under which it is attainable. This implies that, under constant inflow, purely-resistive control torque, it is not generally possible to completely eliminate intracycle variations from turbine response, and those variations are exacerbated by low flow speeds and large positive $\frac{\partial \lambda}{\partial \theta}$ gradients. Because straight-bladed turbines with a low blade count generally have large $\frac{\partial \lambda}{\partial \theta}$ gradients, but higher peak efficiency, this suggests a trade-off between efficiency and consistency in power output when using a purely resistive control torque [71].

Further, note that U_{min} is proportional to J and inversely proportional to AR^2. For a rotating mass, $J = \frac{1}{2} m R^2$, where m is the mass of the rotating body and $A = 2RL$, where L is the length of the turbine dimension perpendicular to R. If we assume a straight blade of constant cross-sectional area A_c and constant density ρ_c, then mass can be approximated as $m = \rho_c A_c L$ (neglecting any rotating blade support structure). By substitution, we see that

$$U_{min} \sim \frac{J}{AR^2} = \frac{mR^2}{(4RL)R^2} = \frac{m}{4RL} = \frac{\rho_c A_c L}{4RL} = \frac{\rho_c A_c L}{4RL} \sim \frac{1}{R} \tag{60}$$

While it is likely that A_c will increase with turbine scale, this proportionality implies that U_{min} will decrease for a given turbine as R increases. This implies that purely resistive-torque control algorithms could approach optimal trajectories for larger machines.

Extending this approach for a prescribed resistive control torque (e.g., P/ω) will provide a more realistic estimate of minimum required inflow speed, but will require a more complicated iterative solution method because the optimal $\frac{\partial \lambda}{\partial \theta}$ trajectory is itself a function of λ and U.

Table 11: Alternative Region 3 Control Approaches

Control Description	Abbreviation
Proportional-Integral-Derivative on Power, Overspeed	PID-PO
Proportional-Integral-Derivative on Power, Underspeed	PID-PU
Adaptive K on Power, Overspeed	KO
Adaptive K on Power, Underspeed	KU
Linear Quadratic Integrator	LQI

D Alternative Region 3 Control Approaches

The Region 3 (power-tracking) controller presented in Section 5 was selected following an investigation of multiple prospective controllers in simulation. Throughout this section, simulation used a phase-resolved model (except where noted) of the helical and straight-bladed turbine, as described in Section 5. A combination of overspeed and underspeed controllers were investigated. The attempted controllers are listed in Table 11.

This investigation is not intended as an exhaustive vetting of the attempted controllers. It is possible that they may be usefully applied to cross-flow turbines in some circumstances. However, rejected controllers were either not conducive to the objectives of this work or demonstrated poor performance or robustness.

D.1 Evaluated Control Laws

The linear proportional-integral-derivative (PID) control law was attempted as both an underspeed and overspeed control law. The PID control law is given as Equation 61.

$$\tau_c = K_P P_{error} + K_I \int P_{error} dt + K_D \frac{\partial P_{error}}{\partial t} \tag{61}$$

where K_P, K_I, and K_D are proportional, integral and derivative gains respectively. To prevent integral wind-up, the technique of [55] was employed. The PID architecture can also be used to adjust K in an adaptive $K\omega^2$ control law as

$$K = K_P P_{error} + K_I \int P_{error} dt + K_D \frac{\partial P_{error}}{\partial t} \tag{62}$$

and control torque is then defined as Equation 13.

Gains for each of these control laws were tuned iteratively in simulation by a Nelder-Mead Simplex optimizer (repeated many times from a randomized initial simplex to increase the probability that a global minimum was found) attempting to minimize the sum of squared power tracking errors over the testing interval [72]. The learned gains were cross-validated using unique laboratory free-stream time series. The

performance for each control law is considered under optimal gains found to provide good, stable performance across all tested time series.

Finally, an optimal linear-quadratic-integrator (LQI) control law was attempted. LQI control is discussed rigorously in [73]. An LQI controller is functionally similar to a PI controller, and can be derived using linearizations of the turbine dynamic equation (Eq. 1) assuming constant inflow (Eq. 50). This allowed the construction of a linear system of the form

$$\begin{aligned} \dot{x} &= Ax + Bu \\ y &= Cx + Du \end{aligned} \tag{63}$$

for output value y where

$$\begin{aligned} x &= \hat{\dot{\omega}} \\ y &= \hat{P} \\ u &= \hat{\tau_c} \\ A &= \frac{K_\omega}{J} \\ B &= \frac{-1}{J} \\ C &= \overline{\tau_c} \\ D &= \overline{\omega} \end{aligned} \tag{64}$$

where an overline denotes a quantities in equilibrium at the fixed point about which the system was linearized and P is mechanical power at the power take-off (Eq. 8).

The LQI gains are selected to minimize the quadratic cost function

$$\mathcal{J} = \int x^T Q x + u^T R u dt \tag{65}$$

where $\mathcal{J}$ is the cost, x is the state matrix of the linearized system, u is the input control, Q is a matrix penalizing changes in states, R is a matrix penalizing control actuation, and ^{T} is the matrix transpose operator. In practice, the Q and R matrices will depend on the implementation and the operating objectives of the turbine system. In this study, Q was the identity matrix, and R was an iteratively-adjusted diagonal matrix. The controller gains were determined for the linearized system using the Matlab 'lqi' function, which solves the Algebraic Ricatti Equation for the selected cost function and specified linear system. In order to

adapt the control law to the significant intracycle variations, the system was linearized at discrete θ (i.e., K_ω was determined at each θ), and the resulting LQI control gains were scheduled based upon turbine angular position.

D.1.1 Power-Tracking Error Definition

Because all attempted controllers used a power tracking error to calculate control torque, overspeed and underspeed control laws are differentiated through alternate definitions of power-tracking error. For overspeed control laws, turbine power is decreased by increasing λ. Thus, power tracking error is defined as

$$P_{error} = P_{set} - P \tag{66}$$

such that too much turbine power P results in a negative value of power-tracking error, leading to a reduction in τ_c (in the case of adaptive $K\omega^2$, a reduction in K and a subsequent reduction in τ_c) and a higher equilibrium λ. For underspeed control, turbine power is decreased by decreasing λ, so the negative power tracking error is utilized

$$P_{error} = P - P_{set} \tag{67}$$

such that too much turbine power results in a positive value of power tracking error, leading to an increase in τ_c (or K) and a lower equilibrium λ.

For LQI control, power tracking error was defined using the former definition, specified by the gain-scheduling procedure.

D.2 Control Law Performance

The performance of each tested control law and considerations for implementation are discussed qualitatively in each subsequent section.

D.2.1 PID on Power

Overspeed PID control showed sum of squared power tracking errors comparable with the P/ω control discussed in Section 5. The optimizer consistently drove the derivative gain to zero, and the tuned gains demonstrated satisfactory performance in all cross-validation cases. In fact, for the two-bladed turbine, overspeed PID control out-performed the benchmark P/ω controller. Further, gains converged consistently to similar values for largely separated initial guesses. Importantly, these gains were also similar when the

tuning procedure was repeated using only a time-average turbine model, implying that gain tuning may not require knowledge of a phase-resolved turbine model. This is consistent with turbine hydrodynamics, since, as tip-speed ratio increases, the angle of attack oscillations experienced by the foil decrease in amplitude, and the amplitude of intracycle hydrodynamic power oscillations decrease as well.

Underspeed PID control showed sum-of-squared power-tracking errors several orders of magnitude larger than the overspeed controller. The tuned gains were both less aggressive and stronger functions of initial guess: poor initial guesses frequently resulted in all gains converging to zero. Further, tuned gains performed less reliably in cross-validation studies, demonstrating unstable behavior for some inflow time-series.

Due to its satisfactory performance, overspeed PID control was attempted in laboratory experiment, as described in Section 5. However, noisy estimates for turbine power (a consequence of noise in the torque measurement), system latency, and non-linear servomotor behavior invalidated the simulation-optimized gains. A similar gain tuning procedure was attempted on the laboratory implementation, but all resulting gain combinations showed unstable behavior and significantly poorer performance than the P/ω control law (which did not require a power measurement or tuning procedure).

D.2.2 Adaptive $K\omega^2$

Overspeed adaptive K control showed slightly poorer performance to PID-PO and P/ω control. Additionally, gain tuning took longer and was more sensitive to initial guess than for PID-PO control. Optimal KO control gains were also well-approximated by time-average simulation. Like PID-PO, optimal $K_D = 0$ for this control law.

Underspeed adaptive K control showed slightly lower power tracking errors than PID-PU, but still showed significantly poorer performance than overspeed control laws. Gain tuning also took longer, was extremely sensitive to initial guess, and proved to be less robust during cross-validation. Compared to KO, the suggested gains are much less aggressive.

D.2.3 Linear Quadratic Integrator

LQI control showed excellent performance for both turbines in simulation when the linearized system (from which the LQI gains were derived) was used in place of the actual nonlinear turbine model. However, when a realistic turbine model was applied, the small dynamic discrepancies resulting from linearization errors significantly degraded performance. A similar result was seen for all other introduced non-idealities: small levels of signal noise, latency, or uncertainties in the phase-resolved model from which scheduled gains were derived. By increasing the magnitude of R, unstable behavior could be reduced, but performance was reduced commensurately such that robust LQI performance was slightly worse than PID-PO. Because this

control law failed to outperform PID-PO under all but ideal simulated conditions and requires a far more involved development procedure, it was not pursued further.

Importantly, satisfactory performance of this control law was also only demonstrated if the turbine was motored, a violation of the restrictions adopted in Section 5.

D.3 Observations

None of the tested controllers consistently outperformed P/ω control, despite the additional complexities of their implementations. For these reasons, P/ω control was pursued in Section 5. In general, underspeed control laws exhibit much higher power-tracking error than overspeed controllers and are less robust. The degradation of performance for underspeed torque control laws is expected, as these control laws more frequently exhibit non-minimum phase behavior. Underspeed control laws also require a more complicated transition between Region 2 and Region 3 objectives that the approach adopted in Section 5.

References

[1] V. S. Neary, B. Gunawan, and D. C. Sale. Turbulent inflow characteristics for hydrokinetic energy conversion in rivers. *Renew. Sustain. Energy Rev.*, 26:437–445, 2013.

[2] J. Thomson, B. Polagye, V. Durgesh, and M. C. Richmond. Measurements of Turbulence at Two Tidal Energy Sites in Puget Sound, WA. *IEEE J. Ocean. Eng.*, 37(3):363–374, jul 2012.

[3] Alana E S Duerr and Manhar R. Dhanak. An assessment of the hydrokinetic energy resource of the Florida current. *IEEE J. Ocean. Eng.*, 37(2):281–293, 2012.

[4] M.J. Khan, G. Bhuyan, M.T. Iqbal, and J.E. Quaicoe. Hydrokinetic energy conversion systems and assessment of horizontal and vertical axis turbines for river and tidal applications: A technology status review. *Appl. Energy*, 86(10):1823–1835, oct 2009.

[5] Herbert J Sutherland, Dale E Berg, and Thomas D Ashwill. A Retrospective of VAWT Technology. Technical Report January, 2012.

[6] Brandon L Ennis and D Todd Griffith. System Levelized Cost of Energy Analysis for Floating Offshore Vertical-Axis Wind Turbines. (August), 2018.

[7] TJ Carlson, M Grear, AE Copping, M Halvorsen, R Jepsen, and K Metzinger. Assessment of Strike of Adult Killer Whales by an OpenHydro Tidal Turbine Blade. *Prep. U.S. Dep. Energy by Pacific Northwest Natl. Lab.*, (January), 2014.

[8] C Garrett and P Cummins. The efficiency of a turbine in a tidal channel. *J. Fluid Mech.*, 588:243–251, 2007.

[9] Xiaojing Sun, Diangui Huang, and Guoqing Wu. The current state of offshore wind energy technology development. *Energy*, 41(1):298–312, 2012.

[10] J.O. Dabiri. Potential order-of-magnitude enhancement of wind farm power density via counter- rotating vertical-axis wind turbine arrays. *J. Renew. Sustain. Energy*, 3, 2011.

[11] Lucy Y. Pao and Kathryn E Johnson. Control of Wind Turbines: Approaches, Challenges, and Recent Developments. *IEEE Control Syst. Mag.*, (April):44–62, 2011.

[12] Brian Kirke and Leo Lazauskas. Variable Pitch Darrieus Water Turbines. *J. Fluid Sci. Technol.*, 3(3):430–438, 2008.

[13] S H Salter and J R M Taylor. Vertical-axis tidal-current generators and the Pentland Firth. *Proc. Inst. Mech. Eng. Part A J. Power Energy*, 221(2):181–199, 2007.

[14] L. Lazauskas and B. K. Kirke. Modeling passive variable pitch cross flow hydrokinetic turbines to maximize performance and smooth operation. *Renew. Energy*, 45:41–50, 2012.

[15] B. Paillard, F. Hauville, and J. a. Astolfi. Simulating variable pitch crossflow water turbines: A coupled unsteady ONERA-EDLIN model and streamtube model. *Renew. Energy*, 52:209–217, 2013.

[16] I Paraschivoiu, O Trifu, and F Saeed. H-Darrieus Wind Turbine with Blade Pitch Control. *Int. J. Rotating Mach.*, 2009:1–7, 2009.

[17] Takahiro Kiwata, Tetsuyoshi Kita, Tatsuro Yamada, Shinei Takata, Nobuyoshi Komatsu, and Shigeo Kimura. Performance of Vertical Axis Wind Turbine with Variable-Pitch Straight Blades by a Linkage Mechanism. *Trans. Japan Soc. Mech. Eng. Ser. B*, 74(748):2543–2551, 2008.

[18] Robert J Cavagnaro. *Performance Evaluation, Emulation, and Control of Cross-Flow Hydrokinetic Turbines*. Doctoral thesis, University of Washington, 2016.

[19] Benjamin Strom, Steven L. Brunton, and Brian Polagye. Intracycle angular velocity control of cross-flow turbines. *Nat. Energy*, 2(June), 2017.

[20] C. Simão Ferreira, H. Aagaard Madsen, M. Barone, B. Roscher, P. Deglaire, and I. Arduin. Comparison of aerodynamic models for vertical axis wind turbines. *J. Phys. Conf. Ser.*, 524(1), 2014.

[21] Lucy Y Pao and Kathryn E Johnson. A Tutorial on the Dynamics and Control of Wind Turbines and Wind Farms. In *Am. Control Conf.*, 2009.

[22] Jin Tan, Weihao Hu, Xiaoru Wang, and Zhe Chen. Effect of tower shadow and wind shear in a wind farm on AC tie-line power oscillations of interconnected power systems. *Energies*, 6(12):6352–6372, 2013.

[23] Tongguang Wang and Frank N Coton. An Unsteady Aerodynamic Model for HAWT Performance Including Tower Shadow Effects. *Wind Eng.*, 23(5):255–268, 1999.

[24] Swagata Das, Neeraj Karnik, and Surya Santoso. Time-Domain Modeling of Tower Shadow and Wind Shear in Wind Turbines. *ISRN Renew. Energy*, 2011:1–11, 2011.

[25] S.R.J Powles. The Effects of Tower Shadow on the Dynamics of a Horizontal-Axis Wind Turbine. *Wind Eng.*, 7(1):26–42, 1983.

[26] Robert J Cavagnaro, Brian Polagye, Jim Thomson, Brian Fabien, Dominic Forbush, and Levi Kilcher. Emulation of a Hydrokinetic Turbine to Assess Control and Grid Integration. In *Proc. 11th Eur. Wave Tidal Energy Conf.*, pages 1–8, Nantes, France, 2015.

[27] Kathryn E Johnson, Lucy Y Pao, Mark J Balas, and Lee J Fingersh. Control of Variable Speed Wind Turbines Standard and Adaptive Techniques For Maximizing Energy Capture. *IEEE Control Syst. Mag.*, (June):70–81, 2006.

[28] Jackson G Njiri and Dirk Söffker. State-of-the-art in wind turbine control : Trends and challenges. *Renew. Sustain. Energy Rev.*, 60:377–393, 2016.

[29] Andrew Kusiak, Wenyan Li, and Zhe Song. Dynamic control of wind turbines. *Renew. Energy*, 35(2):456–463, 2010.

[30] Katherine McCaffrey, Baylor Fox-Kemper, Peter E. Hamlington, and Jim Thomson. Characterization of turbulence anisotropy, coherence, and intermittency at a prospective tidal energy site: Observational data analysis. *Renew. Energy*, 76:441–453, 2015.

[31] Uwe Fey, Michael Konig, and Helmut Eckelmann. A new StrouhalReynolds-number relationship for the circular cylinder in the range 47<Re<210ˆ5. *Phys. Fluids*, 10(7):1547, 1998.

[32] G.I. Taylor. Spectra of Turbulence. *Proc. R. Soc. London. Ser. A, Math. Phys. Sci.*, 1937.

[33] Stephen B. Pope. *Turbulent Flows*. Cambridge University Press, Cambridge, Massachusetts, 2000.

[34] Dominic Forbush, Rob Cavagnaro, Brian Fabien, Brian Polagye, James Donegan, and Jarlath McEntee. Development of a Cross-Flow Hydrokinetic Turbine in Simulation, Experiment, and Field Testing. In *Proc. 4th Mar. Energy Technol. Symp.*, 2016.

[35] Dominic Forbush, Brian Polagye, Box Stevens, and Way Ne. Predicting cross-flow turbine controller dynamics with low-order simulation. In *Proc. 11th Eur. Wave Tidal Energy Conf.*, volume 2, Cork, Ireland, 2017.

[36] Jason Laks, Lucy Pao, Alan Wright, Neil Kelley, and Bonnie Jonkman. The use of preview wind measurements for blade pitch control. *Mechatronics*, 21(4):668–681, jun 2011.

[37] M Harris, M Hand, and A Wright. Lidar for Turbine Control. *NREL Tech. Rep.*, NREL/TP-50(January), 2005.

[38] Fiona Dunnel and Lucy Y Pao. Benefit of Wind Turbine Preview Control as a Function of Measurement Coherence and Preview Time. In *2013 Am. Control Conf.*, 2013.

[39] David Schlipf, Po Wen Cheng, and Jakob Mann. Model of the Correlation between Lidar Systems and Wind Turbines for Lidar-Assisted Control. *J. Atmos. Ocean. Technol.*, 30(10):2233–2240, oct 2013.

[40] Dominic Forbush, Brian Polagye, Jim Thomson, Levi Kilcher, James Donegan, and Jarlath McEntee. Performance characterization of a cross-flow hydrokinetic turbine in sheared inflow. *Int. J. Mar. Energy*, 16:150–161, 2016.

[41] R.T. Cheng and J.W. Gartner. Complete velocity distribution in river cross-sections measured by acoustic instruments. *Proc. IEEE/OES Seventh Work. Conf. Curr. Meas. Technol. 2003.*, pages 21–26, 2003.

[42] Ocean Renewable Power Company. At Small River Sites : ORPC 's RivGen ® Power System, 2014.

[43] Vincent Neary, Carlos Michelen, Andrew Murphy, Ryan Coe, and Hal Youngren. Numerical Modeling Study to Investigate RivGen® Strut Drag on Power Performance. Technical Report Figure 1, Sandia National Laboratories, Albuquerque, NM, 2014.

[44] Peter Bachant and Martin Wosnik. Performance measurements of cylindrical- and spherical-helical cross-flow marine hydrokinetic turbines , with estimates of exergy efficiency. *Renew. Energy*, 74:318–325, 2015.

[45] Jim Thomson, Levi Kilcher, Marshall Richmond, Joe Talbert, Alex DeKlerk, Brian Polagye, Maricarmen Guerra, and Rodrigo Cienfuegos. Tidal turbulence spectra from a compliant mooring. In *Proc. 1st Mar. Energy Technol. Symp.*, Washington, D.C., 2013.

[46] Levi F Kilcher and Jim Thomson. Determining the spatial coherence of turbulence at mhk sites. In *Proc. 2nd Mar. Energy Technol. Symp.*, pages 1–7, Seattle, WA, 2014.

[47] Elizabeth a. Nystrom, Kevin a. Oberg, and Chris R. Rehmann. Measurement of Turbulence with Acoustic Doppler Current Profilers - Sources of Error and Laboratory Results. *Hydraul. Meas. Exp. Methods 2002*, pages 1–10, 2002.

[48] Yadolah Dodge. *The Concise Encyclopedia of Statistics*, volume 38. Springer Science + Business Media, 2011.

[49] TerraSond Ltd. Kvichak River RISEC Project Resource Reconnaissance & Physical Characterization Final Report. Technical report, Terrasond Ltd., Palmer, AK, 2011.

[50] Y K Sanusi and S G Abisoye. Estimation of Wind Energy Potential in Southwestern Nigeria . *Pacific J. Sci. Technol.*, 12(2):160–166, 2011.

[51] Tinglong Pan, Zhicheng Ji, and Zhenhua Jiang. Maximum Power Point Tracking of Wind Energy Conversion Systems Based on Sliding Mode Extremum Seeking Control. In *2008 IEEE Energy 2030 Conf.*, 2008.

[52] C. Zhang and Raul Ordonez. *Extremum-Seeking Control and Applications A Numerical Optimization-Based Approach.* Springer, Hoboken, NJ, 18 edition, 2012.

[53] Dominic Forbush, Robert J. Cavagnaro, James Donegan, Jarlath McEntee, and Brian Polagye. Multi-mode evaluation of power-maximizing cross-flow turbine controllers. *Int. J. Mar. Energy*, 20:80–96, 2017.

[54] Robert J Cavagnaro, Jason C Neely, F.X. Fa, and Joseba Lopez Mendia. Evaluation of Electromechanical Systems Dynamically Emulating a Candidate Hydrokinetic Turbine. *IEEE Trans. Power Syst.*, 7(1):390–399, 2016.

[55] Karl Johan Aström and Richard M. Murray. *PID Control.* Princeton University Press, Princeton, New Jersey, 2.10c edition, 2010.

[56] Dominic Forbush, Brian Polagye, Jim Thomson, Brian Fabien, James Donegan, and Jarlath McEntee. Characterization and Control of a Cross-Flow Turbine in Shear Flow. In *Proc. 3rd Mar. Energy Technol. Symp.*, pages 3–8, Washington, D.C., 2015.

[57] Robert J. Cavagnaro and Brian Polagye. Field performance assessment of a hydrokinetic turbine. *Int. J. Mar. Energy*, 14:125–142, 2015.

[58] Mitsuhiro Shiono, Katsuyuki Suzuki, and Seiji Kiho. Experimental study of the characteristics of a Darrieus turbine for tidal power generation. *Electr. Eng. Japan (English Transl. Denki Gakkai Ronbunshi)*, 132(3):38–47, 2000.

[59] J.N. Newman. *Marine Hydrodynamics.* The MIT Press, Cambridge, Massachusetts, 1977.

[60] K E Johnson, L J Fingersh, Mark J Balas, and Lucy Y Pao. Methods for Increasing Region 2 Power Capture on a Variable Speed HAWT Preprint. In *23rd ASME Wind Energy Symp.*, Reno, NV, 2004.

[61] Robert J Cavagnaro and Brian Polagye. Dynamics of a Stalling Cross-Flow Turbine. In *Proc. 4th Mar. Energy Technol. Symp.*, Washington, D.C., 2016.

[62] David Schlipf, Dominik Johannes Schlipf, and Martin Kühn. Nonlinear model predictive control of wind turbines using LIDAR. *Wind Energy*, (16):1107–1129, 2013.

[63] Derek G. Goring and Vladimir I. Nikora. Despiking Acoustic Doppler Velocimeter Data. *J. Hydraul. Eng.*, 128(1):117–126, 2002.

[64] B Polagye, B Strom, D Forbush, H Ross, and R Cavagnaro. Quantifying Performance of Cross-flow Turbines. *Prog.*, 2018.

[65] M Maureen Hand and Mark J Balas. Systematic Controller Design Methodology for Variable-Speed Wind Turbines Systematic Controller Design Methodology for Variable-Speed Wind Turbines. (February), 2002.

[66] Vincent J Ginter and Jeff K Pieper. Robust Gain Scheduled Control of a Hydrokinetic Turbine. *IEEE Trans. Control Syst. Technol.*, 19(4):805–817, 2011.

[67] W. J. Mccroskey. The phenomenon of dynamic stall. 1981.

[68] Lawrence W. Carr. Progress in analysis and prediction of dynamic stall. *J. Aircr.*, 25(1):6–17, 1988.

[69] H. C. Tsai and T. Colonius. Coriolis Effect on Dynamic Stall in a Vertical Axis Wind Turbine at Moderate Reynolds Number. In *32nd AIAA Appl. Aerodyn. Conf.*, volume 54, Pasadena, CA, 2016. AIAA.

[70] Justin Creaby, Yaoyu Li, and John E Seem. Maximizing Wind Turbine Energy Capture using Multivariable Extremum Seeking Control. *Wind Eng.*, 33:361–387, 2009.

[71] Benjamin Strom, Brian Polagye, and Steve Brunton. Hydrodynamic Optimization of Cross-Flow Turbines with Large Chord to Radius Ratios. In *Proc. 3rd Mar. Energy Technol. Symp.*, Washington, D.C., 2015.

[72] Russell R Barton, John S Ivey, Russell R Barton, and John S Ivey. Nelder-Mead Simplex Modifications for Simulation Optimization. *Manage. Sci.*, 42(7):954–973, 1996.

[73] Peter C Young. An approach to the linear multivariable servomechanism problem. *Int. J. Control*, 15(5):961–979, 1972.